Vilnius University

CENTER FOR PHYSICAL
SCIENCES AND TECHNOLOGY

Lina
DEDELAITĖ

π-π Conjugated Compounds and Gold Nanostructures for Sensor Design

DOCTORAL DISSERTATION

Physical sciences,
Chemistry (03 P)

VILNIUS 2018

The doctoral dissertation was prepared at Vilnius University, Faculty of Chemistry and Geosciences in the period of 2013 - 2018. A part of experimental work was performed in collaboration with Selcuk University (Konya, Turkey), Institute of physics (Chemnitz, Germany) and Center for Physical Science and Technology Vilnius (Vilnius, Lithuania).

Scientific supervisor:
prof. habil. dr. Arūnas Ramanavičius (Vilnius University, Physical Sciences, chemistry -03P)

Evaluation Board:
Chairman – **habil. dr. Gediminas Niaura** (Physical Science and Technology Vilnius, Physical Sciences, chemistry -03P)
Members:
Habil. dr. Rimas Ramanauskas (Physical Science and Technology Vilnius, Physical Sciences, chemistry -03P)
Prof. dr. Vida Vičkačkaitė (Vilnius University, Physical Sciences, chemistry – 03P)
Dr. Svajus Asadauskas (Physical Science and Technology Vilnius, Physical Sciences, chemistry -03P)
Dr. Vitali Syritsky (Tallinn Technical University, Physical Sciences, chemistry - 03P)

The doctoral dissertation defense will be held on 28th of September 2018 at 3 p.m. at the public meeting of the Evaluation Board at the Inorganic chemistry auditorium (141) of the Faculty of Chemistry and Geosciences of Vilnius University. Address: Naugarduko g. 24, LT-03225, Vilnius, Lithuania, Tel.: 2193108; e-mail: lina.dedelaite@gmail.com

The dissertation is available at the Library of Vilnius University and at the Library of FTMC, and on the Internet:
https://www.vu.lt/naujienos/ivykiu-kalendorius

Vilniaus
universitetas

FIZINIŲ TECHNOLOGIJŲ
MOKSLŲ CENTRAS

Lina
DEDELAITĖ

π-π junginiai ir aukso nanostruktūros jutiklių kūrime

DAKTARO DISERTACIJA

Fiziniai mokslai,
Chemija (03 P)

VILNIUS 2018

Selčuko Universitetu (Konija, Turkija) bei Fizikos institutu (Chemnitzas, Vokietija) bei Fizinių ir technologijos mokslų centras (Vilnius, Lietuva).

Mokslinis vadovas:
prof. habil. dr. Arūnas Ramanavičius (Viliaus Universitetas, fiziniai mokslai, chemija -03P)

Gynimo taryba:
Pirmininkas – **habil. dr. Gediminas Niaura** (Fizinių ir technologijos mokslų centras, fiziniai mokslai, chemija – 03P)
Nariai:
Habil. dr. Rimas Ramanauskas (Fizinių ir technologijos mokslų centras, fiziniai mokslai, chemija – 03P)
Prof. dr. Vida Vičkačkaitė (Vilniaus universitetas, fiziniai mokslai, chemija – 03P)
Dr. Svajus Asadauskas (Fizinių ir technologijos mokslų centras, fiziniai mokslai, chemija – 03P)
Dr. Vitali Syritsky (Talino technikos universitetas, fiziniai mokslai, chemija – 03P)

Disertacija ginama viešame Gynimo tarybos posėdyje 2018 m. rugsėjo mėn. 28 d. 15:00 val. Vilnius Universiteto Chemijos ir Geomokslų fakulteto Neorganinės chemijos auditorijoje (141). Adresas: Naugarduko g.24, LT-03225, Vilnius, Lietuva, Tel.: 2193108; el. paštas lina.dedelaite@gmail.com

Disertaciją galima peržiūrėti Vilniaus universiteto ir FTMC Chemijos instituto bibliotekose ir VU interneto svetainėje adresu:
https://www.vu.lt/naujienos/ivykiu-kalendoriu

To my father Antanas Algimantas Dedela
who left too early

List of original papers by PhD candidate

Paper 1 A. Stirke, R. M. Apetrei, M. Kirsnyte, L. Dedelaite, V. Bondarenka, V. Jasulaitiene, M. Pucetaite, A. Selskis, G. Carac, G. Bahrim, Synthesis of polypyrrole microspheres by Streptomyces spp, Polymer 84 (2016) 99-106.

Paper 2 L. Dedelaite, S. Kizilkaya, H. Incebay, H. Ciftci, M. Ersoz, Z. Yazicigil, Y. Oztekin, A. Ramanaviciene, A. Ramanavicius, Electrochemical determination of Cu(II) ions using glassy carbon electrode modified by some nanomaterials and 3-nitroaniline, Colloids and Surfaces A: Physicochemical and Engineering Aspects 483 (2015) 279-284.

Paper 3 L. Dedelaite, R.D. Rodriguez, E. Andriukonis, M. Hietschold, D.R. Zahn, A. Ramanavicius, Surfaces functionalized by graphene oxide nanosheets for single cell investigations, Sensors and Actuators B: Chemical 255 (2018) 1735-1743.

Paper 4 B. Schreiber, D. Gkogkou, L. Dedelaite, J. Kerbusch, R. Hubner, E. Sheremet, D.R.T. Zahn, A. Ramanavicius, S. Facsko, R.D. Rodriguez, Large-scale self-organized gold nanostructures with bidirectional plasmon resonances for SERS, RSC Advances 8 (2018) 22569-22576.

Author's contribution to the original papers

Paper 1 Performed experiments, which were needed to verify the hypothesis. Also, together with M. Pucetaite performed infrared spectroscopy measurements and worked on writing and correcting manuscript.

Paper 2 Planned most of the experiments, performed electrode modification and electrodes characterization together with a colleague S. Kizilkaja (Turkey). Analyzed results and prepared manuscript.

Paper 3 Planned and performed all experiments, performed optical spectroscopy and Raman spectroscopy measurements. Analyzed the results and prepared the manuscript.

Paper 4 Performed the deposition of cobalt phthalocyanine on all the samples, performed Raman spectroscopy and analyzed the results. Actively worked on writing and correcting manuscript.

Table of content

List of abbreviations

AFM – atomic force microscopy
AuChts – gold-chitosan
BPPy – bacterial synthesized polypyrrole
BR – Britton-Robinson
CoPc – cobalt phthalocyanine
DPV – differential pulse voltammetry
EF – enhancement factor
EPPy – electrochemically synthesized polypyrrole
FEM – finite element method
FIB-SEM – focused ion beam scanning electron microscope
FTIR - Fourier transform infrared spectroscopy
G – graphene
GC – glassy carbon electrode
GO – graphene oxide
HOPG – highly oriented pyrolytic graphite
LOD – limit of detection
LSPR – localized surface plasmon resonance
LWD – long working distance
MWCNT – multiwalled carbon nanotubes
N.A. – numerical aperture
NIR – near-infrared spectra range
NMs – nanomaterials
OM - optical microscopy
PDMS – polydimethylsiloxane
PPy – polypyrrole
Py - pyrrole
rGO – reduced graphene oxide
RS – Raman spectroscopy
R.S.V. – relative standard variation
SE – spectroscopic ellipsometry
SEM – scanning electron microscopy
SERS – surface enhanced Raman spectroscopy
Si – silicon
STB POT – stable potential
TBATFB - tetrabutylammoniumtetrafluoroborate
TEM – transmission electron microscopy
VIS – visible spectra range
XPS – X-ray photoelectron spectroscopy
3NA – 3-nitroaniline
3NA(red) – reduced 3-nitroaniline

Introduction

A sensor is a device which detects a variable electrical or physical quantity, usually electronically, and converts it into the signal that can be acknowledged in form of electrical or optical signal. The most important aspects of the sensor are sensitivity, selectivity and stability. Sensors can be classified into the ones that are based on quantity such as thermal, chemical, optical, humidity, gas and others. In this thesis we are going to discuss about electrochemical and optical sensors.

Electrochemical sensors are very promising analytical device because they can be modified to increase their sensitivity and selectivity. Depending on the purpose of the electrochemical sensor modification procedure and materials can be adjusted which makes fabrication of such sensors easily adjustable. Nanocomposites used in the electrode modification such as carbon nanotubes, metal nanoparticles can increase the surface area for biomolecules to be immobilized and raises electrodes sensitivity. In order to improve electrodes selectivity towards the analyte specific molecules or enzymes can be used for the modification. By optimizing these two parameters the obtained electrode can be extremely sensitive and selective towards chosen analytes.

Optical sensors on the other hand do not need to be selective. Methods such as Raman spectroscopy provides information in a shape of spectra which consist of vibrations of the molecule bonds. These vibrations have set position and finger prints usually in the visible spectra range. On the other hand, Raman spectroscopy signal can be relatively low or difficult to obtain and there are always ongoing researches of how to improve it. Here comes surface enhanced Raman spectroscopy where for the signal enhancement plasmon nanoparticles are used such as gold, silver, aluminum and others. However, the substrates developed for SERS have plasmon resonance only in the limited range depending on the shape, size and the nature of the nanocomposites. This by itself limits the use of the substrate for only for the specific range of the analytes. For this reason, substrates with the bidirectional plasmon resonance can be used.

The aim of the study:

synthesis of some π-π conjugated compounds and application of π-π conjugated compounds in the design of electrochemical optical sensors.

The objectives of the study:

1. To investigate green method for the synthesis of π-π conjugated polymer – polypyrrole – microspheres using two *Streptomycess spp.* bacteria MIUG 12p and MIUG 4.88 strains.
2. To investigate the effect of some π-π conjugated nanomaterials (namely: graphene oxide, graphene, magnetite, gold-chitosan,

multiwalled carbon nanotubes) for electrochemical determination of copper(II) ions.
3. To analyze the characteristics of the optimum electrode towards Cu(II) ions detection.
4. To investigate π-π conjugated graphene oxide nanosheets for substrate treatment for obtaining single cells and the mechanism behind it.
5. To compare obtained Raman spectra from single yeast cells with the spectra from aggregated yeast cells.
6. To investigate the tunability of the localized surface plasmon resonance of the self-organized gold nanoparticles on the rippled silicon substrates and its dependence on the substrates position.
7. To simulate plasmonic hotspots by using exact nanoparticle size, geometry and configuration obtained from the experimental data.

Scientific novelty:

1. *Streptomyces spp*. bacteria showed to be a good synthesis initiator for obtaining π-π conjugated polymer polypyrrole microspheres in an environmentally friendly route and free from oxidation byproducts.
2. Multiwalled carbon nanotubes immobilized on the glassy carbon electrode before electrochemical modification and reduction of 3-nitroanline increases sensitivity towards Cu(II) ions detection.
3. Single yeast cells deposited on the substrates modified with graphene oxide nanosheets showed advanced information in Raman spectra compared to Raman spectra obtained from the yeast cells aggregated on graphene oxide modified substrate.
4. Two-step fabrication method using ion-beam and oblique angle physical vapor deposition is a suitable method for obtaining large scale self-organized gold nanoparticles with bidirectional plasmon resonance for SERS application.

Statements for defense:

1. Polypyrrole microspheres can be synthesized using ‘green method’ based on two different strains of *Streptomyces spp.* bacteria.
2. Carbon multiwalled nanotubes enhance sensitivity of glassy carbon electrode towards Cu(II) ions when they are deposited before the electrochemical modification and reduction of 3-nitroanilne.
3. Graphene oxide nanosheets modified arbitrary substrates can be used for immobilization of single cells and the enhancement of Raman signal.
4. Raman spectra of single cells deposited on the graphene oxide modified substrates show more information compared to the spectra of the cell aggregates deposited on the same substrates.

5. Two-step fabrication method using ion-beam and oblique angle physical vapor deposition is a suitable method for obtaining large scale self-organized gold nanoparticles with bidirectional plasmon resonance for SERS application.

1. Literature review

1.1.Sensors

1.1.1. Solid state electrodes

Solid state electrodes, such as gold, platinum or carbon have superior electrochemical properties, but various carbon forms are preferred because of being electrochemically inert and having wide potential window suitable for electrochemical detection, good conductivity and resistance to environmental and chemical hazards [1]. Due to these facts all carbon based electrodes seem very promising for electrochemical analytical systems [2]. To enhance and/or to extend carbon electrode properties some modifications of the surfaces are applied [3]. Recently, there has been increasing interest in electrodes' surface modification with some conductive/non-conductive polymers, organic and inorganic molecules due to their ability to bind various metal ions [4-9]. Moreover, for certain electroanalytical requirements in order to detect various analytes as individual, selective or simultaneous detection, the carbon electrodes have been modified with various nanomaterials (NMs). Main advantages of the application of a NMs-modified electrode when compared to others: high effective surface area, mass transport, catalysis and control over local microenvironment. The electrochemical sensors based on unmodified/modified nanostructured carbon materials could be applied in sensors suitable for the detection of chemical and biochemical analytes [10, 11].

1.1.2. Surface enhanced Raman spectroscopy

Raman scattering was discovered in 1928 and named after its discoverer C.V. Raman. Raman spectroscopy is based on spectral measurements on inelastic scattering of monochromatic radiation [12].

In comparison with the other methods applied for cell or molecule analysis Raman vibrational spectroscopy is non-invasive, non-destructive analysis of microorganisms. It's easy to apply, doesn't require any additional sample preparation or markings. Moreover, it allows analysis of solid, liquid and gas state materials [13]. Raman spectroscopy is one of the most sensitive methods for obtaining chemical information and is vastly used [14-20].

Even though Raman spectroscopy is widely used in many applications, the intensity or Raman signal is 10^6 weaker than Rayleigh intensity, which makes it sometimes difficult to obtain. To overcome this challenge intense light source such as laser is required. But if used in all its power it can destroy the analyte. Analytes such as cells and biological materials can undergo degradation which will lead to negative results [21]. To overcome this several solutions can be addressed: 1) reducing laser intensity

but increasing acquisition time, 2) choosing laser which is in resonance of the analyte, 3) using plasmon enhanced Raman spectroscopy methods (surface enhanced Raman scattering (SERS)), or even tip-enhanced Raman scattering method (TERS) [22, 23].

SERS effect is Raman signal amplification through the electromagnetic interaction of light with metals. There electromagnetic field forms which generally known as plasmons. To obtain Raman enhancement analyte must be absorbed on the metal surface or near it. Most used metals for SERS and plasmonics are gold (Au), silver (Ag), copper (Cu) and aluminum (Al) because they have different optical properties from other dielectrics. Other needed factor for SERS are the structures with the dimensions in the sub-wavelength range, which is usually less than 100 nm [24]. However, there is no limit how small the metallic objects are, even a rough metallic surface could be a SERS substrate. It is known that the original SERS substrate was electrochemically roughened metal electrode [25]. While using metal nanoparticles a strong emphasis is based on the optimization parameters, since both the frequency and magnitude of the maximum field enhancement are strongly dependent on the shape, size and arrangement of the metallic nanofeatures [26]. If all parameters are satisfied such substrate can have SERS enhancement factor (EF) up to 10^{11} allowing single molecule detection [27].

1.2. π–π conjugated compounds

1.2.1. Polypyrole and polyaniline

Polypyrrole (PPy) was first synthesized using chemical oxidation method from pyrrole (Py) monomer in 1961. However, various experiments started 1968 when first PPy layer was synthesized using electrochemical oxidation method. Since then various improvements were made for PPy synthesis and it has been the most extensively studied conducting polymer mainly because of its simple synthesis, environmental stability, good redox properties, biocompatibility and variable electrical conductivity. As a result of its good intrinsic properties, PPy has proven to be promising for several applications including biosensors, actuators, batteries, antistatic coatings, tissue engineering and drug delivery systems [28-32].

Most common methods for pyrrole synthesis are electrochemical and chemical oxidations. The chemical oxidation is an easy method that involves the oxidation of pyrrole in aqueous medium, commonly using ferric chloride or ammonium persulfate as oxidizing agent, resulting in an electrically conductive black powder. On the other hand, the electrochemical oxidation of pyrrole is carried out without adding chemical oxidizers, but it is limited to polypyrrole (PPy) films deposited onto the working electrode.

Developments in the biological synthesis of nanoparticles and polymers on a commercial scale are still in their infancy stage but are attracting attention of many material scientists throughout the world. Microorganism-assisted biological synthesis is safe and economically viable prospect for novel material synthesis approach. Bacterial, fungi [33] or other microorganism-assisted synthesis can be used for polymer, metal nanoparticle [34, 35] or other diverse material [36] synthesis. Therefore, there is a demand to develop more "greener" routes for the synthesis of more advanced polymers such as PPy. Ideal conditions for PPy synthesis would be at neutral pH and in aqueous environment [37]. In order to fulfill these conditions huge interest is growing on synthesizing more environmentally friendly polymers. It has been reported that more environmentally friendly chemical oxidants, such as hydrogen peroxide (H_2O_2) could polymerize Py [38]. However, this polymerization is very fast and results in large quantities of side products. Other reported polymerization methods for PPy have included using catalytic amounts of ferric chloride hexahydrate ($FeCl_3 \cdot 6H_2O$) [39], iron porphyrin enzyme mimics [40], and the enzymes horseradish peroxidase (HRP), glucose oxidase, and laccase [41].

Nitroaniline however is not that widely analyzed and used in electrochemistry. Only recently some of the attention was turned towards electrochemical investigation of substituted anilines by electrochemical and spectrochemical techniques [42]. 3-Nitroaniline (3NA) from the isomeric anilines family differs due to having an electron withdrawing nitro group and an electron-donating amino group which is positioned in the meta position on the benzene ring. This gives rise to a somewhat smaller molecular dipole moment and a lower molecular hyperpolarizability compared to 4-nitroaniline [43]. 3NA crystallizes in noncentrosymmetric structures and shows large optical nonlinearity [44, 45], large electro-optic effect [46] and are widely used in simple nonlinear optical (NLO) materials [47]. Moreover, piezoelectric [48] and ferroelectric behaviors [49] were noticed in 3NA compounds. However, so far there are no known use of 3NA for the electrochemical sensor development.

1.2.2. Graphene oxide and multiwalled carbon nanotubes

Graphene oxide (GO) is a two-dimensional (2D) material with a honeycomb carbon structure composed of relatively large sp^2 carbon domains surrounded by some sp^3 carbon domains and/or oxygen containing hydrophilic functional groups such as epoxide, hydroxyl, and carboxyl [50]. Due to its unique chemical structure, GO shows excellent processability in aqueous environments, applicability for surface engineering, suitability for surface-enhanced Raman scattering (SERS) and fluorescence quenching based technologies [51]. These properties attracted interest in using this material for biological studies and creation of advanced graphene-based nanomaterials

[52, 53]. Recently GO received even more attention due to its ability to self-exfoliate into single sheets by simple incubation in water making the production of GO films possible straight from a water-based solution. This is a considerable advantage over the modification by fullerenes that requires high temperatures or vapor deposition for fullerene-based film formation. Due to these characteristics GO can be combined with plastics or other materials that are sensitive to high temperature [54]. Moreover, the functional groups of GO can be reduced to graphene-like nanosheets by chemical [55] and/or electrochemical reduction [56], thermal reduction [57], 'green chemistry' based reduction by using reducing biological materials [58], or reduction by applying intense light pulses [59]. The conductivity of reduced GO (rGO) is increased but it is not as high as exfoliated graphene since rGO has a higher number of various defects in its structure and not all attached functional groups are removed. A significant number of sp^3 hybridization possessing groups and structures and increased number of lattice defects remains in rGO induced by oxidation of graphene to GO, which is followed by the GO reduction process. On the other hand, functional groups that were not reduced can remain as chemically active defect sites, which can be used for further chemical modification [55].

Multiwalled carbon nanotubes (MWCNT) are allotropes of sp^2 hybridized carbon similar to fullerenes and shaped as cylindrical tubes made out of six-membered carbon rings similar to graphite which are stacked one in the other. There might be from 6 to 25 and more of such cylindrical tubes and due to that the diameter of MWCNT can reach up to 100 nm. MWCNT are known to be highly conductive, have high aspect ratio, physical properties of having an excellent tensile strength, thermal stability and high chemical stability [60]. Due to these properties MWCNT are being employed in many applications, such as: sensors and instruments, coatings, semiconducting materials, medical implants [61], etc.

Since the structure of the MWCNT is a nanotube, the whole weight is concentrated on its surface layers. This feature predetermines their electrochemical and adsorption properties [62]. High sensitivity of nanotubes electronic properties to adsorbed molecules and the unique surface unit makes them a promising material for the development of the superminiaturized chemical and biological sensors [63, 64]. The principle of these sensors is based on the V-I curves which depends on the adsorption of the specific molecules on the MWCNT surface. The use of MWCNT in the sensor design give the most promising applications in electronics. Moreover, sensors with MWCNT obtain fast response time and recovery [65].

1.3.Substrate modification for obtaining single cells

Budding yeasts cells (*Saccharomyces Cerevisiae*) serve as a bio-analytical target and model system to investigate single cells [66] and the mechanisms of

their attachment on different substrates. Yeasts are simple single cell microorganisms that are suitable for various manipulations, chemical treatment [67, 68], electrochemical, and electromagnetic perturbations [69, 70] and they are well growing in different media and are sticking to various surfaces. These criteria determined the application of yeast cells as one of the most extensively used eukaryotic models, which is often used for a better understanding of biological systems [71]. Yeast cell walls contains specialized surface proteins called ‘adhesins’ or ‘flocculins’ that are responsible for cell to cell and cell to surface adhesion. Cell adhesion is one of the most crucial ability that prevents cells from being washed away when a cell finds nourishing environment and allows forming biofilms with strong self-protection abilities [72]. These interactions include van der Waals, electrostatic, and hydrogen bonds [73] that create up to 25 μN averaged adhesion force per cell [74]. However not only proteins are known to form interactions with the specific substrates. The stacking π-π interaction between nucleotide bases of DNA can also be formed with the aromatic rings of graphene as shown in a previous report [75]. All these characteristics make yeast cells attractive and easy to analyze even immobilized on dry substrates in air at ambient conditions [76]. However, for better cell adhesion surface functionalization agents are required.

Cell imaging and investigation started immediately after the invention of optical microscopy, although mostly bulk samples containing high number of cells were analyzed. Recently the attention shifted towards the investigation and manipulation of single cells since it was understood that cells are individual microorganisms showing variations and distinct behavior with respect to that of the colony. It has been believed that the information obtained by analyzing large cell colonies is also representative for the behavior of individual cells. In the data obtained from bulk cell samples this phenotype-related information is averaged or even attributed to noise or statistical variations. However, by exposing genetically identical cells to the same environmental conditions multiple variations in molecular content and even phenotype can be observed at the single cell level [77]. In order to avoid this situation analysis at the single cell level is required.

Nowadays there exist several most frequently used techniques for the separation and immobilization of single cells. One of the common ways to immobilize cells is based on the contact trapping method by exploiting the ability of cells to adhere naturally or artificially after treatment by various chemicals [78-82]. However, using such technique there is a high chance to induce unknown phenotype variations. Therefore, it is very important to minimize these effects and optimal substrates with surfaces most suitable for cell-immobilization have to be selected carefully [83-85]. Beyond substrate engineering to investigate single cells, there are non-contact optical methods based on light trapping, the so-called optical tweezers where Raman spectra is obtained of the single cell interacting only with liquid environment [86].

2. Materials and methods

2.1.Chemicals

All chemicals of analytical grade and deionized water were used. All materials if not stated otherwise were obtained from Sigma Aldrich (Germany). *Streptomyces spp.* strains MIUG 12p and MIUG 4.88 were provided from the microbial Cultures Collection of the Bioaliment Research Center, Faculty of Food Science and Engineering of 'Dunarea de Jos' University of Galati, Romania (MIUG) [87]. Yeast cell strain *Saccharomyces cerevisiae* was obtained from EUROSCARF (Frankfurt, Germany), solid agar yeast extract-agar media was purchased from Merck (Germany). Graphene oxide (GO) was purchased from ACS Materials (USA) and potassium chloride (KCl) was received from Scharlau Chemie S.A. (Spain).

Nanomaterials that were used for electrochemical Cu(II) detection (GO, graphene (G), magnetite (Fe_3O_4), gold-chitosan (AuChts) were synthesized using the purest available chemicals, which were additionally purified by procedures described in other references [88-91].

2.2.Experimental part

2.2.1. Polypyrrole synthesis

2.2.1.1. Green synthesis of polypyrrole

Growth medium was prepared with agar (solid) and without (liquid). Both growth mediums were sterilized in autoclave for 20 min. at 121°C. The culture suspension from solid growth medium was transferred with sterile loop into 250 ml Erlenmeyer flask with 100 ml of liquid growth medium and for 10 days was placed on the shaker with controlled speed of 150 rpm and temperature of 25°C. For the estimation of the optimum pyrrole concentration in the bacteria medium after 6 days of incubation several concentrations: 10, 20, 30, 40, 60 and 80 mM of Py were added leaving one to be control sample. Bacteria medium with added Py and control sample without Py left on the shaker for 4 more days. For more information about the experimental details please check in Stirke, Apetrei, Kirsnyte, Dedelaite, Bondarenka, Jasulaitiene, Pucetaite, Selskis, Carac and Bahrim [92] page 100.

2.2.1.2. Electrochemical synthesis of polypyrrole

For comparison with the green synthesized PPy, there were also PPy synthesized electrochemically using potentiostat PGSTAT 30 Autolab (Netherlands). For that 3-cell electrode system was used where platinum (Pt) was working electrode, Ag/AgCl reference electrode and Pt – counter

electrode. For more information about the experimental details please check in Stirke, Apetrei, Kirsnyte, Dedelaite, Bondarenka, Jasulaitiene, Pucetaite, Selskis, Carac and Bahrim [92] page 100-101.

2.2.2. Electrode modification for Cu(II) detection

In this study, electrode for Cu(II) ion detection by stripping voltammetry is suggested and evaluated. Electrochemical measurements were performed using a Gamry Reference 750 Potentiostat/Galvanostat from Gamry Instruments (USA) equipped with a C3 cell stand. Glassy carbon electrodes of 0.071 cm^2 geometric area were used as working electrodes. Pt wire was used as a counter electrode. Ag/AgCl in saturated KCl (Ag/AgCl/($KCl_{sat.}$)) was applied as a reference electrode for the experiments, which were performed in aqueous media; or an Ag/Ag^+ in 10 mM $AgNO_3$ ($Ag/AgNO_3$) was applied for the experiments, which were performed in non-aqueous media. In order to renew the surface of glassy carbon (GC) electrode was hand polished as it was described before [93, 94]. Electrochemical modification of the electrode was performed with Gamry PCI4/750 potentiostat. Modification protocol was carried by using 3NA and performed by 100 reversible potential cycles in acetonitrile (CH_3CN) including tetrabutylammoniumtetrafluoroborate (TBATFB) solution. The obtained GC/3NA electrode was then used as it is or electrochemical reduction of nitro groups was then performed. Then bare or modified electrodes surface was modified with nanomaterials using drop method before and after 3NA reduction. Stable potential (STB POT) was applied followed by differential pulse voltammetry (DPV) for the developed electrodes. Several electrodes were prepared and analyzed. Most optimum electrode was further evaluated for selectivity to other metal ions, as well as stability, reproducibility, repeatability and sensibility. More detailed experimental description is in Dedelaite, Kizilkaya, Incebay, Ciftci, Ersoz, Yazicigil, Oztekin, Ramanaviciene and Ramanavicius [95] page 280-281.

2.2.3. Substrate preparation for obtaining single yeast cells

GO chemically prepared by the Hummers method [88, 96] with a flake size of about 0.5 – 5.0 μm and dispersed in ethanol at a concentration of 5 g/L. For surface modification with GO five different samples were chosen: objective glass slides, polished silicon wafers (100, p-type), highly orientated pyrolytic graphite (HOPG), mica, and polydimethylsiloxane (PDMS). GO solution was dropped on the sample and air dried. More detailed experimental description is in Dedelaite, Rodriguez, Andriukonis, Hietschold, Zahn and Ramanavicius [97] page 280-281.

2.2.4. Sample fabrication for SERS substrate

SERS substrates with bidirectional localized surface plasmon resonances (LSPR) were obtained by two step routine fabrication. First step is ripple pattern production on silicon substrate by iron irradiation with a Kaufman type ion-source in a vacuum chamber. After the irradiation process is finished silicon substrate with surface ripple structures with the periodicity of 50 nm and low defect density is then obtained [98]. Second step is gold (Au) deposition done in oblique-angle by electron-beam deposition in a high vacuum chamber (BesTech, Germany). Additionally, one sample was annealed in air on a conventional heat plate for 1 h at 400°C. More details about the experiment is provided in Schreiber, Gkogkou, Dedelaite, Kerbusch, Hubner, Sheremet, Zahn, Ramanavicius, Facsko and Rodriguez [99] page 22570-22571.

2.2.5. Surface analysis methods

2.2.5.1. Static contact angle measurements

The static contact angle measurements were carried out using an OCA-20 contact angle meter (Data Physics Instruments GmbH, Filderstadt, Germany) with the sessile drop method at room temperature and under air atmosphere. Deionized water was applied for all contact angle measurements.

2.2.6. Optical methods

2.2.6.1. Optical microscopy

The sample of bacteria with PPy for morphological analysis was prepared by centrifugation of 1 mL of bacteria medium after 6 and 10 days of incubation with added pyrrole and the obtained sediment used for optical microscopy. The analysis was performed using optical microscope OLYMPUS BX51 (Japan).

Yeast cell drying process was observed using digital microscope Keyence VH-Z100 (USA) at 100x and 1000x magnification.

2.2.6.2. Scanning electron microscopy

The morphology of PPy microspheres was analyzed using dual beam system Helios Nanolab 650, (FIB-SEM), FEI. Sample was placed on a gold slide and covered with platinum foil.

Top view of the ripple pattern on the silicon substrate with the Au structures was taken by Raith e_Line plus with a Zeiss Gemini optics.

2.2.6.3. Transmission electron microscopy

Cross-sectional transmission electron microscopy (TEM) images were taken by using an image C_s- corrected Titan 80-300 microscope FEI Itd (Netherlands). More details about the method is in Schreiber, Gkogkou, Dedelaite, Kerbusch, Hubner, Sheremet, Zahn, Ramanavicius, Facsko and Rodriguez [99] page 22571.

2.2.6.4. Atomic force microscopy

The surface of glass modified glass with GO and rGO substrates were imaged using atomic force microscopy (AFM). An OmegaScope SPM (AIST-NT, USA) was employed in contact mode with conventional silicon cantilevers.

The topography of the ion-induced ripple pattern was measured by using AFM in tapping mode (Bruker MM8 AFM with PPL-NCRL tips from Nanosensors).

2.2.6.5. Fourier transform infrared spectroscopy

The samples for Fourier transform infrared spectroscopy (FTIR) were prepared using two different method. KBr pellet method prepared samples for obtaining spectra "BRUKER VERTEX70" FTIR (USA) was used with globar IR emitter, liquid nitrogen cooling mercury cadmium telluride sensor and KBr ray divider. Whereas samples prepared using attenuated total reflection (ATR) method were analyzed using "BRUKER ALPHA" FTIR (USA) spectrophotometer that uses global IR emitter, DTGS sensor and KBr ray divider. More details about the measurements are in Stirke, Apetrei, Kirsnyte, Dedelaite, Bondarenka, Jasulaitiene, Pucetaite, Selskis, Carac and Bahrim [92] page 101.

2.2.6.6. X-ray photoelectron spectroscopy

X-ray Photoelectron Spectroscopy (XPS) for the characterization of surface composition of microspheres was performed with a spectrometer ''ESCALAB MK II'' VG Scientific (Great Britain). For that pure Py, electrochemically synthesized polypyrrole (EPPy) and bacterial synthesized polypyrrole (BPPy) (microspheres) samples were prepared by spreading PPy as thin layer on gold covered chip and placing the chip in incubator (+25°C) for 30–60 min to dry. More details about the measurements are in Stirke, Apetrei, Kirsnyte, Dedelaite, Bondarenka, Jasulaitiene, Pucetaite, Selskis, Carac and Bahrim [92] page 101.

2.2.6.7. Ellipsometer and reflectance measurements

Spectroscopic ellipsometry of the rippled silicon substrate was performed with a J.A. Woollam M-2000FI ellipsometer under ambient conditions. Angle of incident was set to 75° and measurement was done 100 times per spectra.

2.2.6.8. Raman Spectroscopy

Raman spectroscopy experiments for obtaining signal from yeast cells and CoPc were performed with a micro-Raman spectrometer LabRam HR800 (HORIBA, France) and XploRA (HORIBA, France). Several excitation laser lines were used: 514.7 nm, 632.8 nm, 532.0 nm, 638 nm and 785 nm. The laser intensity measured at the sample was set to 1 mW and 105 μW for the 514.7 nm and 532.0 nm, respectively. For obtaining spectra of yeast cells a 100x objective (numerical aperture, N.A. = 0.9), whereas for CoPc – 50x LWD objective (N.A. = 0.5) with laser power on a sample of 1 mW.

2.2.6.9. Static contact angle measurements

The static contact angle measurements were carried out using an OCA-20 contact angle meter (Data Physics Instruments GmbH, Filderstadt, Germany) with the sessile drop method at room temperature and under air atmosphere. Deionized water was applied for all contact angle measurements.

2.2.3. Finite Element Method Calculations

For FEM wave optics module in COMSOL Multiphysics 4.4 was used. Using Gryddion the particle geometry was extracted by masking then and saved as .dxf files (by Python 2.7 and OpenCV). More information is in the Schreiber, Gkogkou, Dedelaite, Kerbusch, Hubner, Sheremet, Zahn, Ramanavicius, Facsko and Rodriguez [99] page 22571.

3. Results and discussion

3.1.Polypyrrole synthesis using Streptomycess spp. bacteria

3.1.1. Polymer formation

Optimum concentration for the PPy synthesis was analyzed by adding different concentrations to the bacterial medium after 6 days of incubation and observing changes in the medium. After 10 days of incubation flasks became darker with the concentration of 30 mM and higher. For further synthesis 30 mM pyrrole concentration was used.

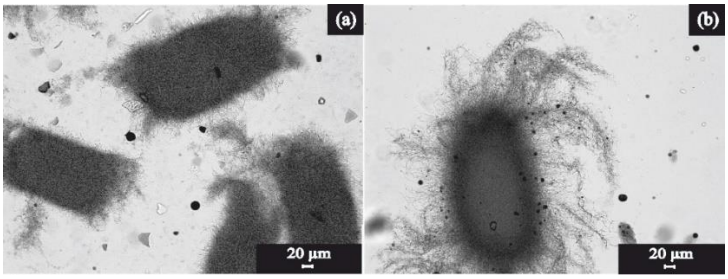

Figure 1. *Optical microscopy images of PPy microspheres synthesized by Streptomyces spp.: (a) MIUG 12p strain; (b) MIUG 4.88 strain.*

OM was used to investigate black formations and strain viability. The bacterial strains increased development was observed on the 4th day and on the 8th day it became stationary even with the pyrrole monomer present in the medium. The added monomer shows no effect on the strain growth.

The black formations in the bacterial medium was noticed 2 days after the monomer addition. In the Figure 1 black 10-20 µm diameter microspheres are visible around the bacteria colonies. The size of the microspheres depends on the bacteria strain. In the MIUG 12p strain medium microspheres appear around 20 µm, whereas in the MIUG 4.88 – only around 10 µm. Furthermore, the concentration of the PPy microspheres obtained in MIUG 12p medium was 8 times lower compared with the concentration in MIUG 4.88 medium. This could be attributed to earlier PPy microsphere formation in MIUG 12p medium which gave time to aggregate. Depending on the synthesis method PPy particle sizes can vary [100-102].

3.1.2. FIB-SEM PPy microsphere imaging

The PPy microspheres were analyzed using FIB-SEM technology. Top view and cross-section images are presented in Figure 2. From the FIB-SEM images it's visible that microspheres obtained with MIUG 4.88 bacteria strain is not as resistant and bends under the vacuum. Moreover, cross-section of the microspheres showed that formations with MIUG 12p strain are denser

compared to the ones obtained with MIUG 4.88. This could be since synthesis of PPy in MIUG 12p medium starts earlier, which leads to microspheres being bigger and denser than the ones obtained in MIUG 4.88 medium. Also, FIB-SEM analysis showed that PPy microspheres are hollow unlike PPy particles obtained by other synthesis methods. Obtaining hollow PPy microspheres throughout biocatalytic synthesis is a feature attractive to many applications [103-108].

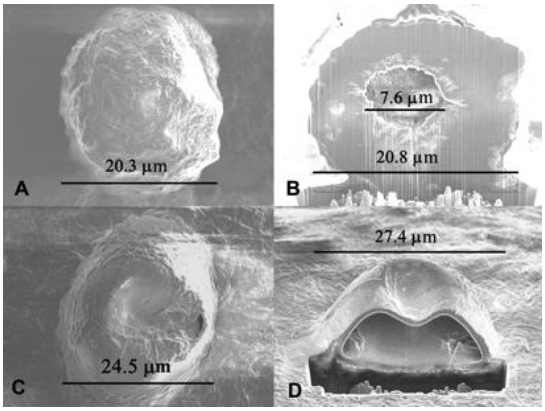

Figure 2. *FIB-SEM images of PPy microspheres obtained by incubation Streptomyces spp. based medium: (A, B) MIUG 12p strain; (C, D) MIUG 4.88 strain. A, C – top view; B, D – cross section, view angle 53°.*

3.1.3. FTIR spectra

FTIR was used to identify chemical bonds in microspheres by producing an infrared absorption spectrum [109]. Spectra of pure Py, bacterial synthesized PPy (BPPy) and electrochemically synthesized PPy (EPPy) were obtained and presented in Figure 3. Both spectra of BPPy and EPPy exhibits characteristic peaks of polypyrrole. The peak shift in BPPy microsphere spectra could be due to additional products in synthesis solution, such as starch, and/or presence of bacterial bioproducts.

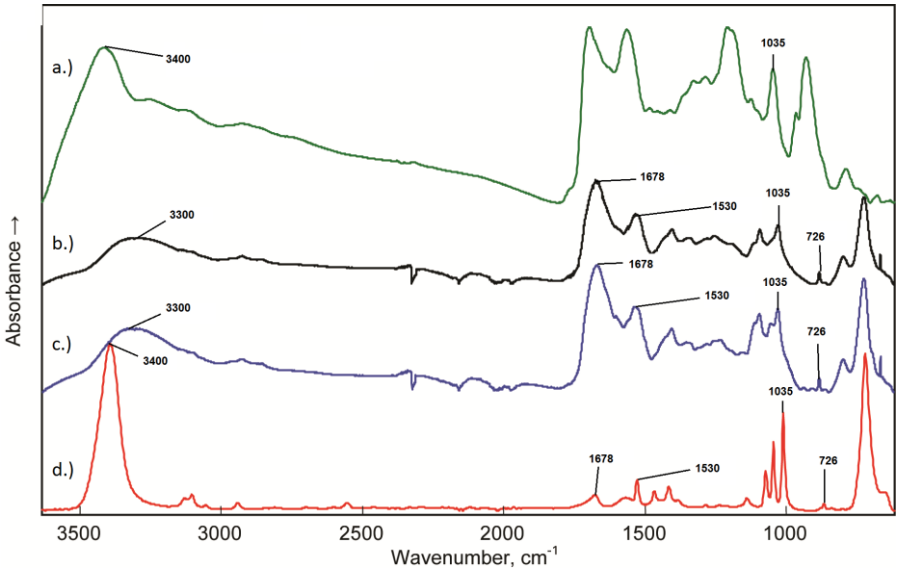

Figure 3. *FTIR spectrum of PPy synthesized: (a) electrochemicaly; (b) MIUG 12p strain; (c) MIUG 4.88 strain; (d) Py with marked peaks that are characteristic to PPy.*

3.1.4. X-ray photoelectron spectroscopy

XPS spectrum of BPPy was taken and was compared with EPPy and Py (Figure 4). The carbon region binding energies corresponds to the ones found in PPy except the one at ~286 eV which corresponds carbon in hydroxyl group (C-OH) [110]. Such group could be found if some PPy derivatives such as furan, furfural, N-methylpyrrole, porphobilinogen, pyrrole-3-carboxylic acid, and so on has formed [111-113]. The groups fitted in the oxygen region are the same groups that could be found in the PPy derivatives mentioned before, such as carbonyl, carboxynil/N [114]. Water in the samples could appear from the atmosphere or during synthesis and highest amount of water content is found in EPPy. The nitrogen region could be deconvoluted into three peaks that corresponds to nitrogen in imine state (– NH =), amine nitrogen (– NH –) [110], and imidogen cation (– NH^+ –) [115, 116]. From XPS fitting the relative concentrations of carbon, nitrogen, and oxygen ions, which are involved in various chemical bonds, are shown in Figure 4d,e,f. From these images we can conclude that the total content of the nitrogen is highest for the Py. Moreover, in Figure 4d the content of the Py can be calculated for all the samples. Since the concentration of C-N bonds is lower than the sum of C-C/C-H and C-OH bonds it can be concluded that concentration of pure Py is lower than the concentration of its' derivatives. High carbon concentration in the samples can be explained by the carbon absorption from the environment. However, after analyzing all spectra it may

be concluded that XPS obtained from BPPy is similar and practically don't differ from the XPS obtained from EPPy [117].

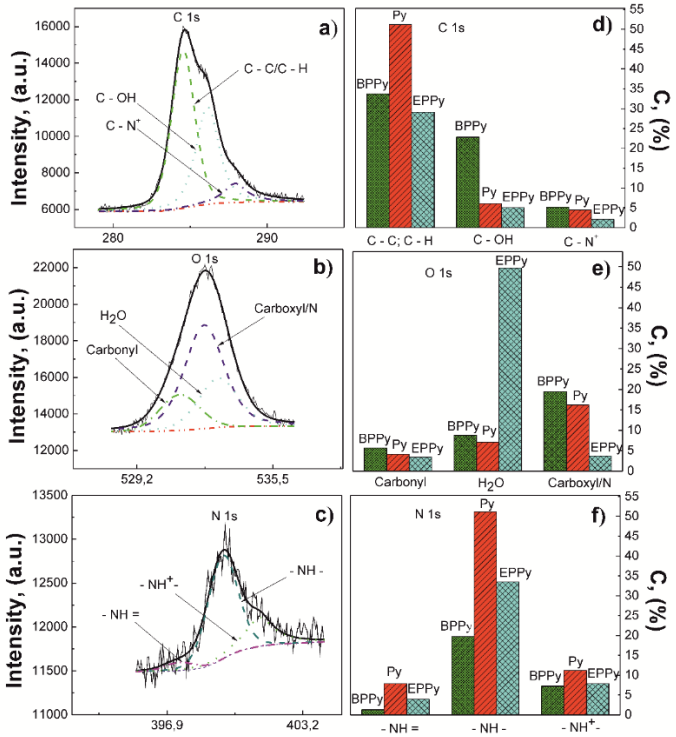

Figure 4. *XPS spectra of BPPy of (a) C 1s; (b) O 1s; (c) N 1s; histograms of relative concentration of (d) carbon ions in various chemical bonds (BPPy, Py, EPPy); (e) oxygen ions in various chemical bonds (BPPy, Py, EPPy); (f) nitrogen ions in various chemical bonds (BPPy, Py, EPPy).*

Figure 5 depicts the concentrations of C, O and N in all the compounds and from that chemical formulas could be written for BPPy as $C_{0.617}N_{0.043}O_{0.34}$, for Py - $C_{0.618}N_{0.107}O_{0.275}$, and EPPy - $C_{0.363}N_{0.069}O_{0.568}$. However, water content plays high role and should be added into the formulas simultaneously decreasing the content of oxygen. Then the general formulas of BPPy, Py, and EPPy must be written as $C_{0.617}N_{0.043}O_{0.31}\cdot 0.03H_2O$, $C_{0.618}N_{0.107}O_{0.256}\cdot 0.019H_2O$, and $C_{0.363}N_{0.069}O_{0.286}\cdot 0.282H_2O$ respectively. From these formulas oxygen content in all the compounds is approximately equal to 0.3, which means that the quantity of PPy derivatives is the same for all the investigated samples and pyrrole is a hydrated compound.

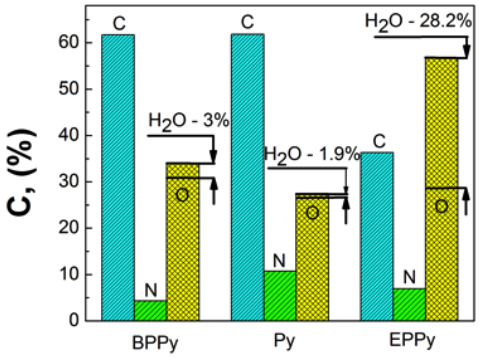

Figure 5. *Histogram of carbon, nitrogen, and oxygen concentrations in investigated compounds (H_2O – X % – relative concentration of water molecules).*

3.2.3-nitroaniline and multiwalled carbon nanotubes modified electrode for Cu(II) ions detection

3.2.1. Electrode modification with 3NA and GO for Cu(II) detection

Adsorption and electrochemical deposition followed by reduction of functional groups on the modified GC electrodes' surface were combined for electrochemical detection of Cu(II) ion. The interaction mechanism of the Cu(II) ions and the amino groups can be explained by interaction of amino groups and Cu(II) ions and formation of chelate complex (Figure 6), which is taking place on modified electrode surface. On the other hand, the efficiency of 3NA modified surfaces was enhanced by nanomaterials, which were applied in this research.

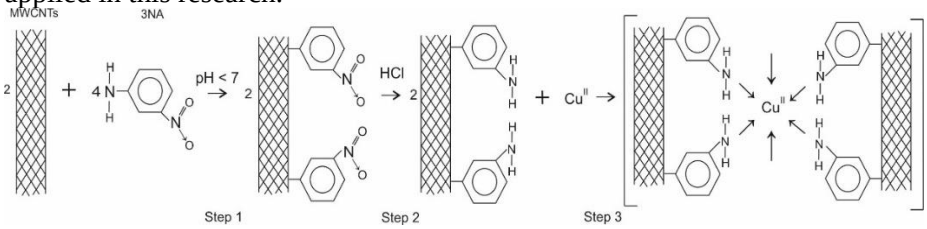

Figure 6. *Reaction scheme of (1) 3NA electrochemical modification on MWCNT, (2) nitro group electrochemical reduction to amino groups and (3) Cu(II) reduction.*

For this aim, number of differently modified electrodes was prepared by the deposition of NMs before or after electrochemical modification with 3NA; the electrodes were classified into several groups: (I) bare GC; (II) GC modified with 3NA (GC/3NA); (III) GC modified with electrochemically reduced 3NA (GC/3NA(red)); (IV) GC/3NA additionally modified with

nanomaterial (GC/3NA/NMs); (V) GC/3NA(red) additionally modified with nanomaterial (GC/3NA(red)/NMs), (VI) GC/NMs modified with 3NA (GC/NMs/3NA); (VII) GC/NMs modified with electrochemically reduced 3NA (GC/NMs/3NA(red)). Then these electrodes were applied for the electrochemical determination of Cu(II) ions. Firstly, GO modified electrodes were evaluated. DPV results, which are shown in Figure 7, illustrate that the highest DPV peak was observed at - 0.06 V towards Cu(II) ions with GC/NMs/3NA(red) electrode. GC/GO/3NA(red) electrode is 6 times more sensitive towards Cu(II) ions compared to bare GC electrode. The reason of this advanced sensitivity is related to larger electrochemically active surface, which has been increased by GO. Other researches also noticed some advantages of electrodes modified by carbon nanomaterials [118, 119].

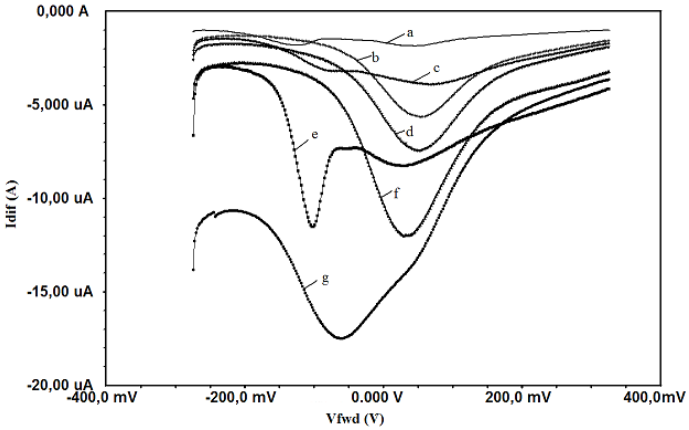

Figure 7. *Differential pulse voltammograms of copper at Bare GC* ***(a)****; GC/3NA* ***(b)****; GC/3NA(red)* ***(c)****; GC/3NA/GO* ***(d)****; GC/3NA(red)/GO* ***(e)****; GC/GO/3NA* ***(f)****; GC/GO/3NA(red)* ***(g)*** *electrodes recorded in BR buffer solution, pH 5.0* vs *Ag/AgCl/KCl*$_{sat}$.

3.2.2. Optimization of the nanomaterials for electrode modification

As it is seen in Figure 7, the modification of GC by GO before electrochemical modification procedures enhances current responses compared with that of GC/3NA and GC/3NA(red) electrodes. Therefore, another step of this research was to determine nanomaterials which are the most efficient in electrochemical determination of Cu(II) ion. Five different nanomaterials were chosen for this aim: GO, G, Fe_3O_4, AuChts and MWCNT and five different electrodes were prepared for this part of research and their electrochemical responses towards Cu(II) ions were compared with bare GC and GC/3NA(red) electrodes.

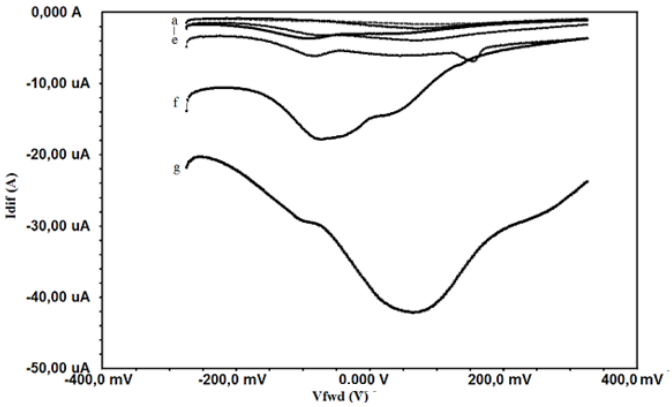

Figure 8. *Differential pulse voltammograms of copper at GC/NPs/3NA(red) electrodes: Bare GC (a); GC/3NA(red) (b); GC/Fe_3O_4/3NA(red) (c); GC/AuChts/3NA(red) (d); GC/Graphene/3NA(red) (e); GC/GO/3NA(red) (f); GC/MWCNTs/3NA(red) (g) recorded in BR buffer solution, pH 5.0 vs Ag/AgCl/KCl_{sat}.*

DPV results (Figure 8) showed that analytical signal registered by GC/MWCNT/3NA(red) at +0.05 V electrode increases twice when compared with that registered with GC/GO/3NA(red). This effect is related to properties of MWCNT. Since the MWCNT can adsorb ions and molecules, exhibit strong adsorptive ability towards other species and increase their surface concentration [120]. Therefore, further experiments were carried using GC/MWCNT/3NA(red) electrode.

3.2.3. Characterization of the electrode

The characteristics of the sensing systems such as selectivity, repeatability, reproducibility and stability are important as much as sensitivity. For this reason, all further experiments were performed, and the results were evaluated while applying statistical analysis. The investigation of sensitivity of the GC/MWCNT/3NA(red) electrode towards binding of Cu(II) ions was carried out in the presence of other interfering metal ions (Zn(II), Cd(II), Pb(II), Mn(II), Co(II), Fe(III)). When other ions were presented at the same concentration as Cu(II) ions, their interfering effect decreased in following order: Co(II)>Mn(II)>Fe(III)>Cd(II)>Pb(II)>Zn(II). When all these metal ions at 1 mM concentrations were applied simultaneously with Cu(II) ions, the interference towards Cu(II) ions determination increased up to 40%. Also, no additional peaks were visible in related potential range. In order to perform exact determination of interfering metals that are present in the sample together with Cu(II) ions it is essential to know the potentials of current peaks of interfering ions (Table 1).

Table 1. *Interference of various metal ions to DPV-based analytical signal of GC/MWCNT/3NA electrode registered in BR buffer, pH 5.0* vs *Ag/AgCl/KCl$_{sat}$.*

Ions	Concentration (mM)	DPV peak current (μA)	Relative difference from 1 mM Cu^{2+}
Cu^{2+}	1	-42.12	0
All metals	1	-25.38	40%
Co^{2+}	1	-26.63	37%
Mn^{2+}	1	-27.71	34%
Fe^{3+}	1	-31.50	25%
Cd^{2+}	1	-33.60	20%
Pb^{2+}	1	-32.22	27%
Zn^{2+}	1	-36.13	14%

During the investigation of the stability of GC/MWCNTs/3NA(red), electrode was kept at +4°C temperature for 0, 1, 5 and 14 days in closed vessel with Ar gas and their sensitivity towards Cu(II) ions has been investigated using DPV. It has been noticed that the stability of analytical signal of electrode was decreasing gradually and after 5 days it became stable. After 14 days of incubation GC/MWCNTs/3NA(red) remained at 50% level of its' original electrochemical response towards Cu(II) ions (Figure 9).

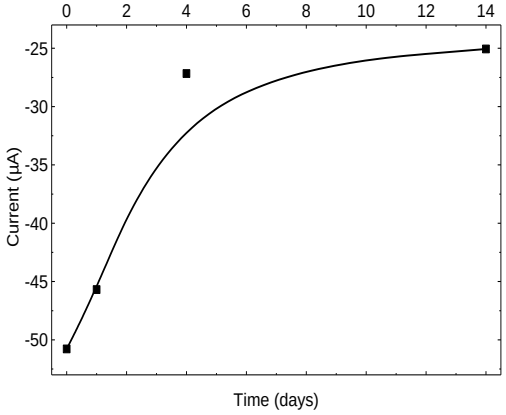

Figure 9*. Stability of DPV-based analytical signal of GC/MWCNTs/3NA(red) electrode in BR buffer solution, pH 5.0* vs *Ag/AgCl/KCl$_{sat}$.*

Repeatability of differently modified electrodes in Cu(II) ion detection was tested using three similar electrodes prepared at same conditions. Relative standard variation (R.S.V.) of this test was 6.4%, and R.S.V. of the reproducibility test was 1.4%. After the evaluation of repeatability and reproducibility results obtained by various electrodes applied in Cu(II) detection, which have been reported in some other researches and comparing them with the obtained in the frame of this article, it was

determined that here reported GC/MWCNT/3NA(red) electrode can compete in the determination of Cu(II) ions with other electrodes [121, 122].

3.2.4. Limit of detection of developed electrode towards Cu(II) ions

Finally, the GC/MWCNT/3NA(red) electrode was evaluated for the limit of detection (LOD) value towards Cu(II) ions. The determination of Cu(II) ions was performed for three times and standard deviation values were calculated. LOD of the GC/MWCNT/3NA(red) electrode was 0.5×10^{-9} M Cu(II) ions concentration. Sensitivity of the electrode manufactured in this experiment is as sensitive as other electrodes that are presented in other publications [123-125].

3.3.Obtaining single cell and its Raman analysis

3.3.1. Yeast cell solution drying observation

Five different materials: glass, silicon, HOPG, PDMS, and mica were chosen as substrates for single cell immobilization. The drying process was observed in ambient conditions and the results are presented in Figure 10. It was observed that on the pristine substrates, during water evaporation, cells that are immersed in the droplet due to water surface tension were swept across the surface and formed aggregates at the end of drying.

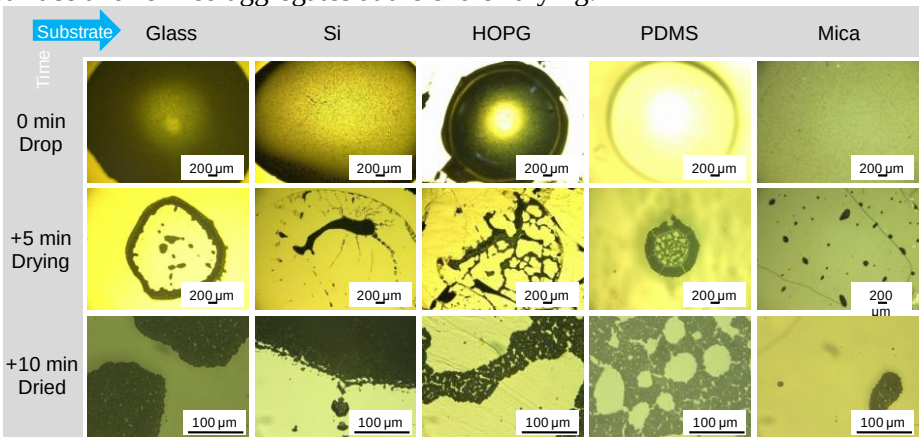

Figure 10. *Drying process of yeast cell suspension, which was prepared by dispersion of yeast cells in water and then drop coated on clean substrates such as: glass, silicon, HOPG, PDMS, and mica. Pictures were taken before and after water evaporation proceeded at ambient conditions over 5-10 min.*

As can be seen from Figure 10 intricate yeast cell agglomerates are formed on all substrates. GO was chosen for the modification of the

mentioned substrates due to its unique chemical properties and biocompatibility [126]. The drying process of the yeast cell suspension on the modified with GO surfaces was observed (Figure 11). Unlike pristine substrates, the GO modified surfaces remarkably reduced the cell aggregation and increased the regions containing separated single cells. This is an indication of the enhanced cell adhesion on GO-based surfaces and form singlets and small colonies allowing to perform analysis at the single cell level.

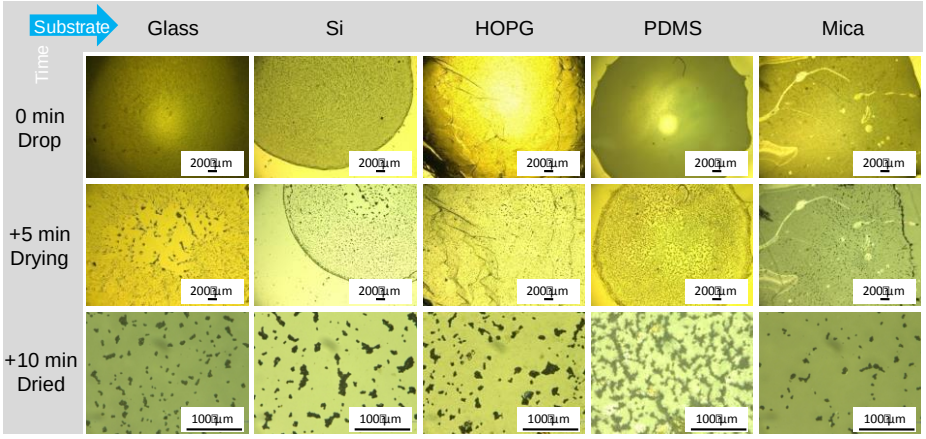

Figure 11. *Visualization of the drying process of yeast cell suspensions drop coated on the surfaces of GO modified substrates. Pictures were taken before and after water evaporation proceeded at ambient conditions over 5-10 min.*

The mechanisms behind such improved single cell addition were investigated and some most plausible reasons was identified: 1) increased mechanical friction between cells and GO-modified surfaces due to roughness of GO films, 2) changes in hydrophobicity of the substrates which alters the drying process of the solvent, 3) increased electrostatic interaction between charged parts of yeast cell walls and carboxyl, carbonyl, and hydroxyl groups of GO, and 4) possible chemical interaction between carbonyl and hydroxyl groups of GO and the cell surface. In order to investigate these mechanisms in more detail we performed AFM, contact angle measurements, and studied a GO-coated surface after thermal reduction.

3.3.2. Increase in surface roughness

The surface roughness can increase or decrease the contact area between a cell and the substrate surface, which is proportional to the solid-liquid interfacial adhesive force [127]. Therefore, for surface roughness measurements contact mode AFM imaging was performed on pristine glass and glass coated with GO. Images of GO coated glass showed a heterogeneous surface with planar and wrinkled surface areas (Figure 12b). The cross section of a graphene

oxide nanosheet proved that the thickness of GO is around (1.7 ± 0.1) nm. Even though, due to natural stacking into multiple layers and formation of wrinkles and folds the root mean square roughness is only (1.5 ± 0.2) nm compared to the clean glass surface with a roughness of (0.4 ± 0.2) nm. In comparison with the micrometer range cell size (ca. 4 µm), the nanometer roughness difference between reduced and pristine GO can be expected to be insignificant to mechanically immobilize cells.

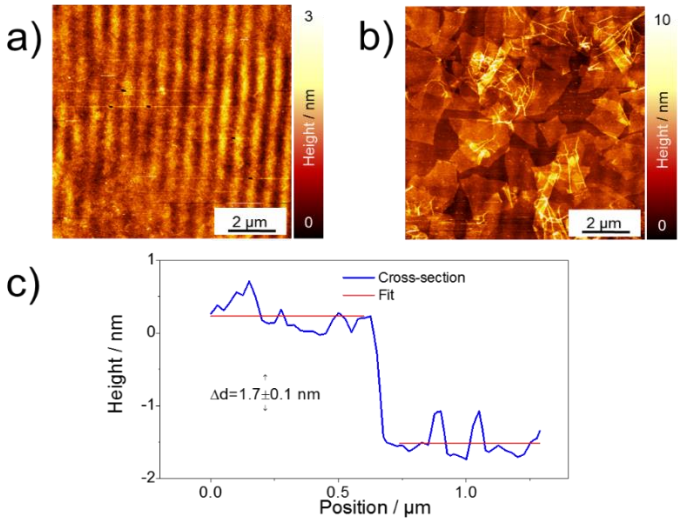

***Figure 12**. AFM images of glass (a) and glass modified with GO (b) surface roughness and cross section (c) of the GO – substrate.*

3.3.3. GO hydrophilicity

GO is known to be a hydrophilic material due to the presence of oxygen groups on its basal plane and edges, hence we can expect that it changes the hydrophilic properties of the substrate that could be the origin of the difference in cell adhesion. For this reason, water contact angle measurements were performed. This analysis revealed that the layer of graphene oxide increases the substrate hydrophilicity by 14 – 69%, (Figure 13). However, we cannot conclude that the surface hydrophilicity is the parameter that defines isolation of cells since GO-coated samples do not display a unique value but show different contact angles in the range of 12.6° ± 0.6° to 41.3° ± 0.4° which also partly overlap with the contact angle of the surfaces before the GO modification.

	Glass	Si	HOPG	PDMS	Mica
Without GO					
	47.8° ± 0.9°	47.7° ± 0.3°	86.7° ± 0.6°	110.8° ± 0.6°	15.9° ± 0.5°
With GO	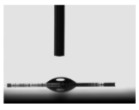				
	41.3° ± 0.4°	39.8° ± 0.4°	30.2° ± 0.2°	34.0° ± 0.3°	12.6° ± 0.6°

Figure 13. *Water contact angle measurements on pristine substrates (1st line) and modified with GO surfaces (2nd line).*

3.3.4. Chemical functionality of GO

The yeast cell surface contains proteins that can create attractive interactions with functional groups present at the substrate, in this case – the basal plane of GO. In order to test this assumption, we compared the aggregation of yeast cells on both GO and thermally reduced GO (rGO), which contains a much lower concentration of functional groups on its surface. AFM images and Raman spectra before and after reduction of GO were taken under excitation by a 514.7 nm laser.

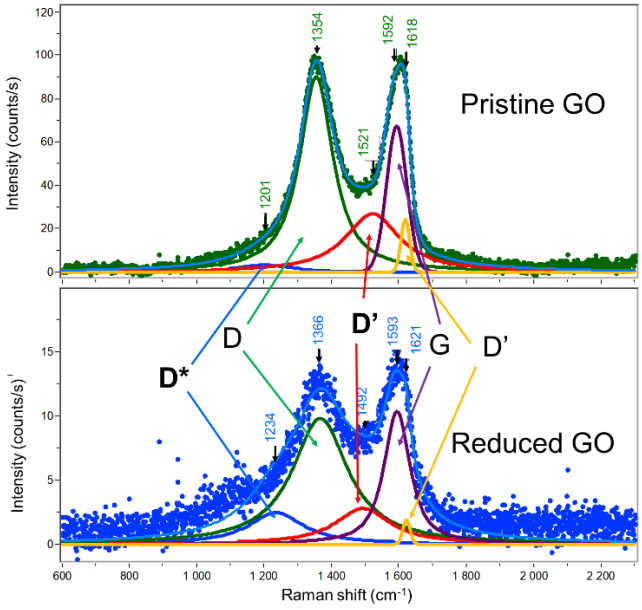

Figure 14. *Raman spectra analysis of the GO film before and after thermal reduction at 400°C for 30 min. The bands D* and D'', upshift and downshift, respectively, with the reduction level.*

The Raman spectra of GO and rGO presented in Figure 14 show characteristic D and G bands, which arise from sp^2 and sp^3 vibrations, and some other peaks that arise due to defects in the carbon-based structure. In this study, both Raman bands were fitted using a total of 5 peaks (mixed Gaussian/Lorentzian fit) which were marked to allow differences to be tracked. D* and D" after GO thermal reduction into rGO shift towards higher and lower wavelength numbers, respectively, which indicates the decrease of oxygen content [128]. G shift towards higher wave numbers can be explained due to amorphisation of the graphite structure. Additional D' peak rises from structural variety of the sample sp^2 hybridization [129]. Moreover, band related to amorphous phase marked as D" intensity decreases 10 time due to increased crystallinity [128, 130]. The AFM image in Figure 15 shows that GO nanosheets were significantly reduced during thermal annealing although some structural changes in the form of newly formed rods and particles were also observed. These results confirm that the reduction of GO was successful and that most of the functional groups were reduced.

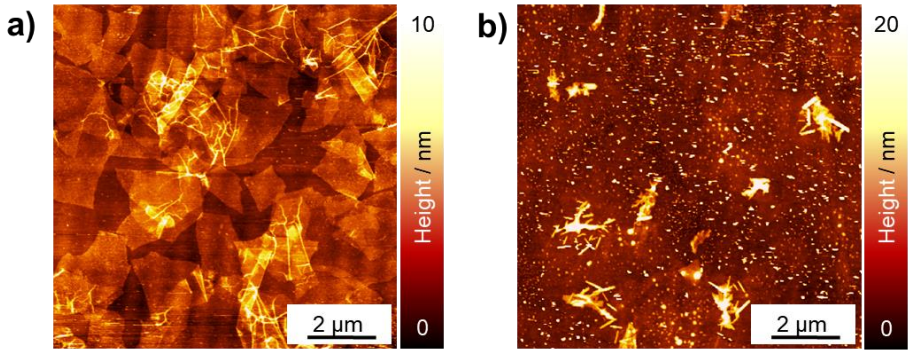

Figure 15. *AFM images of a) graphene oxide and b) thermally reduced graphene oxide.*

Yeast cell adhesion on rGO-modified surfaces was tested. It was observed that on the rGO-modified surface, yeast cells behave the same way as on the pristine glass substrate (Figure 16). Given that the roughness increased from 1.6 nm to 4.5 nm after the thermal reduction of GO was performed (as deduced from AFM), and that such increased roughness resulted in poorer cell adhesion, then we can conclude that the roughness effects are too small to play a significant role in our case. These results on rGO thus provide essential evidence to support our hypothesis that the functional groups on GO are responsible for the stronger interaction between cell wall and GO-coated surfaces. This can be explained by chemical heterogeneities between the cell wall and the GO-modified surface, which creates localized sites where interaction energies at the interfacial area are higher making adhesion more efficient [131].

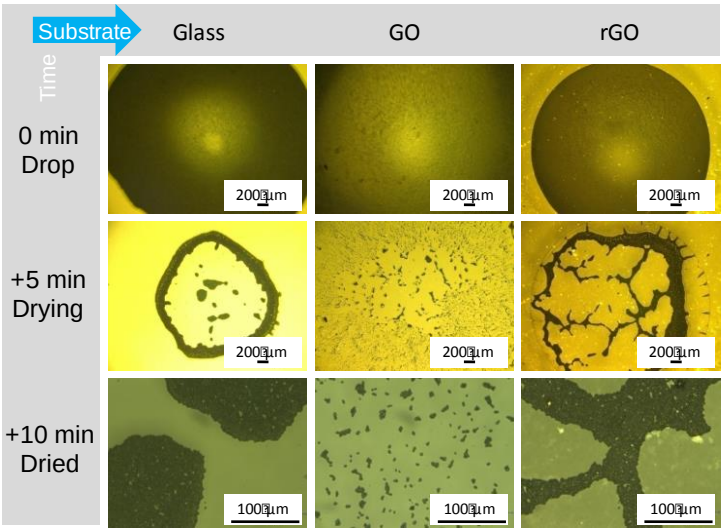

Figure 16. *Visualization of drying process of yeast cell suspension drop coated on GO and rGO modified substrates. Pictures were taken before and after water evaporation proceeded at ambient conditions over 5-10 min.*

3.3.5. Evaluation of the Raman spectra of single yeast cells immobilized on GO-modified surfaces

Raman spectra of single and aggregated cells immobilized on glass and GO-modified glass surfaces were registered under 532.0 nm laser excitation and are presented in Figure 17. While comparing the yeast spectrum obtained for yeast cells immobilized on glass with that obtained for yeast cells immobilized on a GO-modified glass substrate it was observed that the GO modification improves the Raman signal by 100%. This increase in intensity is likely due to the enhancing properties of GO-based layers [132]. Moreover, these Raman spectra prove that the spectrum registered from a single cell provides more information than the one from aggregated cells. In the spectra registered from single and aggregated yeast cells immobilized on GO-modified glass substrates there are obvious differences in peak positions and intensities. In the spectrum of a single yeast cell immobilized on a GO-modified glass substrate the low intensity peaks at 1260 cm^{-1} and 1294 cm^{-1} are observed. These peaks are attributed to C-H deformation in proteins and lipids which are likely to be sensitive to the cell-cell interaction. The peaks at 1548 cm^{-1} and 1601 cm^{-1} are also visible only in the spectra registered from single cells. These peaks are attributed to nucleic acids and lipids, respectively [133]. Moreover, the peak at 1601 cm^{-1} reflects the respiratory activity of mitochondria and can be associated with cell viability [134].

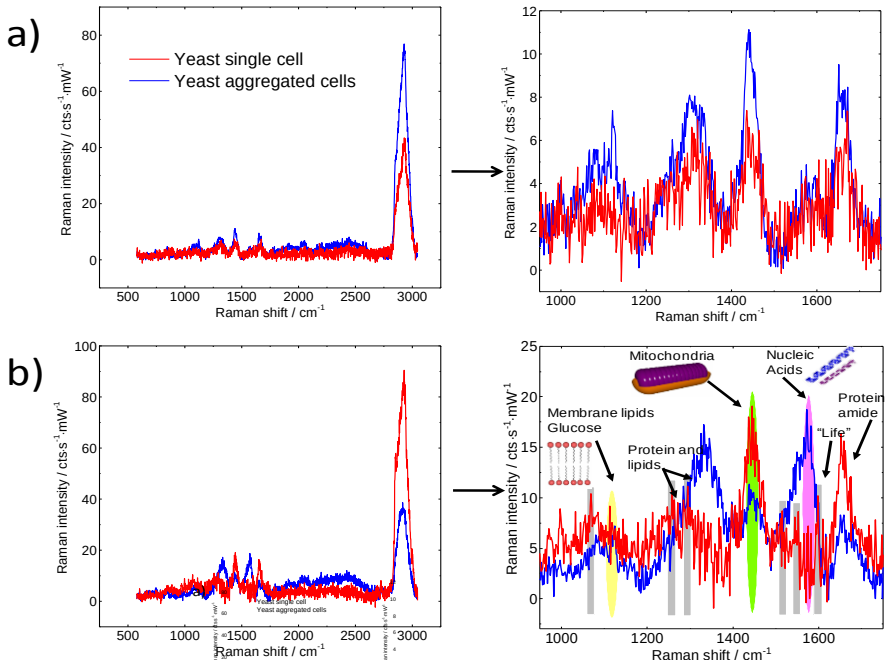

Figure 17. *Raman spectra of yeast cells immobilized on a) bare glass and b) GO-modified glass with part of spectra 'zoomed in' in the range from 950 cm^{-1} to 1750 cm^{-1}. Peaks that are visible only in the spectrum of a single yeast cell modified surface are marked by grey color. The baseline is corrected, and the Raman signal of GO-modified glass was subtracted.*

From these results, we conclude that by analyzing single cells immobilized on GO-modified substrates in comparison to the analysis of large cell aggregates it is possible to gather additional information, which otherwise would be not noticed.

3.4.Self-organized Au nanostructures with bidirectional plasmon resonance for SERS

3.4.1. Morphological characterization of ripple pattern with gold nanostructures

Figure 18a illustrates the two step fabrication routine of SERS substrates with bidirectional plasmon resonance. For the template ion-beam induced ripple patterned silicon substrate was used with the periodicity of (49.9 ± 2.5) nm. Depending on the Au thickness different morphology is observed (Figure 18b,c,d,e). Starting with 30 nm thickness, clear nanoparticle self-organization along the ripple pattern is visible. After increasing the thickness particle elongation is observed which starts forming wire-like nanostructures. By

further increasing Au thickness particles form more intricate nanostructures without forming continuous Au layer. Particles that form on the ripple pattern are rough with less defined shapes [135, 136]. Additional post thermal annealing of the deposited Au particles reshaped them into more smooth and spherical shape (Figure 18f,g). This is comparable to the known silver particle chains on ripple pattern [137, 138].

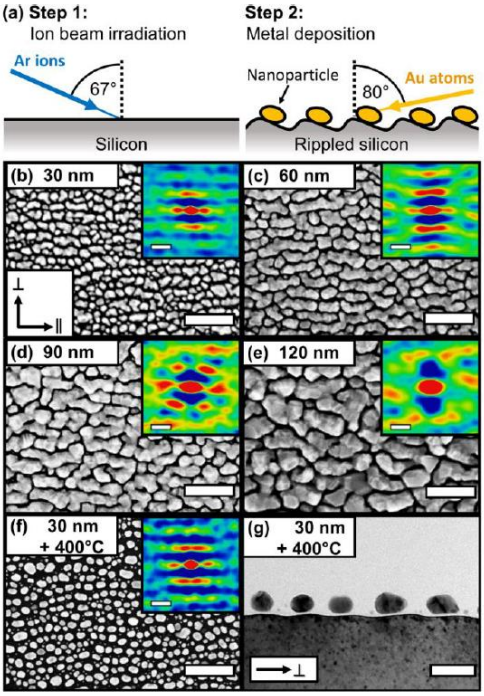

Figure 18. *Morphology of self-organized gold nanostructures on rippled templates. (a) Illustration of two-step fabrication routine. (b-f) top-view SEM images for different gold thicknesses from 30 nm to 120 nm and (f) 30 nm with post-annealing at 400°C. The insets show the corresponding 2D autocorrelations. (g) cross-sectional bright-field TEM image of (f). Scale bars (b-f): 200 nm (insets 50 nm), (g) 50 nm.*

2D autocorrelation and particle analysis allowed to deduce the details on particle geometry. For the 30 nm and 60 nm Au thickness a clear separation of the particles is visible, whereas for larger thicknesses of 90 nm and 120 nm the separation is lost, and particles coalescence takes place.

Table 2 summarizes the Au particle dimensions for samples of 30 nm, 60 nm nominal Au thickness and 30 nm after additional thermal annealing. From 2D autocorrelation the average center-to-center particle distances for the parallel (∥) and perpendicular (⊥) directions with respect to the pattern axis was derived. The nanoparticles follow the periodicity along the ripple pattern with the maximum particle diameter orientated along (∥ direction) and the

minimum diameter across (⊥ direction) the ripples. However, no isolated structures were formed for 90 nm and 120 nm Au deposition thicknesses.

Table 2. *Summarized dimensions of self-organized Au nanoparticles by annealing.*

Sample	min. diameter[a] (nm)	max. diameter[a] (nm)	particle height (nm)	∥ center-to-center (nm)	⊥ center-to-center (nm)
30 nm	24.4±0.3	36.5±1.4	18.1±2.9	30.3±9.4	46.6±8.7
30 nm, annealed	23.1±0.2	29.8±0.4	17.6±3.5	40.2±12.8	46.9±8.4
60 nm	40.0± 0.6	53.1±7.4[b]	-	49.1 ± 8.3	49.1±8.3
	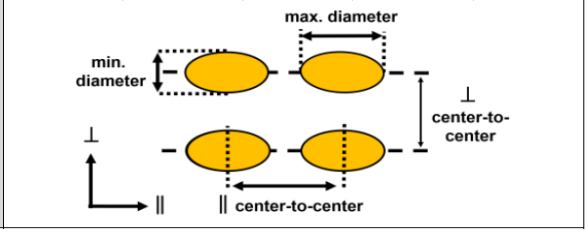				

[a]excluding the particles with diameter <10 nm; [b]excluding the particles grown together over grooves

3.4.2. Optical properties of the nanostructures

In Figure 19 imaginary part of the effective pseudo dielectric function $\langle \varepsilon_2 \rangle$ is plotted which was measured by spectroscopic ellipsometry (SE) and is associated with the absorption position of Au and indicates the position of LSPR. In the range between 400 and 500 nm is the interband transition of Au and starting from 600 nm is the plasmon resonance which depending on the gold layer thickness shifts towards the mid-infrared range. The LSPR can be excited at different spectral positions for polarizations across ($E_\perp$) and along ($E_\parallel$) the ripple axis. For $E_\perp$ polarization the LSPRs are observed in the spectra region from ~600 nm red-shifting with increased Au thickness. For $E_\parallel$ the LSPR starts at ~800 nm and red-shifts and broadens with increased Au layer thickness. This indicates that LSPR across ($E_\perp$) and along ($E_\parallel$) the templates can be selectively excited due to the anisotropic particle shape and coupling in the same directions. Raman spectroscopy using 632.8 nm laser excitation was performed on the substrates having CoPc as a Raman analyte (Figure 19b). By changing polarization Raman signal changes. A_{1g} vibrational Raman mode of CoPc which is at 687 cm^{-1} was analyzed [139]. The enhancement factor (EF) of CoPc was calculated by the intensity ratio of the plasmonic structures with

respect to the Raman signal of the molecule on flat silicon (100) surface which was used as a reference and was from ~150 up to ~1200.

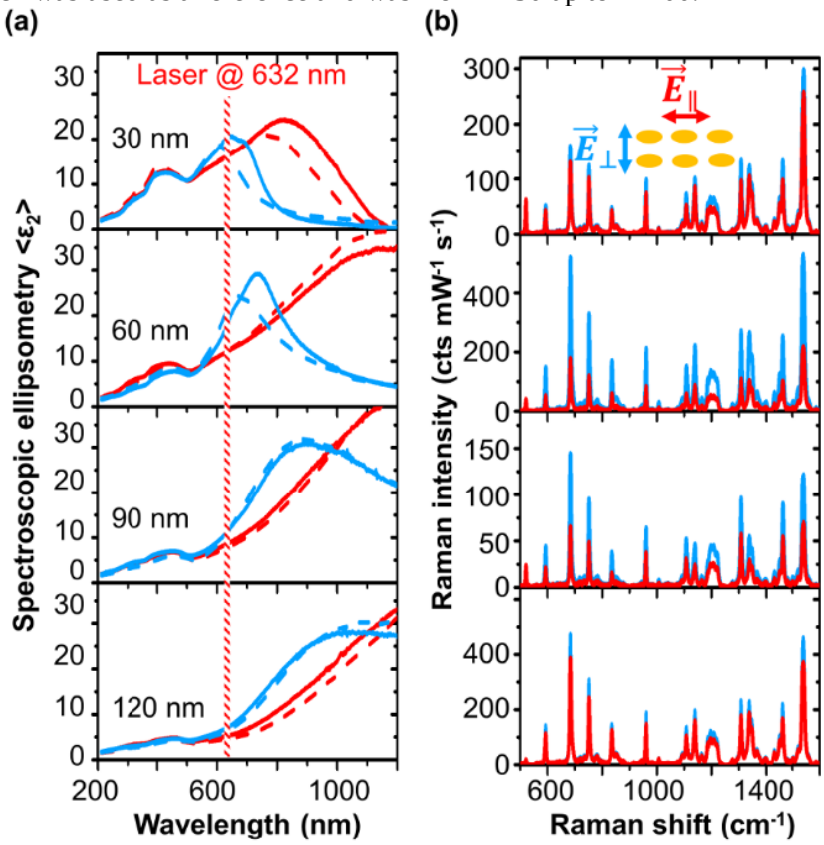

Figure 19. *Development of bidirectional LSPR through the gold deposition process. (a) Spectroscopic ellipsometry (SE) of the imaginary part of the effective dielectric function ⟨ε2⟩ for polarization parallel ($\vec{E}_{\parallel}$, red) and perpendicular ($\vec{E}_{\perp}$, blue) to the nanoparticle chains. Solid and dashed lines for spectra with and without deposited CoPc molecules as Raman probe. The Raman excitation laser line of 632.8 nm is indicated. (b) Raman spectra at the same thicknesses corresponding to SE spectra in each column. Raman signal for different laser polarization $\vec{E}_{\parallel}$ (red) and $\vec{E}_{\perp}$ (blue) are shown.*

From the Table 3 it is observed that the highest enhancement is obtained for $E_{\perp}$ which means that the signal is dominated by the area between the gold chains. For the gold thickness of 60 nm and 90 nm clear anisotropic Raman signal is visible, whereas for 30 nm and 120 nm anisotropy is less pronounced. The results agree with the ones deduced from the SE measurements same as SERS anisotropy is in agreement with the square of ratio of the pseudo-dielectric function at this spectra position. However, the

amplitude values of the imaginary part of the pseudo dielectric function does not represent the plasmonic excitation strength. This is because local plasmonic field enhancement also depends on the local geometry of the particles. For example, strong off-plasmon resonance SERS effect was observed on the 120 nm Au nanostructures which could be due to the strong electromagnetic field enhancement inside the narrow voids (Figure 18).

Table 3. *Summarized Raman enhancement factor EF and pseudo dielectric functions* $\langle \varepsilon_2 \rangle$ *for* $\vec{E}_\perp$ *and* $\vec{E}_\parallel$ *polarizations at excitation wavelength at 632.8 nm.*

Sample	$EF_\parallel$	$EF_\perp$	$\langle \varepsilon_2 \rangle_\parallel$	$\langle \varepsilon_2 \rangle_\perp$	$EF_\perp/EF_\parallel$	$\langle \varepsilon_2 \rangle_\perp^2 / \langle \varepsilon_2 \rangle_\parallel^2$
30 nm	289	313	16.2	20.2	1.1	1.1
60 nm	385	1135	12.1	17.8	2.9	3.0
90 nm	144	314	8.5	11.1	2.2	2.0
120 nm	837	1032	5.2	7.0	1.2	1.8

Since the most pronounced geometry and bidirectional LSPR was for 30 nm Au substrates, these substrates were additionally annealed. After annealing the substrates nanoparticles became more spherical and defined and the center-to-center distance was reduced as well as particle diameter ‖ direction (Table 2). The LSPR shift and effect on SERS by post deposition annealing was observed in Figure 20 by three different excitation laser lines: 532 nm, 638 nm and 785 nm.

With 532 nm no clear anisotropic effect is visible for both annealed and non-annealed samples. This is due to the off-LSPR excitation and thus Raman excitation is low. With 638 nm excitation clear anisotropic SERS effect on the annealed sample and high enhancement for the $E_\parallel$ polarization is visible. For the non-annealed, high SERS response is obtained for $E_\perp$ polarization. However, for the 785 nm this is reversed.

This is a good example of the sample that supports LSPR under two different laser lines which can be selected by the polarization. SERS results are in good agreement with the SE results. In Figure 20b the difference of $\langle \varepsilon_2 \rangle$ is shown where values below zero represents increased LSPR for $E_\perp$ and above zero for $E_\parallel$. Non-annealed sample shows highest LSPR excitation for $E_\parallel$ with peak at around 650 nm whereas annealed sample has 2 LSPRs at 638 nm and 785 nm wavelength, depending on the excitation polarization.

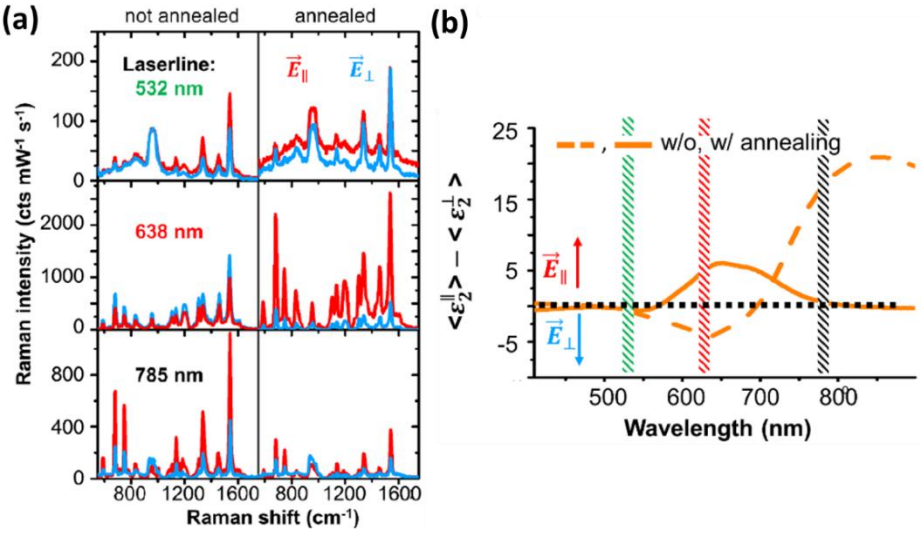

Figure 20. *Polarization dependent VIS-NIR Raman responses for 30 nm gold thickness with and without annealing. (a) Raman spectra of 1 nm CoPc probed by three different laser lines (top: 532 nm, middle: 638 nm, and bottom: 785 nm) for parallel ($\vec{E}_{\parallel}$, red) and perpendicular ($\vec{E}_{\perp}$, blue) polarizations. (b) Difference of the imaginary parts of the pseudo-dielectric function for parallel and perpendicular excitation measured for 30 nm gold thickness without (solid) and with annealing (dashed). Difference below or above zero means that Raman is enhanced for $\vec{E}_{\perp}$ or $\vec{E}_{\parallel}$ polarization.*

3.4.3. Finite element method calculations

In Figure 21 the spatial distribution of hotspots calculated using finite element method for annealed and non-annealed samples are presented. For the annealed sample under 638 nm excitation plasmonic hotspots can be observed along the particle chains even if the particles are not fully aligned. For the $E_{\perp}$ a lower field enhancement is visible across the ripple pattern. In the cross-section view of the simulation (Figure 21c) it's observed that a big portion of the electric field is trapped under the particle in the native oxide layer [140]. Moreover, the distance between the particles is higher which adds up to the plasmon coupling between the nanoparticles being weak for $E_{\perp}$.

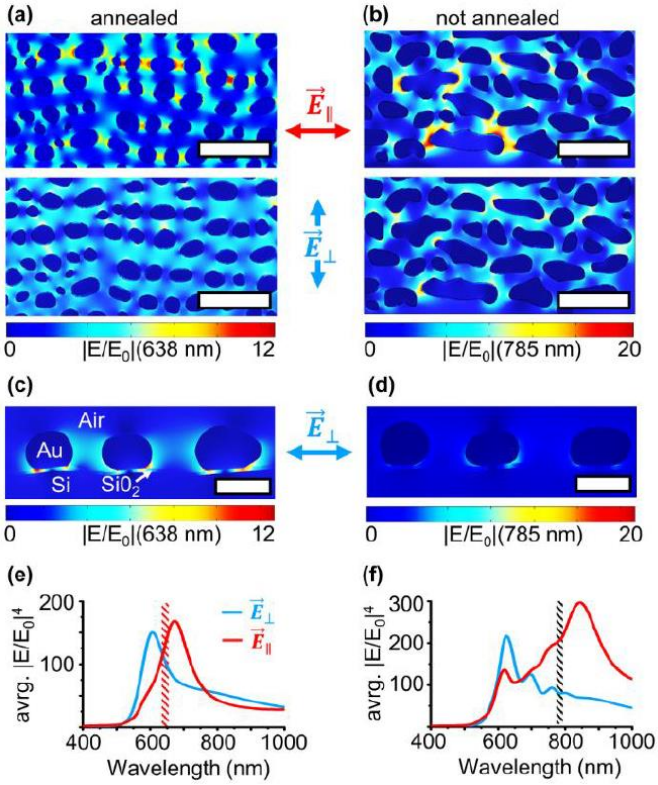

Figure 21. *FEM calculation results of the near-field enhancement of electric* $|E|/|E_0|$ *based on SEM images. The systems modeled correspond to (a) annealed and (b) non-annealed gold samples for two different directions of the incident electric field (top)* $\vec{E}_{\parallel}$ *and (bottom)* $\vec{E}_{\perp}$*. Scale bars: 100 nm. The particle cross-section visualization of the annealed (c) and not annealed (d) sample is shown below (scale 30 nm). Simulated spectra of average SERS enhancement (*$\propto$ *avrg.* $|E|^4/|E_0|^4$*) for annealed and not annealed particle geometries for* $\vec{E}_{\perp}$ *and* $\vec{E}_{\parallel}$ *polarizations.*

Situation for the non-annealed scenario becomes more complicated due to the oval particle shape. Moreover, broad particle size, aspect ratio and shape distribution contribute to the LSPR being excited in the wide spectra range. The chain structure made out of interconnected oval-shape particles can also attribute to the coupling of hotspots in the $E_{\parallel}$ direction at 785 nm [141]. However, from SE and Raman results the $E_{\perp}$ 785 nm excitation does not match the LSPR and no hotspots are visible only weak plasmon coupling along the particle rows due to inhomogeneity of the particles. In Figure 21e,f spectra of average SERS enhancement $|E|^4/|E_0|^4$ for both particle shapes are presented. These simulations agree with the measured $\langle\varepsilon_2\rangle$ and anisotropic Raman signal ratios for $E_{\perp}$ and $E_{\parallel}$. Furthermore, the calculated enhancements

are 1-3 times weaker than obtained from Raman measurements. This is because signal amplification is coming from few, but very strong hotspots, preferably from between rough particles, and therefore the samples cannot be fully represented by the FEM calculations.

General conclusions

1. Polypyrrole microspheres were successfully synthesized through green method using 2 different strains of *Streptomyces* spp. bacteria. Microspheres obtained using *Streptomyces* spp. MIUG 12p strain were ~25 μm diameter, denser and lower in concentration compared to the ones obtained using MIUG 4.88 which were ~10 μm in diameter, higher in concentration and were completely hollow.
2. Several nanomaterials were used for GC electrode modification before and after electrochemical modification with 3NA: GO, G, Fe_3O_4, AuChts and MWCNT towards Cu(II) ions detection. Electrode, which was modified with MWCNT and then modified with 3NA which was then reduced, showed 16 times increased signal towards Cu(II) ions compared to the bare GC.
3. Since GC/MWCNT/3NA(red) showed the best response towards Cu(II) detection selectivity, repeatability, reproducibility and stability was investigated. Selectivity investigation showed that this electrode is selective towards Cu(II) ions. R.V.S. of repeatability and reproducibility tests were 6.4% and 1.4% respectively, and after storing electrode for 5 days it's signal reduced down to 50% and became stable. LOD for the GC/MWCNT/3NA(red) was 0.5×10^{-9} M Cu(II) ions concentration.
4. The method for obtaining single yeast cells using substrates modified with GO nanosheets proved that cell immobilization on the GO-modified surfaces is possible due to presence of proteins on the cell surface, which bonds with the functional groups of GO.
5. Raman signal of yeast cells on GO-modified glass substrates was enhanced by 100% compared with the signal of yeast cells obtained on the glass. In Raman spectra obtained from single cell peaks at 1260 cm^{-1}, 1294 cm^{-1}, 1548 cm^{-1} and 1601 cm^{-1} are observed, they are attributed to proteins, lipids, nucleic acids and even "cell life" respectively, but are absent in Raman spectra obtained from the aggregated cells.
6. SERS substrates that were produced by two-step fabrication method showed EF up to ~1200 times. Moreover, by changing the gold thickness and position of the substrate it's possible to tune in LSPR with different wavelengths.
7. FEM calculations showed that for 30 nm Au thickness annealed sample under 638 nm plasmonic hotspots were observed along the particle chains. For non-annealed 30 nm Au thickness plasmon hotspots can be observed in the $E_{\parallel}$ direction under 785 nm excitation, but the hotspots are localized on single nanoparticles mostly with an elongated shape.

Summary

These days development of various sensors became one of the most important study topics. The focus on developing sensors is on the sensibility, selectivity and stability. In this dissertation polypyrrole environmentally friendly synthesis method is presented using two different strains of Streptomyces spp. bacteria: MIUG 12p and MIUG 4.88. SEM and optical microscope images showed that PPy hollow microspheres were obtained during the synthesis with the size varying from 10 to 25 μm depending on the strain. FTIR and XPS analysis of bacterial PPy was consistent with that of electrochemically synthesized PPy and pyrrole monomer with presence of derivatives which is equal in all the compounds. These microspheres could be adapted for the drug delivery and something else.

Electrochemical sensor for Cu(II) ions was developed using glassy carbon electrode modified with MWCNT and then reduced 3-nitroaniline. Such electrode showed selectivity towards Cu(II) ions in the presence of other metals. Moreover, R.S.V of reproducibility and repeatability tests were 6.4% and 1.4% respectively. After storing the electrode for 5 days signal reduced by 50% and stayed stable for up to 14 days. Limit of detection tested towards Cu(II) ions was 0.5×10^{-9} M. Such electrode performed better than glassy carbon electrode modified with reduced 4-nitroaniline produced by the same group. This is due to the MWCNT which increased working electrodes surface area.

Raman spectroscopy is one of the vastly used analytical devices, which are easy to use, non-destructive and reliable. However, Raman signal is relatively low and requires additional substrate modification in order to enhance it. Moreover, when analyzing cell colony, the signal is averaged, and part of information is lost. For that graphene oxide modified substrates were used to enhance the signal and obtain single yeast cells which were further analyzed using Raman spectroscopy. It was discovered that GO enhances single yeast cell signal by 100 times and shows additional peaks in spectra, which corresponds to important compounds and even “cell life” that otherwise are or ignored when analyzing the cell colony.

As it was mentioned before Raman spectroscopy signal is relatively low and here surface enhanced Raman spectroscopy can be applied, where metal plasmon nanocomposites are used to enhance the signal. However, such substrates have plasmon resonance only in certain range, depending on the metal, shape or size of the nanocomposites. In this thesis a two-step method was suggested for obtaining bidirectional plasmon resonance by inducing ripple pattern on the silicon substrate and then depositing gold nanoparticle.

Depending on the substrate orientation it's possible to obtain plasmon resonance in different spectra ranges.

References

[1] Y. Alvarez-Gallego, X. Dominguez-Benetton, D. Pant, L. Diels, K. Vanbroekhoven, I. Genné, P. Vermeiren, Development of gas diffusion electrodes for cogeneration of chemicals and electricity, Electrochimica Acta, 82 (2012) 415-426.
[2] C.-L. Yu, N.-C. Lo, H. Cheng, T. Tsuda, T. Sakamoto, Y.-H. Chen, S. Kuwabata, P.-Y. Chen, An ionic liquid-Fe_3O_4 nanoparticles-graphite composite electrode used for nonenzymatic electrochemical determination of hydrogen peroxide, Journal of Electroanalytical Chemistry, 729 (2014) 109-115.
[3] X. Zhang, D. Pant, F. Zhang, J. Liu, W. He, B.E. Logan, Long-term performance of chemically and physically modified activated carbons in air cathodes of microbial fuel cells, ChemElectroChem, 1 (2014) 1859-1866.
[4] L.M. Niu, H.Q. Luo, N.B. Li, L. Song, Electrochemical detection of copper (II) at a gold electrode modified with a self-assembled monolayer of penicillamine, Journal of Analytical Chemistry, 62 (2007) 470-474.
[5] M. Lin, M. Cho, W.-S. Choe, Y. Son, Y. Lee, Electrochemical detection of copper ion using a modified copolythiophene electrode, Electrochimica Acta, 54 (2009) 7012-7017.
[6] E. Bilici, Z. Yazicigil, M. Tok, Y. Oztekin, Electrochemical determination of copper (II) using modified glassy carbon electrodes, Desalination and Water Treatment, 50 (2012) 198-205.
[7] Y. Oztekin, M. Tok, H. Nalvuran, S. Kiyak, T. Gover, Z. Yazicigil, A. Ramanaviciene, A. Ramanavicius, Electrochemical modification of glassy carbon electrode by poly-4-nitroaniline and its application for determination of copper (II), Electrochimica Acta, 56 (2010) 387-395.
[8] G. Aragay, J. Pons, A. Merkoçi, Recent trends in macro-, micro-, and nanomaterial-based tools and strategies for heavy-metal detection, Chemical reviews, 111 (2011) 3433-3458.
[9] T. Alizadeh, M.R. Ganjali, M. Zare, Application of an Hg 2+ selective imprinted polymer as a new modifying agent for the preparation of a novel highly selective and sensitive electrochemical sensor for the determination of ultratrace mercury ions, Analytica chimica acta, 689 (2011) 52-59.
[10] L. Lin, J. Chen, H. Yao, Y. Chen, Y. Zheng, X. Lin, Simultaneous determination of dopamine, ascorbic acid and uric acid at poly (Evans Blue) modified glassy carbon electrode, Bioelectrochemistry, 73 (2008) 11-17.
[11] X. Dai, R.G. Compton, Detection of As (III) via oxidation to As (V) using platinum nanoparticle modified glassy carbon electrodes: arsenic detection without interference from copper, Analyst, 131 (2006) 516-521.
[12] C. Raman, K. Krishnan, A new type of secondary radiation (Nature, 1928, 121, 501-502), CURRENT SCIENCE-BANGALORE-, 74 (1998) 381-381.

[13] P.Y. Yu, M. Cardona, Fundamentals of semiconductors: physics and materials properties, Springer2010.
[14] A. Downes, A. Elfick, Raman spectroscopy and related techniques in biomedicine, Sensors, 10 (2010) 1871-1889.
[15] K.A. Antonio, Z.D. Schultz, Advances in biomedical raman microscopy, Analytical chemistry, 86 (2013) 30-46.
[16] A.C. Ferrari, D.M. Basko, Raman spectroscopy as a versatile tool for studying the properties of graphene, Nature nanotechnology, 8 (2013) 235-246.
[17] A. Raza, B. Saha, Application of Raman spectroscopy in forensic investigation of questioned documents involving stamp inks, Science & Justice, 53 (2013) 332-338.
[18] F. Casadio, C. Daher, L. Bellot-Gurlet, Raman spectroscopy of cultural heritage materials: overview of applications and new frontiers in instrumentation, sampling modalities, and data processing, Topics in Current Chemistry, 374 (2016) 62.
[19] M. Fan, G.F.S. Andrade, A.G. Brolo, A review on the fabrication of substrates for surface enhanced Raman spectroscopy and their applications in analytical chemistry, Analytica Chimica Acta, 693 (2011) 7-25.
[20] C.S. Kumar, Raman spectroscopy for nanomaterials characterization, Springer Science & Business Media2012.
[21] D. Gangopadhyay, P. Sharma, S.K. Singh, P. Singh, V. Deckert, J. Popp, R.K. Singh, Surface enhanced Raman scattering based reaction monitoring of in vitro decyclization of creatinine→ creatine, RSC Advances, 6 (2016) 58943-58949.
[22] L. Mikoliunaite, R.D. Rodriguez, E. Sheremet, V. Kolchuzhin, J. Mehner, A. Ramanavicius, D.R. Zahn, The substrate matters in the Raman spectroscopy analysis of cells, Scientific reports, 5 (2015).
[23] K. Hering, D. Cialla, K. Ackermann, T. Dörfer, R. Möller, H. Schneidewind, R. Mattheis, W. Fritzsche, P. Rösch, J. Popp, SERS: a versatile tool in chemical and biochemical diagnostics, Analytical and bioanalytical chemistry, 390 (2008) 113-124.
[24] E. Le Ru, P. Etchegoin, Principles of Surface-Enhanced Raman Spectroscopy: and related plasmonic effects, Elsevier2008.
[25] M. Fleischmann, P.J. Hendra, A.J. McQuillan, Raman spectra of pyridine adsorbed at a silver electrode, Chemical Physics Letters, 26 (1974) 163-166.
[26] K.L. Kelly, E. Coronado, L.L. Zhao, G.C. Schatz, The optical properties of metal nanoparticles: the influence of size, shape, and dielectric environment, ACS Publications, 2003.
[27] E. Le Ru, E. Blackie, M. Meyer, P.G. Etchegoin, Surface enhanced Raman scattering enhancement factors: a comprehensive study, The Journal of Physical Chemistry C, 111 (2007) 13794-13803.
[28] P. Chandrasekhar, B.J. Zay, T. McQueeney, G.C. Birur, V. Sitaram, R. Menon, M. Coviello, R.L. Elsenbaumer, Physical, chemical, theoretical

aspects of conducting polymer electrochromics in the visible, IR and microwave regions, Synthetic Metals, 155 (2005) 623-627.
[29] T.A. Skotheim, R.L. Elsenbaumer, J.R. Reynolds, Handbook of conducting polymers, 2nd ed., M. Dekker, New York, 1998.
[30] H.S. Nalwa, Handbook of organic conductive molecules and polymers, Wiley, Chichester ; New York, 1997.
[31] Y. Wan, H. Wu, D. Wen, Porous-Conductive Chitosan Scaffolds for Tissue Engineering, 1, Macromolecular bioscience, 4 (2004) 882-890.
[32] S. Sadki, P. Schottland, N. Brodie, G. Sabouraud, The mechanisms of pyrrole electropolymerization, Chemical Society Reviews, 29 (2000) 283-293.
[33] A. Chauhan, S. Zubair, S. Tufail, A. Sherwani, M. Sajid, S.C. Raman, A. Azam, M. Owais, Fungus-mediated biological synthesis of gold nanoparticles: potential in detection of liver cancer, International journal of nanomedicine, 6 (2011) 2305.
[34] R. Sindhu, A. Pandey, P. Binod, Microbial Diversity of Nanoparticle Biosynthesis, Bio-Nanoparticles, John Wiley & Sons, Inc2015, pp. 187-203.
[35] H. Korbekandi, S. Iravani, S. Abbasi, Production of nanoparticles using organisms, Critical Reviews in Biotechnology, 29 (2009) 279-306.
[36] D. Byrom, Polymer synthesis by microorganisms: technology and economics, Trends in Biotechnology, 5 (1987) 246-250.
[37] R. Bouldin, S. Ravichandran, A. Kokil, R. Garhwal, S. Nagarajan, J. Kumar, F.F. Bruno, L.A. Samuelson, R. Nagarajan, Synthesis of polypyrrole with fewer structural defects using enzyme catalysis, Synthetic Metals, 161 (2011) 1611-1617.
[38] K. Leonavicius, A. Ramanaviciene, A. Ramanavicius, Polymerization model for hydrogen peroxide initiated synthesis of polypyrrole nanoparticles, Langmuir, 27 (2011) 10970-10976.
[39] H.V.R. Dias, M. Fianchini, R.M.G. Rajapakse, Greener method for high-quality polypyrrole, Polymer, 47 (2006) 7349-7354.
[40] F.F. Bruno, S.A. Fossey, S. Nagarajan, R. Nagarajan, J. Kumar, L.A. Samuelson, Biomimetic Synthesis of Water-Soluble Conducting Copolymers/Homopolymers of Pyrrole and 3,4-Ethylenedioxythiophene, Biomacromolecules, 7 (2005) 586-589.
[41] J. Tabačiarová, M. Mičušík, P. Fedorko, M. Omastová, Study of polypyrrole aging by XPS, FTIR and conductivity measurements, Polymer Degradation and Stability, 120 (2015) 392-401.
[42] A.A. Jbarah, R. Holze, A comparative spectroelectrochemical study of the redox electrochemistry of nitroanilines, Journal of Solid State Electrochemistry, 10 (2006) 360-372.
[43] M. Dadsetani, A. Omidi, Linear and nonlinear optical properties of 3-nitroaniline (m-NA) and 4-nitroaniline (p-NA) crystals: A DFT/TDDFT study, Journal of Physics and Chemistry of Solids, 85 (2015) 117-131.
[44] T. Kanagasekaran, M. Gunasekaran, P. Srinivasan, D. Jayaraman, R. Gopalakrishnan, P. Ramasamy, Studies on growth, induction period,

interfacial energy and metastable zonewidth of m-nitroaniline, Crystal Research and Technology, 40 (2005) 1128-1133.
[45] M. Dadsetani, A.R. Omidi, Linear and nonlinear optical properties of 3-nitroaniline (m-NA) and 4-nitroaniline (p-NA) crystals: A DFT/TDDFT study, Journal of Physics and Chemistry of Solids, 85 (2015) 117-131.
[46] H. Nobutoki, H. Koezuka, Theoretical study of hyperpolarizabilities in crystalline m-nitroaniline, The Journal of Physical Chemistry A, 101 (1997) 3762-3768.
[47] V. Krishnakumar, R. Nagalakshmi, Studies on the first-order hyperpolarizability and terahertz generation in 3-nitroaniline, Physica B: Condensed Matter, 403 (2008) 1863-1869.
[48] L. Avanci, L. Cardoso, S. Girdwood, D. Pugh, J. Sherwood, K. Roberts, Piezoelectric coefficients of mNA organic nonlinear optical material using synchrotron X-ray multiple diffraction, Physical review letters, 81 (1998) 5426.
[49] L. Avanci, R. Braga, L. Cardoso, D. Galvao, J. Sherwood, Hysteresislike behavior in meta-nitroaniline crystals, Physical Review Letters, 83 (1999) 5146.
[50] D.R. Dreyer, S. Park, C.W. Bielawski, R.S. Ruoff, The chemistry of graphene oxide, Chemical Society Reviews, 39 (2010) 228-240.
[51] C. Chung, Y.-K. Kim, D. Shin, S.-R. Ryoo, B.H. Hong, D.-H. Min, Biomedical applications of graphene and graphene oxide, Accounts of chemical research, 46 (2013) 2211-2224.
[52] Y. Wang, Z. Li, J. Wang, J. Li, Y. Lin, Graphene and graphene oxide: biofunctionalization and applications in biotechnology, Trends in biotechnology, 29 (2011) 205-212.
[53] S.H. Yang, T. Lee, E. Seo, E.H. Ko, I.S. Choi, B.S. Kim, Interfacing living yeast cells with graphene oxide nanosheaths, Macromolecular bioscience, 12 (2012) 61-66.
[54] J.T. Robinson, F.K. Perkins, E.S. Snow, Z. Wei, P.E. Sheehan, Reduced graphene oxide molecular sensors, Nano letters, 8 (2008) 3137-3140.
[55] C.K. Chua, M. Pumera, Chemical reduction of graphene oxide: a synthetic chemistry viewpoint, Chemical Society Reviews, 43 (2014) 291-312.
[56] J. Kauppila, P. Kunnas, P. Damlin, A. Viinikanoja, C. Kvarnström, Electrochemical reduction of graphene oxide films in aqueous and organic solutions, Electrochimica Acta, 89 (2013) 84-89.
[57] X. Gao, J. Jang, S. Nagase, Hydrazine and thermal reduction of graphene oxide: reaction mechanisms, product structures, and reaction design, The Journal of Physical Chemistry C, 114 (2009) 832-842.
[58] P. Khanra, T. Kuila, N.H. Kim, S.H. Bae, D.-s. Yu, J.H. Lee, Simultaneous bio-functionalization and reduction of graphene oxide by baker's yeast, Chemical Engineering Journal, 183 (2012) 526-533.

[59] A. Al-Hamry, H. Kang, E. Sowade, V. Dzhagan, R. Rodriguez, C. Müller, D. Zahn, R. Baumann, O. Kanoun, Tuning the reduction and conductivity of solution-processed graphene oxide by intense pulsed light, Carbon, 102 (2016) 236-244.
[60] T. Yamabe, K. Fukui, K. Tanaka, The science and technology of carbon nanotubes, Elsevier1999.
[61] C. Kaya, I. Singh, A.R. Boccaccini, Multi-walled carbon nanotube-reinforced hydroxyapatite layers on Ti6Al4V medical implants by Electrophoretic Deposition (EPD), Advanced Engineering Materials, 10 (2008) 131-138.
[62] A.V. Eletskii, Sorption properties of carbon nanostructures, Physics-Uspekhi, 47 (2004) 1119-1154.
[63] A. Merkoçi, Carbon nanotubes in analytical sciences, Microchimica Acta, 152 (2006) 157-174.
[64] M. Boujtita, 1 - Chemical and biological sensing with carbon nanotubes (CNTs) A2 - Honeychurch, Kevin C, Nanosensors for Chemical and Biological Applications, Woodhead Publishing2014, pp. 3-27.
[65] I.V. Zaporotskova, N.P. Boroznina, Y.N. Parkhomenko, L.V. Kozhitov, Carbon nanotubes: Sensor properties. A review, Modern Electronic Materials, 2 (2016) 95-105.
[66] A. Ramanavicius, I. Morkvenaite-Vilkonciene, A. Kisieliute, J. Petroniene, A. Ramanaviciene, Scanning electrochemical microscopy based evaluation of influence of pH on bioelectrochemical activity of yeast cells − Saccharomyces cerevisiae, Colloids and Surfaces B: Biointerfaces, 149 (2017) 1-6.
[67] A. Ramanavicius, E. Andriukonis, A. Stirke, L. Mikoliunaite, Z. Balevicius, A. Ramanaviciene, Synthesis of polypyrrole within the cell wall of yeast by redox-cycling of [Fe(CN)6]3−/[Fe(CN)6]4−, Enzyme and Microbial Technology, 83 (2016) 40-47.
[68] I. Morkvenaite-Vilkonciene, A. Ramanaviciene, A. Ramanavicius, 9,10-Phenanthrenequinone as a redox mediator for the imaging of yeast cells by scanning electrochemical microscopy, Sensors and Actuators B: Chemical, 228 (2016) 200-206.
[69] A. Stirke, A. Zimkus, S. Balevicius, V. Stankevic, A. Ramanaviciene, A. Ramanavicius, N. Zurauskiene, Permeabilization of yeast Saccharomyces cerevisiae cell walls using nanosecond high power electrical pulses, Applied Physics Letters, 105 (2014) 253701.
[70] A. Stirke, A. Zimkus, A. Ramanaviciene, S. Balevicius, N. Zurauskiene, G. Saulis, L. Chaustova, V. Stankevic, A. Ramanavicius, Electric field-induced effects on yeast cell wall permeabilization, Bioelectromagnetics, 35 (2014) 136-144.
[71] K. Baronian, The use of yeast and moulds as sensing elements in biosensors, Biosensors and bioelectronics, 19 (2004) 953-962.

[72] K.J. Verstrepen, F.M. Klis, Flocculation, adhesion and biofilm formation in yeasts, Molecular microbiology, 60 (2006) 5-15.
[73] C. Nune, W. Xu, R. Misra, The impact of grafted modification of silicone surfaces with quantum-sized materials on protein adsorption and bacterial adhesion, Journal of Biomedical Materials Research Part A, 100 (2012) 3197-3204.
[74] Y. Shen, M.R. Ahmad, M. Nakajima, S. Kojima, M. Homma, T. Fukuda, Evaluation of the single yeast cell's adhesion to ITO substrates with various surface energies via ESEM nanorobotic manipulation system, NanoBioscience, IEEE Transactions on, 10 (2011) 217-224.
[75] M. Stobiecka, B. Dworakowska, S. Jakiela, A. Lukasiak, A. Chalupa, K. Zembrzycki, Sensing of survivin mRNA in malignant astrocytes using graphene oxide nanocarrier-supported oligonucleotide molecular beacons, Sensors and Actuators B: Chemical, 235 (2016) 136-145.
[76] L. Mikoliunaite, A. Makaraviciute, A. Suchodolskis, A. Ramanaviciene, Y. Oztekin, A. Stirke, G. Jurkaite, M. Ukanis, G. Carac, P. Cojocaru, Atomic Force Microscopy Study of Living Baker's Yeast Cells, Advanced Science Letters, 4 (2011) 368-376.
[77] A. Amantonico, J.Y. Oh, J. Sobek, M. Heinemann, R. Zenobi, Mass spectrometric method for analyzing metabolites in yeast with single cell sensitivity, Angewandte Chemie International Edition, 47 (2008) 5382-5385.
[78] S. Lindström, H. Andersson-Svahn, Miniaturization of biological assays—Overview on microwell devices for single-cell analyses, Biochimica et Biophysica Acta (BBA)-General Subjects, 1810 (2011) 308-316.
[79] K.R. Love, V. Panagiotou, B. Jiang, T.A. Stadheim, J.C. Love, Integrated single-cell analysis shows Pichia pastoris secretes protein stochastically, Biotechnology and bioengineering, 106 (2010) 319-325.
[80] B. Sankaran, M. Racic, A. Tona, M.V. Rao, M. Gaitan, S.P. Forry, Dielectrophoretic capture of mammalian cells using transparent indium tin oxide electrodes in microfluidic systems, Electrophoresis, 29 (2008) 5047-5054.
[81] Q. Cheng, K. Komvopoulos, S. Li, Surface chemical patterning for long-term single-cell culture, Journal of Biomedical Materials Research Part A, 96 (2011) 507-512.
[82] D. Falconnet, G. Csucs, H.M. Grandin, M. Textor, Surface engineering approaches to micropattern surfaces for cell-based assays, Biomaterials, 27 (2006) 3044-3063.
[83] F.S. Fritzsch, C. Dusny, O. Frick, A. Schmid, Single-cell analysis in biotechnology, systems biology, and biocatalysis, Annual review of chemical and biomolecular engineering, 3 (2012) 129-155.
[84] A. Suchodolskis, V. Feiza, A. Stirke, A. Timonina, A. Ramanaviciene, A. Ramanavicius, Elastic properties of chemically modified baker's yeast cells studied by AFM, Surface and Interface Analysis, 43 (2011) 1636-1640.

[85] A. Suchodolskis, A. Stirke, A. Timonina, A. Ramanaviciene, A. Ramanavicius, Baker's yeast transformation studies by Atomic Force Microscopy, Advanced Science Letters, 4 (2011) 171-173.
[86] C. Xie, M.A. Dinno, Y.-q. Li, Near-infrared Raman spectroscopy of single optically trapped biological cells, Opt. Lett., 27 (2002) 249-251.
[87] M. Cotarlet, G. Bahrim, T. Negoita, P. Stougaard, Screening of polar streptomycetes able to produce cold-active hydrolytic enzymes using common and chromogenic substrates, Romanian Biotechnological Letters, 13 (2008) 69-80.
[88] D.C. Marcano, D.V. Kosynkin, J.M. Berlin, A. Sinitskii, Z. Sun, A. Slesarev, L.B. Alemany, W. Lu, J.M. Tour, Improved synthesis of graphene oxide, (2010).
[89] Y. Wang, D. Zhang, J. Wu, Electrocatalytic oxidation of kojic acid at a reduced graphene sheet modified glassy carbon electrode, Journal of Electroanalytical Chemistry, 664 (2012) 111-116.
[90] Y. Yong, Y. Bai, Y. Li, L. Lin, Y. Cui, C. Xia, Preparation and application of polymer-grafted magnetic nanoparticles for lipase immobilization, Journal of Magnetism and Magnetic Materials, 320 (2008) 2350-2355.
[91] H. Çiftçi, U. Tamer, A.Ü. Metin, E. Alver, N. Kizir, Electrochemical copper (II) sensor based on chitosan covered gold nanoparticles, Journal of Applied Electrochemistry, 44 (2014) 563-571.
[92] A. Stirke, R.-M. Apetrei, M. Kirsnyte, L. Dedelaite, V. Bondarenka, V. Jasulaitiene, M. Pucetaite, A. Selskis, G. Carac, G. Bahrim, Synthesis of polypyrrole microspheres by Streptomyces spp, Polymer, 84 (2016) 99-106.
[93] Y. Oztekin, Z. Yazicigil, A.O. Solak, Z. Ustundag, A. Okumus, Z. Kilic, A. Ramanaviciene, A. Ramanavicius, Phenanthroline derivatives electrochemically grafted to glassy carbon for Cu (II) ion detection, Sensors and Actuators B: Chemical, 166 (2012) 117-127.
[94] Y. Oztekin, M. Tok, E. Bilici, L. Mikoliunaite, Z. Yazicigil, A. Ramanaviciene, A. Ramanavicius, Copper nanoparticle modified carbon electrode for determination of dopamine, Electrochimica Acta, 76 (2012) 201-207.
[95] L. Dedelaite, S. Kizilkaya, H. Incebay, H. Ciftci, M. Ersoz, Z. Yazicigil, Y. Oztekin, A. Ramanaviciene, A. Ramanavicius, Electrochemical determination of Cu(II) ions using glassy carbon electrode modified by some nanomaterials and 3-nitroaniline, Colloids and Surfaces A: Physicochemical and Engineering Aspects, 483 (2015) 279-284.
[96] N. Cao, Y. Zhang, Study of reduced graphene oxide preparation by Hummers' method and related characterization, Journal of Nanomaterials, 2015 (2015) 2.
[97] L. Dedelaite, R.D. Rodriguez, E. Andriukonis, M. Hietschold, D.R. Zahn, A. Ramanavicius, Surfaces functionalized by graphene oxide nanosheets for

single cell investigations, Sensors and Actuators B: Chemical, 255 (2018) 1735-1743.
[98] A. Keller, S. Facsko, W. Möller, Minimization of topological defects in ion-induced ripple patterns on silicon, New Journal of Physics, 10 (2008) 063004.
[99] B. Schreiber, D. Gkogkou, L. Dedelaite, J. Kerbusch, R. Hubner, E. Sheremet, D.R.T. Zahn, A. Ramanavicius, S. Facsko, R.D. Rodriguez, Large-scale self-organized gold nanostructureswith bidirectional plasmon resonances for SERS, RSC Advances, 8 (2018) 22569-22576.
[100] S.W. Kim, H.G. Cho, C.R. Park, Fabrication of unagglomerated polypyrrole nanospheres with controlled sizes from a surfactant-free emulsion system, Langmuir, 25 (2009) 9030-9036.
[101] Y. Liu, Y. Chu, L. Yang, Adjusting the inner-structure of polypyrrole nanoparticles through microemulsion polymerization, Materials chemistry and physics, 98 (2006) 304-308.
[102] A. Ramanavicius, A. Kausaite, A. Ramanaviciene, J. Acaite, A. Malinauskas, Redox enzyme–glucose oxidase–initiated synthesis of polypyrrole, Synthetic Metals, 156 (2006) 409-413.
[103] P.M. George, D.A. LaVan, J.A. Burdick, C.Y. Chen, E. Liang, R. Langer, Electrically Controlled Drug Delivery from Biotin-Doped Conductive Polypyrrole, Advanced Materials, 18 (2006) 577-581.
[104] P. Novák, B. Rasch, W. Vielstich, Overoxidation of Polypyrrole in Propylene Carbonate An In Situ FTIR Study, Journal of the Electrochemical Society, 138 (1991) 3300-3304.
[105] A. Kros, J.G. Linhardt, H.K. Bowman, D.A. Tirrell, From giant vesicles to filaments and wires: Templates for conducting polymers, Advanced materials, 16 (2004) 723-727.
[106] F.H. Du, B. Li, W. Fu, Y.J. Xiong, K.X. Wang, J.S. Chen, Surface Binding of Polypyrrole on Porous Silicon Hollow Nanospheres for Li-Ion Battery Anodes with High Structure Stability, Advanced materials, 26 (2014) 6145-6150.
[107] R. Panigrahi, S.K. Srivastava, Trapping of microwave radiation in hollow polypyrrole microsphere through enhanced internal reflection: A novel approach, Scientific reports, 5 (2015) 7638.
[108] L. Wang, Z. Lou, T. Fei, T. Zhang, Zinc oxide core–shell hollow microspheres with multi-shelled architecture for gas sensor applications, Journal of Materials Chemistry, 21 (2011) 19331-19336.
[109] X. Lu, D. Chao, J. Chen, W. Zhang, Y. Wei, Preparation and characterization of inorganic/organic hybrid nanocomposites based on Au nanoparticles and polypyrrole, Materials letters, 60 (2006) 2851-2854.
[110] L. Sabbatini, C. Malitesta, E. De Giglio, I. Losito, L. Torsi, P. Zambonin, Electrosynthesised thin polymer films: the role of XPS in the design of application oriented innovative materials, Journal of Electron Spectroscopy and Related Phenomena, 100 (1999) 35-53.

[111] A.L. Harreus, R. Backes, J.O. Eichler, R. Feuerhake, C. Jäkel, U. Mahn, R. Pinkos, R. Vogelsang, 2-Pyrrolidone, Ullmann's Encyclopedia of Industrial Chemistry, Wiley-VCH Verlag GmbH & Co. KGaA2000.
[112] S.D. Gardner, C.S. Singamsetty, G.L. Booth, G.-R. He, C.U. Pittman Jr, Surface characterization of carbon fibers using angle-resolved XPS and ISS, Carbon, 33 (1995) 587-595.
[113] S. Delpeux, F. Beguin, R. Benoit, R. Erre, N. Manolova, I. Rashkov, Fullerene core star-like polymers—1. Preparation from fullerenes and monoazidopolyethers, European polymer journal, 34 (1998) 905-915.
[114] L.N. Bui, N.B. Thompson M Fau - McKeown, A.D. McKeown Nb Fau - Romaschin, P.G. Romaschin Ad Fau - Kalman, P.G. Kalman, Surface modification of the biomedical polymer poly(ethylene terephthalate), (1993) 463-474.
[115] E.T. Kang, K.G. Neoh, Y.K. Ong, K.L. Tan, B.T.G. Tan, X-ray photoelectron spectroscopy studies of deprotonated polypyrrole and its complexes, Polymer, 32 (1991) 1354-1360.
[116] K.L. Tan, B.T.G. Tan, E.T. Kang, K.G. Neoh, The chemical nature of the nitrogens in polypyrrole and polyaniline: A comparative study by x-ray photoelectron spectroscopy, The Journal of Chemical Physics, (1991).
[117] P. Louette, F. Bodino, J.-J. Pireaux, Poly(pyrrole) (PPY) XPS Reference Core Level and Energy Loss Spectra, Surface Science Spectra, 12 (2005) 84-89.
[118] S.G. Wang, Q. Zhang, R. Wang, S.F. Yoon, A novel multi-walled carbon nanotube-based biosensor for glucose detection, Biochemical and Biophysical Research Communications, 311 (2003) 572-576.
[119] Y. Zhang, P. He, N. Hu, Horseradish peroxidase immobilized in TiO_2 nanoparticle films on pyrolytic graphite electrodes: direct electrochemistry and bioelectrocatalysis, Electrochimica Acta, 49 (2004) 1981-1988.
[120] F.H. Wu, G.C. Zhao, X.W. Wei, Electrocatalytic oxidation of nitric oxide at multi-walled carbon nanotubes modified electrode, Electrochemistry Communications, 4 (2002) 690-694.
[121] J. Zhuang, L. Zhang, W. Lu, D. Shen, R. Zhu, D. Pan, Determination of trace copper in water samples by anodic stripping voltammetry at gold microelectrode, International Journal of Electrochemical Science, 6 (2011) 4690-4699.
[122] A. Mohadesi, A. Salmanipour, S.Z. Mohammadi, A. Pourhatami, M.A. Taher, Stripping voltammetric determination of copper (II) on an overoxidized polypyrrole functionalized with Nitroso-R, J Brazil Chem Soc, 19 (2008) 956-962.
[123] B. Zeng, X. Ding, F. Zhao, Y. Yang, Electrochemical determination of copper(II) by gold electrodes modified with N-acetyl-L-cysteine, Analytical letters, 35 (2002) 2245-2258.

[124] S. Betelu, C. Vautrin-Ul, A. Chaussé, Novel 4-carboxyphenyl-grafted screen-printed electrode for trace Cu(II) determination, Electrochemistry Communications, 11 (2009) 383-386.
[125] Y. Bai, X. Ruan, J. Mo, Y. Xie, Potentiometric stripping analysis of copper using cysteine modified mercury film electrode, Analytica Chimica Acta, 373 (1998) 39-46.
[126] S. Nagarajan, C. Pochat-Bohatier, C. Teyssier, S. Balme, P. Miele, N. Kalkura, V. Cavailles, M. Bechelany, Design of graphene oxide/gelatin electrospun nanocomposite fibers for tissue engineering applications, RSC Advances, 6 (2016) 109150-109156.
[127] Y. Fan, F. Cui, S. Hou, Q. Xu, L. Chen, I.-S. Lee, Culture of neural cells on silicon wafers with nano-scale surface topograph, Journal of neuroscience methods, 120 (2002) 17-23.
[128] S. Claramunt, A. Varea, D. López-Díaz, M.M. Velázquez, A. Cornet, A. Cirera, The importance of interbands on the interpretation of the Raman spectrum of graphene oxide, The Journal of Physical Chemistry C, 119 (2015) 10123-10129.
[129] M. Mowry, D. Palaniuk, C.C. Luhrs, S. Osswald, In situ Raman spectroscopy and thermal analysis of the formation of nitrogen-doped graphene from urea and graphite oxide, Rsc Advances, 3 (2013) 21763-21775.
[130] S. Stankovich, D.A. Dikin, R.D. Piner, K.A. Kohlhaas, A. Kleinhammes, Y. Jia, Y. Wu, S.T. Nguyen, R.S. Ruoff, Synthesis of graphene-based nanosheets via chemical reduction of exfoliated graphite oxide, Carbon, 45 (2007) 1558-1565.
[131] S. Kang, H. Choi, Effect of surface hydrophobicity on the adhesion of S. cerevisiae onto modified surfaces by poly (styrene-ran-sulfonic acid) random copolymers, Colloids and Surfaces B: Biointerfaces, 46 (2005) 70-77.
[132] H. Yang, H. Hu, Z. Ni, C.K. Poh, C. Cong, J. Lin, T. Yu, Comparison of surface-enhanced Raman scattering on graphene oxide, reduced graphene oxide and graphene surfaces, Carbon, 62 (2013) 422-429.
[133] Y.-S. Huang, T. Karashima, M. Yamamoto, H.-o. Hamaguchi, Molecular-level investigation of the structure, transformation, and bioactivity of single living fission yeast cells by time-and space-resolved Raman spectroscopy, Biochemistry, 44 (2005) 10009-10019.
[134] L.d. Chiu, M. Ando, H.o. Hamaguchi, Study of the 'Raman spectroscopic signature of life'in mitochondria isolated from budding yeast, Journal of Raman Spectroscopy, 41 (2010) 2-3.
[135] B. Tan, C. Sow, T. Koh, K. Chin, A. Wee, C. Ong, Fabrication of size-tunable gold nanoparticles array with nanosphere lithography, reactive ion etching, and thermal annealing, The Journal of Physical Chemistry B, 109 (2005) 11100-11109.
[136] K.-C. Kao, H. NISHI, T. Tatsuma, Effects of particle size and annealing on plasmon-induced charge separation at self-assembled gold nanoparticle arrays, Physical Chemistry Chemical Physics, (2018).

[137] T.W. Oates, A. Keller, S. Facsko, A. Mücklich, Aligned silver nanoparticles on rippled silicon templates exhibiting anisotropic plasmon absorption, Plasmonics, 2 (2007) 47-50.
[138] T. Oates, A. Keller, S. Noda, S. Facsko, Self-organized metallic nanoparticle and nanowire arrays from ion-sputtered silicon templates, Applied physics letters, 93 (2008) 063106.
[139] Z. Liu, X. Zhang, Y. Zhang, J. Jiang, Theoretical investigation of the molecular, electronic structures and vibrational spectra of a series of first transition metal phthalocyanines, Spectrochimica Acta Part A: Molecular and Biomolecular Spectroscopy, 67 (2007) 1232-1246.
[140] S.H. Guo, S.J. Tsai, H.C. Kan, D.H. Tsai, M.R. Zachariah, R.J. Phaneuf, The Effect of an Active Substrate on Nanoparticle-Enhanced Fluorescence, Advanced Materials, 20 (2008) 1424-1428.
[141] M. Zhang, J. Qi, M. Jiang, Y. Li, J. Qian, J. Chen, Z. Chen, Q. Sun, J. Xu, Screened bonding, antibonding and charge transfer plasmon modes in conductively connected nanorod heterodimer, Journal of Optics, 20 (2018) 025001.

Santrauka

Įvadas

Jutiklis - įtaisas, aptinkantis analitę ir paverčiantis cheminį jos signalą registruojamu elektriniu signalu. Svarbiausios jutiklio savybės – tai jautrumas, selektyvumas ir stabilumas, o klasifikuojami jie į terminius, cheminius, optinius, drėgnumo, dujų ir kitus.

Elektrocheminis jutiklis tai perspektyvus analizinis prietaisas, kuriame naudojami modifikuoti elektrodai siekiant padidinti jų jautrumą ir atrankumą. Atsižvelgiant į elektrocheminio jutiklio paskirtį, galima keisti modifikavimo procesą ir medžiagas, todėl jie yra lengvai pritaikomi įvairiems tyrimams. Elektrodų modifikavimui naudojamos nanokompozitinės medžiagos, tokios kaip anglies nanovamzdeliai, metalų nanodalelės ir kt., kurios didina elektrodų plotą ir jautrumą. Norint pagerinti elektrodų selektyvumą analitei, modifikavimui gali būti naudojamos specifinės medžiagos arba fermentai. Optimizuojant šiuos du parametrus, gautas elektrodas būna labai jautrus ir selektyvus pasirinktos analitės atžvilgiu.

Ramano spektroskopijos metodas, pateikia informaciją spektrų forma, kurią sudaro molekulinių ryšių virpesiai, kurie atitinka tam tikrą spektro poziciją. Tačiau Ramano signalas gali būti neintensyvus arba sunkiai registruojamas, todėl siekiama jį padidinti. Šiam tikslui naudojama paviršiaus sustiprinta Ramano spektroskopija (SERS) kurioje pritaikomos plazmonų rezonansu pasižyminčios nanodalelės, tokios kaip aukso, sidabro ar kitos. Tačiau kai kuriose SERS tyrimams tinkamose medžiagose, plazmonai rezonuoja tik siaurame spektro ruože, priklausomai nuo nanokompozitų formos, dydžio ir prigimties. Tai riboja tokiomis dalelėmis modifikuotų pagrindų panaudojimą tik tam tikroms analitėms nustatyti. Todėl siekiant išplėsti SERS analizės galimybės, yra kuriami ir panaudojami SERS-paviršiai, pasižymintys dvikrypčiu plazmonų rezonansu.

Darbo tikslas:

π-π konjuguotų junginių sintezė ir jų pritaikymas elektrocheminiuose ir optiniuose jutikliuose.

Darbo uždaviniai:

1. Ekologišką π-π polimero – polipirolo sintezę pritaikyti polipirolo mikrosferų gamybai, panaudojant *Streptomyces spp*. bakterijų štamus MIUG 12p ir MIUG 4.88.
2. Ištirti grafeno oksido, grafeno, magnetito, aukso chitsano ir daugiasluoksnių anglies vamzdelių panaudojimą stikliškosios anglies

elektrodo modifikavimui, siekiant jį pritaikyti elektrocheminiam vario(II) aptikimui.
3. Ištirti optimaliausio elektrodo, pritaikyto vario(II) jonų aptikimui, charakteristikas.
4. Ištirti paviršius, modifikuotus π-π junginiu – grafeno oksido nanolakštais, pavienių ląstelių gavimui.
5. Palyginti vienos ląstelės Ramano spektrą su agregavusių ląstelių Ramano spektru.
6. Ištirti ant banguoto silikono paviršiaus tvarkingai išsidėsčiusių aukso nanodalelių lokalizuoto paviršiaus plazmonų rezonanso signalo priklausomybę nuo pagrindo orientacijos.
7. Modeliuoti plazmonų „karštus taškus“ (angl. *hotspots*) naudojant tikslų nanodalelių dydį, jų formą bei išsidėstymą.

Mokslinis naujumas:

1. *Streptomyces spp.* bakterijos inicijuoja polipirolo mikrosferų susidarymą.
2. Daugiasluoksniai anglies nanovamzdeliai, imobilizuoti ant stikliškosios anglies elektrodo, prieš elektrocheminį 3-nitroanilino modifikavimą ir redukavimą, padidina elektrodo jautrumą vario(II) jonams.
3. Pavienės mielių ląstelės buvo imobilizuotos ant pagrindų, modifikuotų su grafeno oksido nano-plokštelėmis bei jų Ramano spektras pasižymėjo didesniu informacijos kiekiu nei agreguotų ląstelių Ramano spektras.
4. Dviejų žingsnių gamybos metodas, panaudojant jonų spinduliuotę ir įstrižo kampo metalo nusodinimą, yra tinkamas norint gauti didelės apimties, tvarkingai išsidėsčiusiosiomis aukso nanodalelėmis modifikuotus pagrindus, kurie pasižymi dvikrypčiu plazmonų resonansu. Tokiu būdu modifikuoti paviršiai yra tinkami SERS analizei.

Ginamieji teiginiai:

1. Polipirolo mikrosferos gali būti susintetintos naudojant *Streptomyces spp* bakterijų štamus.
2. Modifikavimas anglies daugiasluoksniais nanovamzdeliais ir redukuotu 3-nitroanilinu padidina stikliškosios anglies jautrumą Cu(II) jonams.

3. Grafeno oksido nanoplokštelėmis modifikuoti pagrindai gali būti naudojami pavienių ląstelių imobilizavimui bei Ramano signalo padidinimui.
4. Lyginant agreguotų ląstelių ir pavienių ląstelių, įmobilizuotų ant grafeno oksidu modifikuotų pagrindų, Ramano spektrus, pastarasis pasižymėjo didesniu informacijos kiekiu.
5. Paprastas dviejų žingsnių gamybos metodas yra tinkamas norint gauti didelės apimties, tvarkingai išsidėsčiusiomis aukso nanodalelėmis modifikuotus pagrindus, tinkamus SERS analizei.

1. Polipirolo sintezė naudojant Streptomyces spp bakterijas

Yra žinoma, kad bakterijos išskiria oksidatorius, kurie gali inicijuoti polipirolo sintezę. Šiame darbe polipirpolo (PPy) sintezei buvo pasirinkti dveji *Streptomyces spp.* bakterijų štamai: MIUG 12p ir MIUG 4.88. Pirma bakterijos buvo kultivuotos 1 parą Petri lėkštelėse, tada perkeltos į Elermėjerio kolbas ir dėtos į maišyklę esant 25°C. Po 6 dienų inkubacijos į bakterijų augimo terpę įdėta 30 mM pirolo (Py). Praėjus 4 inkubacijos dienoms stebėtas terpės patamsėjimas dėl susidariusio polipirolo. Tiriant optiniu mikroskopu, (OM) rasti juodi dariniai aplink bakterijų kolonijas. Nustatyta, kad naudojant MIUG 12p ląstelių štamus, susidarę PPy dariniai buvo ~20 μm dydžio ir mažesnės koncentracijos, tuo tarpu naudojant MIUG 4.88 ląstelių štamus susidarę PPy dariniai buvo tik ~10 μm. Tai gali būti paaiškinta tuo, kad terpėje su MIUG 12p bakterijų štamu sintezė prasidėjo anksčiau nei terpėje su MIUG 4.88. Ištyrus susidariusių darinių skerspjūvį su skanuojančiu elektroniniu mikroskopu (SEM), pastebėta, kad susidarę dariniai yra tuščiavidurės sferos formos. Tačiau mikrosferos, gautos naudojant MIUG 4.88, turi plonesnį kiautą lyginant su mikrosferomis, gautomis naudojant MIUG 12p bakterijų štamą.

Furjė transformacijos infraraudonųjų spindulių spektroskopijos (FTIR) metodu palygintos bakteriškai gautos PPy (BPPy) mikrosferos su elektrochemiškai (EPPy) sintetintu PPy bei Py monomeru. Nustatyta, kad skirtingais būdais gauto polipirolo spektrai pasižymi jiems charakteringomis smailėmis, tačiau BPPy spektruose matomas smailių pasislinkimas yra dėl bakterijų augimo terpėje esančių pašalinių medžiagų.

Išsami polipirolo mikrosferų analizė buvo atlikta naudojant rentgeno fotoelektroninę spektroskopiją (XPS), kurios metu BPPy spektrai lyginti su EPPy spektrais bei Py monomero spektru. Svarbu atkreipti dėmesį, kad anglies regione ties ~286 eV atsiranda smailė, kuri atitinka hidroksilo grupę (C-OH). Pastaroji aptinkama polipirolo dariniuose, tokiuose kaip furanas, furfuralas, N-metilpyrolas, forfobilinogenas, o tiriamuose mėginiuose galėjo atsirasti deguoniui prisijungiant iš atmosferos arba sintezės metu. XPS tyrimas taip pat rodo, kad mėginiuose yra vandens molekulė, o didžiausia jos

koncentracija nustatyta EPPy. Azoto regionas išskaidytas į tris grupes: azoto imino (–NH=), antrinio amino (–NH–), ir imidogeno katijonas (**–N**H^+–). Iš XPS rezultatų apskaičiuotos santykinės anglies, azoto bei deguonies koncentracijos PPy ir Py molekulėse. Kadangi C-N jungties koncentracija yra mažesnė už suminę C-C/C-H ir C-OH, galima teigti, kad gryno Py koncentracija yra mažesnė nei jo darinių, o didelė anglies koncentracija dariniuose galėjo susidaryti dėl iš atmosferos prisijungusios anglies. Išanalizavus XPS spektrus galima teigti, kad bakteriškai sintetintas PPy mažai kuo skiriasi ar net yra identiškas elektrochemiškai sintetinam PPy, o iš gautų atomų koncentracijų, įvertinus vandens kiekį, junginių molekulinę formulę galima užrašyti taip: BPPy - $C_{0.617}N_{0.043}O_{0.31}\cdot 0.03H_2O$, Py - $C_{0.618}N_{0.107}O_{0.256}\cdot 0.019H_2O$, ir EPPy - $C_{0.363}N_{0.069}O_{0.286}\cdot 0.282H_2O$. Visose šiose formulėse deguonies kiekis yra ~0.3, o tai žymi, kad PPy darinių kiekis yra vienodas.

2. 3-nitroanilinu ir daugiasluoksniais anglies vamzdeliais modifikuotas elektrodas Cu(II) jonų aptikimui

Nanodalelių adsorbcija ir elektrocheminis nusodinimas, po kurio sekė funkcinių grupių redukcija, buvo pritaikyta elektrocheminiam vario(II) jonų aptikimui. Sąveika tarp Cu(II) jonų ir amino grupių gali būti paaiškinta chelato komplekso formavimusi. Norint ištirti, kuris modifikavimo eiliškumas yra pats efektyviausias, buvo pagaminta keletas skirtingų stikliškosios anglies (GC) elektrodų, kurie buvo pritaikyti Cu(II) jonų aptikimui: (I) tik GC; (II) GC modifikuotas su 3NA (GC/3NA); (III) GC modifikuotas su elektrochemiškai redukuotu 3NA (GC/3NA(red)); (IV) GC/3NA papildomai modifikuotu su nanomežiagomis (GC/3NA/NMs); (V) GC/3NA(red) papildomai modifikuotu su nanomedžiagomis (GC/3NA(red)/NMs), (VI) GC/NMs modifikuotas su 3NA (GC/NMs/3NA); (VII) GC/NMs modifikuotas su elektrochemiškai redukuotu 3NA (GC/NMs/3NA(red)). Pirmiausia ištirta grafeno oksido (GO) įtaka elektrodo jautrumui. Nustatyta, kad stikliškosios anglies elektrodas, modifikuotas GO, tada elektrochemiškai modifikuotas ir redukuotas 3NA, padidina elektrodo jautrumą 6 kartus lyginant tik su GC. Taip yra todėl, kad GO padidina elektrochemiškai aktyvų paviršiaus plotą.

Toliau buvo pasirenkamos nanomedžiagos, kurios labiausiai padidintų elektrodo jautrumą Cu(II) jonams. Tam pasirinktas grafeno oksidas (GO), grafenas (G), magnetitas (Fe_3O_4), aukso chitosanas (AuChts) ir daugiasluoksniai anglies nano-vamzdeliai (MWCNT) ir atitinkamai pagaminti 5 skirtingi elektrodai. Jų elektrocheminis atsakas į Cu(II) jonus buvo palygintas su GC ir GC/3NA(red). Nustatyta, kad GC/MWCNT/3NA(red) padidino elektrodo jautrumą 2 kartus, lyginant su GC/GO/3NA(red), o

lyginant su GC - iki 16 kartų. Tolimesni tyrimai atlikti naudojant GC/MWCNT/3NA(red) elektrodą.

Toliau buvo tiriamos GC/MWCNT/3NA(red) elektrodo charakteristikos, tokios kaip atrankumas, atsikartojamumas, atkuriamumas, pastovumas bei jautrumas. Nustatyta, kad kitų metalų jonai turi mažai įtakos vario jonų generuojamam signalui, kuomet buvo naudojami tokiomis pačiomis koncentracijomis kaip ir varis. Jų įtaką vario elektrocheminio signalo sumažėjimui, nuo didžiausios iki mažiausios, galima užrašyti taip: Co(II)>Mn(II)>Fe(III)>Cd(II)>Pb(II)>Zn(II). Tiriant elektrodo stabilumą, jis buvo laikomas šaldytuve +4°C temperatūroje, 14 parų. Iki 5 parų elektrodo jautrumas sumažėjo 50% ir išliko stabilus likusį laiką. Atkartojamumo tyrimui, pagaminti 3 elektrodai ir pritaikyti Cu(II) aptikimui. Apskaičiuotas reliatyvus standartinis nuokrypis (R.S.V) lygus 6.4%, o atkuriamumo R.S.V. lygus 1.4%. Elektrodo Cu(II) jonų aptikimo riba yra lygi 0.5×10^{-9} M. GC/MWCNT/3NA(red) elektrodas gali būti lyginamas su kitais elektrodais aptariamais publikacijose.

3. Pavienės ląstelės gavimas ir Ramano analizė

Anksčiau manyta, kad visos ląstelės pasižymi tomis pačiomis charakteristikomis ir tiriant jas dauguma spektruose registruojamos informacijos būdavo ignoruojama. Kadangi kiekviena ląstelė yra unikali, jos spektras gali suteikti daugiau informacijos, kai ji yra tiriama atskirai. Pirmiausia pavienių ląstelių imobilizavimui panaudojome GO modifikuotus pagrindus. Buvo pastebėta, kad užlašinus mielių ląstelių vandeninį tirpalą ant stiklo, silikono (Si), orientuoto pirolizinio grafito (HOPG), polidimetilsiloksano (PDMS), ar žėručio, ląstelės, veikiamos vandens judėjimo garavimo procese, agreguojasi. Tačiau padengus pagrindų paviršius GO nanoplokšelėmis, mielių ląstelės įsitvirtina paviršiuje ir susidaro maži agregatai bei pavienės ląstelės. Norint paaiškinti tokį reiškinį, iškeltos kelios hipotezės, kurios atliktais tolimesniais eksperimentais arba paneigtos arba patvirtintos.

Pirma hipotezė - ląstelėms agreguotis neleidžia padidėjęs paviršiaus šiurkštumas, kuriam ištirti buvo pritaikytas atominių jėgų mikroskopas (AFM). Nustatyta, kad GO nanoplokštelės skerspjūvis yra apie (1.7 ± 0.1) nm, o paviršiaus šiurkštumo šaknies vidurkio kvadratas (Rq) yra (1.5 ± 0.2) nm. Lyginant su stiklo (0.4 ± 0.2) nm šiurkštumu, Rq matmuo yra gana didelis, tačiau lyginant su mielės ląstele (~4 μm), toks šiurkštumas yra nereikšmingas. Todėl ši hipotezė yra paneigiama.

Kita hipotezė - GO nanoplokštelės padidina paviršiaus hidrofiliškumą. Šiam tyrimui atlikti vandens lašo kampo matavimai ant visų

pagrindų prieš ir po modifikavimo GO nanoplokštelėmis. Nors ir hidrofiliškumas padidėjo nuo 14% iki 69%, tačiau negalima teigti, kad tai yra tokio reiškinio priežastis, nes vandens lašo kampo matavimų rezultatai, gauti po paviršiaus modifikavimo su GO, dalinai sutampa su matavimų rezultatais, atliktais prieš modifikavimą.

Trečia hipotezė - tarp baltymų, esančių mielių paviršiuje, bei funkcinių grupų, esančių ant GO paviršiaus, susidaro cheminiai ryšiai ir taip traukiantis lašui džiūvimo procese ląstelės išsilaiko pagrindo paviršiuje. Tam patikrinti buvo atlikta terminė GO redukcija, kurios metu dauguma funkcinių grupių pašalintos. Pokyčių tyrimams panaudota Ramano spektroskopijos metodas naudojant 514.7 nm lazerį. Spektre matomi GO charakteringi D ir G ryšiai, kurie atsiranda dėl sp^2 ir sp^3 vibracijų, bei kitos smailės kurios atsiranda dėl defektų esančių ar atsiradusių anglies struktūroje. D ir G Ramano ryšiai buvo išskaidyti į dar 5, siekiant tiksliau ištirti medžiagos pokyčius. Ryšiai D* ir D" po terminės redukcijos atitinkamai pasislinko link ilgesnių ir trumpesnių bangų ilgių, kas rodo deguonies kiekio mažėjimą. G ryšio poslinkį link ilgesnių bangos ilgių paaiškina grafito struktūros amorfizacija. Ištyrus pagrindus prieš ir po terminės redukcijos naudojant AFM matoma, kad GO nanoplokštelės yra žymiai sumažėjusios ir atsirado papildomos nanostruktūros, o paviršiaus šiurkštumas padidėjo nuo 1.6 nm iki 4.5 nm. Tačiau stebint mielių tirpalo lašo džiūvimo procesą, pastebėta, kad mielės agreguojasi ant redukuoto GO paviršiaus taip pat kaip ir ant paviršių kurie nebuvo modifikuoti. Tai patvirtina hipotezę, kad mielės įsitvirtina ant GO dėl susidariusio cheminio ryšio tarp baltymų esančių ant mielių ląstelės paviršiaus ir GO funkcinių grupių.

Palyginus Ramano mielių spektrus registruotus mielių ląsteles imobilizavus ant stiklo su spektrais mielių ląsteles imobilizavus ant GO modifikuoto stiklo, pastebėta, kad GO padidina signalą 100%. Palyginus pavienių mielių ląstelių spektrus su agreguotų mielių ląstelių spektrais, pastebėtos baltymų ir lipidų smailės, kurios žymi ląstelės sąveiką su ląstele. Šios smailės agreguotos ląstelės spektre dingo arba buvo ženkliai sumažėjusios normalizuojant spektrą.

4. Tvarkingai organizuotos aukso nanostruktūros su dvikrypčiu plazmonų rezonansu

Dviejų žingsnių gamybos metodas buvo pritaikytas formuojant SERS pagrindą pasižymintį dvikrypčiu plazmonų rezonansu. Pirmiausia naudojant jonų spinduliuotę silikono pagrindo paviršiuje yra išgaunamos lygiagrečių bangų raštas, tada tarp bangų nusodinamas auksas. Keičiant nusodinamo Au storį, gaunamos skirtingos formos Au nanostruktūros. Pradedant nuo 30 nm

storio sluoksnio aiškiai matosi tvarkingai išsidėsčiusios Au nanodalelės palei silikono paviršiuje esančias bangeles. Didinant storį, forma pradeda kisti, bet vientisas aukso sluoksnis nesusidaro. Papildomai atlikus mėginio kaitinimą su 30 nm storio Au, nanodalelės pakito iš ovalios formos į sferinę.

Adsorbcinė spektroskopinė elipsometrija (SE) atlikta ant Au nanodalelėmis padengtų pagrindų parodė, kad lokalizuoto paviršiaus plazmonų rezonansas (LSPR) gali būti sužadintas skirtinguose bangų ruožuose priklausomai nuo statmenos ($E_\perp$) ar lygiagrečios ($E_\parallel$) poliarizacijos paviršiaus bangavimui. $E_\perp$ LSPR yra pastebima ties ~600 nm ir slenka link ilgesnių bangos ilgių kartu su didėjančiu Au sluoksnio storiu, kuomet $E_\parallel$ - nuo ~800 nm ir platėja. Ramano spektroskopija, naudojant 632.8 nm lazerio apšvietimą, buvo atlikta ant mėginių, padengtų kobalto ftalocianinu (CoPc). Keičiant poliarizaciją, molekulės Ramano signalas keičiasi. Buvo analizuojamas CoPc A_{1g} vibracinis Ramano režimas, kuris yra ties 687 cm^{-1}, bei apskaičiuotas signalo stiprinimo faktorius (EF) CoPc kuris lygus ~150 - ~1200. Didžiausias signalo sustiprinimas buvo pastebėtas $E_\perp$, kas reiškia, kad signalą dominuoja sritys, esančios tarp Au grandinių.

Kadangi labiausiai išreikšta nanodalelių geometrija buvo ant paviršių, padengtų 30 nm Au storiu, šie mėginiai kaitinti papildomai. Po kaitinimo dalelės tapo tikslesnės sferinės formos. LSPR poslinkis ir įtaka SERS ištirta atlikus Ramano spektroskopiją, kurios metu buvo pritaikyti trijų bangos ilgių (532 nm, 638 nm ir 785 nm) lazeriai.

Naudojant 532 nm monochromatinį šviesos šaltini anizotropija nebuvo stebėta ant kaitinto ir nekaitinto mėginio. Taip yra todėl, kad LSPR neatitinka molekulės plazmonų rezonanso ir dėl to Ramano sužadinimas yra žemas. Naudojant 638 nm lazerio sužadinimą ant kaitinto mėginio su 30 nm Au storiu, aiškiai matomas anizotropiškas SERS efektas bei pastebimas didelis signalo sustiprinimas $E_\parallel$, tuo tarpu nekaitintame mėginyje stebimas didelis SERS atsakas $E_\perp$. Naudojant 785 nm bangų ilgio lazerį šis reiškinys yra atvirkščias. Tai patvirtina ir SE rezultatai.

Skaičiavimai baigtinių elementų metodu (BEM) buvo atlikti norint nustatyti „karštų taškų“ pasiskirstymą kaitintuose ir nekaitintuose mėginiuose. Kaitintame mėginyje po 638 nm lazerio sužadinimo, plazmoniniai „karšti taškai“ yra matomi išilgai dalelių grandinės. $E_\perp$ mažesnis lauko sustiprinimas yra matomas statmenai bangų raštui. Skerspjūvio modelyje pastebėta, kad didelė elektrinio lauko dalis yra susikoncentravusi vietinio oksido sluoksnyje po Au nanodalele. Situacija nekaitintame mėginyje yra šiek tiek sudėtingesnė, nes dalelės yra ovalios formos. Taip pat nehomogeniškas dalelių dydis, proporcijų santykis ir formų pasiskirstymas sąlygoja LSPR sužadinimą plačioje spektro dalyje. Grandinės struktūra, sudaryta iš tarpusavyje sujungtų ovalios formos dalelių, taip pat gali būti susijusi su „karštais taškais“,

esančiais $E_{\parallel}$ kryptyje kuomet yra naudojamas 785 nm lazerio sužadinimas. Tačiau SE ir Ramano spektroskopijos rezultatai rodo, kad $E_{\perp}$ kryptimi 785 nm monochromatinės šviesos šaltiniu sužadinimas nesutampa su LSPR, ir „karštų taškų“ nesimato, tik silpnas plazmonų jungimasis išilgai dalelių grandinių. Taip pat svarbu paminėti, kad modelyje apskaičiuotas signalo sustiprinimas yra 1-3 kartus mažesnis nei gautas eksperimentiniu būdu. Taip yra todėl, kad signalo sustiprinimas kyla iš kelių, bet labai stiprių „karštų taškų“, esančiu tarp dviejų „šiurkščių“ dalelių, ir dėl šios priežasties toks mėginys negali būti visiškai aprašomas BEM skaičiavimais.

Bendrosios išvados

1. Polipirolo mikrosferos gali būti sėkmingai susintetintos naudojant 2 skirtingus *Streptomyces spp*. MIUG 12p bei MIUG 4.88 bakterijų štamus. Mikrosferos, gautos naudojant *Streptomyces spp*. MIUG 12p štamą, buvo ~20 μm skersmens ir mažesnės koncentracijos, nei gautos naudojant MIUG 4.88, kurios buvo ~10 μm skersmens bei tuščiavidurės.
2. Stikliškosios anglies elektrodas, kuris buvo modifikuotas daugiasluoksniais anglies nano-vamzdeliais ir vėliau modifikuotas redukuotu 3-nitroanilinu, 16 kartų padidino jautrumą Cu(II) jonams, lyginant su nemodifikuotu stikliškosios anglies elektrodu.
3. GC/MWCNT/3NA(red) elektrodo atrankumo tyrimas parodė, kad šis elektrodas selektyvus Cu (II) jonams. Stabilumo tyrimas parodė, kad GC/MWCNT/3NA(red) elektrodo signalas vario (II) jonams po 5 dienų sumažėjo 50% ir išliko stabilus iki 14 dienų. Elektrodas gali būti naudojamas aptikti iki 0.5×10^{-9} M Cu(II) jonų.
4. Pavienės mielių ląstelės ant pagrindų, modifikuotų grafeno oksido nanoplokštelėmis, prisitvirtina baltymų esančių ant ląstelių paviršiaus kurie jungiasi su grafeno oksido funkcinėmis grupėmis pagalba.
5. Mielių ląstelių, įmobilizuotų ant grafeno oksidu modifikuoto stiklo, Ramano signalas padidėjo 100%, lyginant su mielių ląstelių, įmobilizuotų ant stiklo, Ramano signalu. Ramano spektruose, gautuose iš pavienių ląstelių, matomos smailės, kurios priskiriamos baltymams, lipidams, braduolio rūgštims, tačiau jų nėra agreguotų ląstelių, imobilizuotų ant GO modifikuoto paviršiaus, Ramano spektruose.
6. SERS pagrindų, pagamintų naudojant dviejų pakopų metodą, stiprinimo faktorius yra iki ~1200 kartų lyginant su ant silikono pagrindo molekulės Ramano signalu. Keičiant aukso sluoksnio storį ir mėginio orientaciją, galima suderinti lokalizuotą paviršiaus plazmonų rezonansą su skirtingais lazerių bangos ilgiais.

7. Naudojant baigtinių elementų modelį nustatyta, kad elektromagnetinis laukas kaitintame banguoto silikono pagrinde su 30 nm aukso sluoksniu, apšvietus 638 nm monochromatinės šviesos šaltiniu, yra išilgai nanodalelių grandinių. Kuomet nekaitintame analogiškame mėginyje sužadinus 785 nm monochromatinės šviesos šaltinu - statmenai nanodalelių grandinių. Keičiant pagrindo orientaciją, lokalizuotas paviršiaus plazmonų rezonansas tokiame mėginyje yra sužadinamas skirtinguose bangų ilgiuose.

Acknowledgments

First of all, I would like to express my enormous gratitude towards my supervisor and mentor Prof. Dr. Arūnas Ramanavičius for the possibility to work under his guidance and for providing me encouragement in every aspect of the research and life. For giving me motivation when I seem to have none left.

I would like to thank Vilnius University and Faculty of Chemistry and Geosciences staff for the possibility to study doctoral studies as well as for providing me the option to travel and perform my researches abroad with COST STSM and Erasmus programs. Also, I would like to thank Technical University of Chemnitz for giving me the opportunity to perform a research with InProTuc program.

There are no words in which I could express my gratitude to professor Raul D. Rodriguez who was my supervisor in Germany. I am thankful for all the knowledge that he passed on to me, for being not only a supervisor but also a friend and even allowing me to feel a part of TERS-Team family. Also, I would like to give my separate gratitude to the members of TERS-Team. From the very first day there you made me feel like I am at home and I will never forget all the support, help, consultations, questions and answers that you provided.

There is another professor that I am grateful for the possibility to work with which is Yasemin Oztekin. She was the one who took me under her wing and helped me with everything that I needed when I came for the first time in a foreign country. I am also grateful for the all the knowledge that she provided and always giving me motivation and support to be better and work harder.

I would like to thank my colleagues Eva Raudonyte-Svirbutiene, Lina Pavasaryte and Justina Gaidukevic-Daksevic for always being there when I needed and always providing me with warm and witty company. They were the shoulder I could lean to because they understood.

Last but not least, I would like to thank my father and mother, who were always supporting with my life choices and providing me independence. I know that they are proud of all that I achieved. I would also like to thank to my dear sister and brothers who were listen to my complaining, gave me all the moral support and helped me with my decision making and friends for giving me distractions when I needed.

Circulum Vitae

EDUCATION

2013 – 2018 Vilnius University, Faculty of Chemistry and Geoscience, doctoral studies in Chemistry, study program Physical Chemistry.
2011 – 2013 Vilnius University, Faculty of Chemistry, MSc degree in Chemistry, study programme Analytical Chemistry.
2007 – 2011 Vilnius University, Faculty of Chemistry, Bachelor of Chemistry, study programme Conservation and Restoration Chemistry.

ACADEMIC POSITIONS

2015.03 – 2016.07 Vilnius University, Faculty of Chemistry and Geoscience, Department of Physical chemistry, Physical Chemistry Laboratory, Lectureship

PROFESSIONAL TRAINING

1. Erasmus Student Internship, 2016-09 – 2017-09, Chemnitz University of Technology (Germany);
2. InProTuc Project, 2016-01 – 2016.04, Chemnitz University of Technology (Germany);
3. COST Short Term Scientific Mission, 2014-09 – 11, Selcuk University (Turkey).

CONFERENCES

1. **L. Dedelaite**, M. Ersoz, Y. Oztekin, A. Ramanavicius, Electrochemical modification of electrode by poly-nano aniline layers as metal sensing systems. Advanced Materials and Technologies, Palanga, Lithuania, 2015 - 08 – 27-31
2. **L. Dedelaite**, R. D. Rodriguez, L. Mikoliunaite, E. Andriukonis, M. Hietschold, A. Ramanavicius, D. R.T. Zahn, Investigation of single cells on specifically modified surface. Current Trends of Cancer Theranostics, Druskininkai, Lithuania, 2016 – 07 – 19-23

Original papers

Paper 1

Synthesis of polypyrrole microspheres by *Streptomyces* spp

A. Stirke, R. M. Apetrei, M. Kirsnyte, L. Dedelaite, V. Bondarenka, V. Jasulaitiene, M. Pucetaite, A. Selskis, G. Carac, G. Bahrim

Polymer 84 (2016) 99-106.

Polymer 84 (2016) 99–106

Contents lists available at ScienceDirect

Polymer

journal homepage: www.elsevier.com/locate/polymer

Synthesis of polypyrrole microspheres by *Streptomyces* spp.☆

Arunas Stirke [a, *], Roxana-Mihaela Apetrei [b], Monika Kirsnyte [a], Lina Dedelaite [c], Vladimiras Bondarenka [a, f], Vitalija Jasulaitiene [d], Milda Pucetaite [e], Algis Selskis [d], Geta Carac [b], Gabriela Bahrim [b], Arunas Ramanavicius [a, c]

[a] Center for Physical Sciences and Technology, Semiconductor Physics Institute, A. Gostauto 11, LT-01108 Vilnius, Lithuania
[b] "Dunarea de Jos" University of Galati, Domneasca Street 111, 800201 Galati, Romania
[c] Vilnius University, Naugarduko 24, LT-03225 Vilnius, Lithuania
[d] Center for Physical Sciences and Technology, Institute of Chemistry, A. Gostauto 9, LT-01108 Vilnius, Lithuania
[e] Vilnius University, Sauletekio av. 9 bl. 3, LT-10234 Vilnius, Lithuania
[f] Lithuanian University of Educational Sciences, Studentu 39, LT-08106 Vilnius, Lithuania

ARTICLE INFO

Article history:
Received 5 September 2015
Received in revised form
25 November 2015
Accepted 16 December 2015
Available online 25 December 2015

Keywords:
Polypyrrole
Streptomyces
Hollow microspheres

ABSTRACT

The present paper shows a green method for the formation of polypyrrole by two different MIUG 12p and MIUG 4.88 strains of *Streptomyces* spp. bacteria. According to our knowledge, such method has never been proposed before for pyrrole oxidation. For this experiment pyrrole monomer was added into bacterial medium after 6 days of incubation and after 4 days polypyrrole (PPy) based 10–25 μm microspheres has been observed in the medium around living cells, The microsphere diameter dependence on the bacterial strains was observed. The morphological characterization of the PPy microspheres was subsequently performed by optical microscopy (OM), scanning electron microscopy (SEM), Fourier transform infrared spectroscopy (FTIR) and X-ray photoelectron spectroscopy. The characterization of formed hollow microspheres confirmed that they consist of polypyrrole.

1. Introduction

The field of conducting polymers has attracted a lot of interest because conducting polymers have shown tremendous scientific and technological advantages. The possibility of combining in these materials the properties of organic polymers and the electronic properties of semiconductors has been the driving force for various applications [1].

Polypyrrole or black pyrrole is known since 1961 when it was first synthesized in chemical oxidation method using pyrrole monomer. This insoluble monomer was not analyzed in detail at that time. Various experiments started 1968 when first PPy layer was synthesized using electrochemical oxidation method. Since then various improvements were made for polypyrrole synthesis. Over the past twenty years, the PPy stands out to be the most extensively studied conducting polymer mainly because of its simple synthesis, environmental stability, good redox properties, biocompatibility and variable electrical conductivity. As a result of its good intrinsic properties, PPy has proven to be promising for several applications including biosensors, actuators, batteries, antistatic coatings, tissue engineering [2] and drug delivery systems [3].

Most common methods for pyrrole synthesis are electrochemical and chemical oxidations. The chemical oxidation is an easy method that involves the oxidation of pyrrole in aqueous medium, commonly using ferric chloride or ammonium persulfate as oxidizing agent, resulting in an electrically conductive black powder. On the other hand, the electrochemical oxidation of pyrrole is carried out without adding chemical oxidizers, but it is limited to deposit polypyrrole (PPy) films onto the electrically conducting substrate used as working electrode. Other methods, such as vapour-phase [4] induced polymerization generate PPy without using solvent; nevertheless the synthesized polymer contains a significant amount of oxidation by-products.

Abbreviations: ATR, attenuated total reflection; BPPy, bacterial synthesized polypyrrole; EPPy, electrochemical synthesized polypyrrole; FIB-SEM, focused ion beam-scanning electron microscope; MIUG, Microbial Cultures Collection of the Bioaliment Research Center, Faculty of Food Science and Engineering of 'Dunarea de Jos' University of Galati, Romania; OM, optical microscopy; PPy, polypyrrole; Py, pyrrole; XPS, X-ray photoelectron spectroscopy.

☆ This article is dedicated to Professor V. Bondarenka, co-author, who died recently.

* Corresponding author. Center for Physical Sciences and Technology, A. Gostauto 11, Vilnius LT-01108, Lithuania.
E-mail address: arunas.stirke@ftmc.lt (A. Stirke).

http://dx.doi.org/10.1016/j.polymer.2015.12.029
0032-3861/

However, despite the amount of work already done in polypyrrole polymerization, there has been a special attention given to the mechanism of PPy synthesis (Scheme 1). There is growing interest to an enzymatic method that is more efficient and environmentally friendly at the same time. Since usual chemical methods for the production of PPy were based on application of strong oxidants and mostly were performed in strongly acidic media, therefore the biomedical application of such polypyrrole has been problematic, due to traces of toxic materials present in the formed polymer, which become entrapped during the course of polymerization [5].

Developments in the biological synthesis of nanoparticles and polymers on a commercial scale are still in their infancy stage, but are attracting attention of many material scientists throughout the world. Microorganism-assisted biological synthesis is safe and economically viable prospect for novel material synthesis approach. Bacterial, fungi [6] or other microorganism-assisted synthesis can be used for polymer, metal nanoparticle [7] or other diverse material [8] synthesis. Therefore there is demand to develop more "greener" routes for the synthesis of more advanced polymers such as PPy. Ideal conditions for PPy synthesis would be at neutral pH and in aqueous environment [9]. In order to fulfill these conditions huge interest is growing on synthesizing more environmentally friendly polymers. It has been reported that more environmentally friendly chemical oxidants, such as hydrogen peroxide (H_2O_2) could polymerize pyrrole [10]. However this polymerization is very fast and results in large quantities of side products. Other reported polymerization methods for PPy have included using catalytic amounts of ferric chloride hexahydrate ($FeCl_3 \cdot 6H_2O$) [11], iron porphyrin enzyme mimics [12], and the enzymes horseradish peroxidase (HRP), glucose oxidas, and laccase [13].

In order to develop a 'green' PPy synthesis method in this report *Streptomyces* sp. bacteria was applied as potential initiator of PPy synthesis. It is Gram positive bacteria involved in the formation and/or degradation of complex biopolymers like lignin, melanin and humic substances [14]. *Streptomyces* spp was deeply studied because of their capacity to produce antibiotics and enzymes of industrial importance, such as glucose isomerase, protease, amylase, xylanase, laccase and tyrosinase, which are synthesized intracellular and then transported into the growth medium [15]. In this way it is possible to synthesize polymers using synthetic routes that can be carried out in mild environments and even around living cells. The general aim of this study was to investigate the possibility to synthesize polypyrrole using two bacterial strains of *Streptomyces* spp. In this research proposed method to polymerize pyrrole is an environmentally friendly route, carried out in mild aqueous media and free of oxidation by-products. Further morphologic characterization of polypyrrole was performed using different spectroscopy techniques.

2. Experimental section

2.1. Bacterial growth conditions and PPy polymerization

Two different *Streptomyces* spp. strains MIUG 12p and MIUG 4.88 were provided from the Microbial Cultures Collection of the Bioaliment Research Center, Faculty of Food Science and Engineering of 'Dunarea de Jos' University of Galati, Romania (MIUG) [16]. Microorganisms have been cultivated from pure cultures in Petri dishes using Gause medium No.1 (GMA) and incubated for 6 days at 25 °C.

The composition of solid growth medium was as following: 2.5% agar, 2% potato flakes, 0.05% K_2HPO_4, 0.05% $MgSO_4 \times 7H_2O$, 0.1% KNO_3, 0.05% NaCl, 0.001% $FeSO_4 \times 7H_2O$ (Sigma Aldrich) dissolved in 1000 mL distilled water. The liquid medium had the same components except agar. Mediums have been sterilized in an autoclave at 121 °C for 20 min. All used chemicals and solvents were obtained from various commercial suppliers and were of the highest purity available.

The biosynthesis of the enzymes entails a submerged fermentation system for the selected strains of *Streptomyces* spp., in liquid composition, providing intense aeration and mixing of the fermentation broth so that the cells have equal access to nutrients and oxygen during the fermentation.

The culture suspension of 5 mL with sterile distilled water was transferred aseptically into 250 mL Erlenmeyer flasks containing 100 mL of liquid growth medium. After inoculation, the flasks were placed on the shaker with controlled speed of 150 rpm and temperature of 25 °C for 10 days. The microorganisms have been multiplying increasing the turbidity of the culture medium in the specified conditions. After six days of inoculation pyrrole monomer, which was purchased from Sigma Aldrich, was added.

In order to estimate the optimum pyrrole concentration used for synthesis seven 250 mL Erlenmeyer flasks with 100 mL bacterium medium were prepared as described above. After 6 days of inoculation different pyrrole concentrations 10, 20, 30, 40, 60, 80 mM were added into 6 flasks and left in the shaker for 4 more days. In same conditions one flask without pyrrole was also analyzed as control example. The bacteria vitality and PPy morphological properties were analyzed using optical microscope.

For comparison electrochemical polypyrrole was synthesized. For this synthesis special electrochemical grating (500 μl volume) and potentiostat PGSTAT 30 Autolab (Netherland) were used. Electrochemical grating consists of three electrodes – platinum (Pt) working electrode on which PPy layer is synthesized, Ag/AgCl reference electrode and Pt counter electrode. Reference and counter electrodes are placed on the bottom of grating and working electrode on top. In order to synthesize PPy 0.05 mol/L phosphate buffer (pH 6.0) with 500 mM pyrrole was used. Few methods were

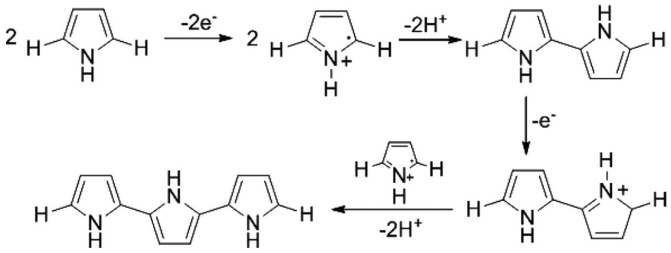

Scheme 1. Oxidative polymerization of pyrrole.

applied for electrochemical synthesis – cyclic voltammetry (30 cycles from 0 to 1 V) and pulsed amperometric (10 pulses – the first pulse of 1.0 V, the second pulse of 0 V, the pulse of the third 1.0 V, the fourth pulse of 0 V, etc.).

2.2. Characterization

The sample for morphological analysis was prepared by centrifugation of 1 mL of bacteria medium after 6 and 10 days of incubation with added pyrrole and the obtained sediment used for optical microscopy. The analysis was performed using optical microscope OLYMPUS BX51 (Japan). Additionally the morphology of microspheres were analyzed using dual beam system Helios Nanolab 650, (FIB-SEM), FEI. Cross-sections of microspheres were prepared using Ga^{+} ion beam. The analysis protocol entails the centrifugation and washing of the sample, subsequently placed on a gold slide and covered with platinum foil in order to provide a conductive surface for the microscope image.

The samples for Fourier transform infrared spectroscopy (FTIR) were prepared using two different methods:

1. KBr pellet method. FTIR spectrums of sample were obtained by preparing a KBr pellets. About 2 mg sample was mixed with 200 mg KBr powder and pressed under hydraulic "Specac" press using 10 t weight pressure into thin 13 nm diameter KBr pellets that were used for registering spectrum transmittance.
2. Attenuated total reflection (ATR) method. Dry sample was placed directly on diamond ATR "prism" and spectrums were obtained.

Using KBr pellets spectrums were obtained using "BRUKER VERTEX70" FTIR (USA) Spectrophotometer, which uses globar IR emitter, liquid nitrogen cooling mercury cadmium telluride sensor and KBr ray divider. Spectrums were obtained at a nominal resolution of 4 cm^{-1} at 4000–600 cm^{-1} ranges.

ATR method spectrums were registered using "BRUKER ALPHA" FTIR (USA) spectrophotometer that uses global IR emitter, DTGS sensor and KBr ray divider. Other spectrum registration parameters are as described previously.

For the characterization of the surface composition of microspheres the X-ray Photoelectron Spectroscopy (XPS) was used for the pure pyrrole (Py), electrochemically synthesized polypyrrole (EPPy) and bacterial synthesized polypyrrole (BPPy) (microspheres). Samples were prepared by centrifuging the bacterial medium and spreading PPy as thin layer on gold covered chip that was washed with distilled water and placing the chip in incubator (+25 °C) for 30–60 min to dry.

X-ray photoelectron spectra were recorded with a spectrometer "ESCALAB MK II" (VG Scientific, Great Britain). The photoelectrons were excited using a non-monochromatized MgKa radiation (1253.6 eV). The working pressure in the analysis chamber was 5×10^{-8} Torr during the spectrum analysis. The photoemission data of C 1s, O 1s, and N 1s regions has been collected and processed. After the MgKa source satellites and background deduction the multiple photoelectron spectra were separated into several peaks setting the peak position: binding energy (BE), area (A), width (FWHM), and Gaussian/Lorentzian (G/L) ratio. The accuracy of the relative intensities and BE of the measured lines were about 10% and 0.1 eV respectively. The random C 1s line BE which should have been equal to 284.6 eV was used for the correction of the charging effects. After Shirley background subtraction, a non-linear least squares curve fitting routine with a Gaussian/Lorentzian product function was used for the analysis of XPS spectra.

3. Results and discussion

3.1. Formation of PPy microspheres

After 10 days of inoculation of the bacterial medium with pyrrole monomer, changes in flasks were noticed. Flasks that contained 30, 60, 80 mmol/L pyrrole were darker than flasks with 10, 20 mmol/L pyrrole. After optical microscopy analysis in samples with 30, 60, 80 mM pyrrole dark round microspheres around vital bacterial colonies were visible at x40 magnification. For further experiments 30 mM pyrrole concentration was chosen.

Optical microscopy was used in order to provide evidence of the polypyrrole microspheres formed in the bacterial medium. The images depicted in Fig. 1 shows the black compact microspheres from 10 to 25 μm in diameter.

The monomer was added into the bacterial medium after six days since the inoculation. The optical analysis was performed after two days when polymerization product appears visible by optical microscope. In each of the samples, optical images revealed black PPy microspheres. However, while the PPy microspheres were formed in the MIUG 12p (Fig. 1a) based medium they appeared at around 20 μm diameter, the ones formed in MIUG 4.88 based medium (Fig. 1b) were being smaller in size. Additionally, the concentration of PPy microspheres formed in MIUG 12p medium is 8 times lower with average of 24 microspheres in 1 μl in contrast to the microspheres in MIUG 4.88 medium with average of 188 pcs./μl.

Optical microscopy (OM) was the primary analysis tool in the morphological investigations of our samples. Initially, it was used to determine the size, shape and vitality of the bacterial colonies formed in the fermentation medium of *Streptomyces* spp. strains. Subsequently, after the addition of pyrrole monomer, the morphological characteristics of PPy microspheres were also analyzed. Optical density measurements have been used in order to asess the biomass development during the experiment. Samples have been collected at every 48 h for 10 days considering the addition of pyrrole in the 6th day and the evaluation of the polymerization starting 10th day. The bacterial strains show increased development starting with day 4 until the 8th day when becomes stationary. The pyrrole does not prove to induce any growth inhibition for this microorganisms.

Furthermore, coupling of FIB-SEM analysis was used to obtain topographical, morphological and compositional information about the PPy microspheres formed in the fermentation medium. The SEM microscope uses focused beams of electrons to magnify and obtain two-dimensional images of the PPy microspheres.

OM and SEM imaging revealed black, globular-shaped microspheres of PPy with 10–20 μm diameters. The PPy microspheres obtained in MIUG 12p based fermentation medium are about 20 μm, which is bigger as the one in MIUG 4.88 based medium, but the concentration of them is 8 times lower in MIUG 12p medium. This may be attributed to the slower polymerization in the MIUG 4.88 based medium. The PPy microspheres were formed earlier in MIUG 12p medium and they got the time to aggregate. Usually using other methods of PPy synthesis particle size can vary. Kim and et. has fabricated PPy nanospheres by chemical reaction using ferric chloride ($FeCl_3$) as an oxidant in various continuous phases such as octanol, benzene and ethyl acetate. The average size of the spheres were around 600 nm, though images shown that they were consist of 40 nm PPy particles, moreover altering water and octanol volume ratios size got reduced to 60 nm and lower [17]. However, smaller PPy nanoparticles changed their morphology from nanospheres into shell-like morphology. Other researchers Liu and et has analyzed alcohol influence to PPy particle formation. In their research transmission electron microscopy (TEM) and SEM images confirmed that the diameter of spherical shape PPy particles,

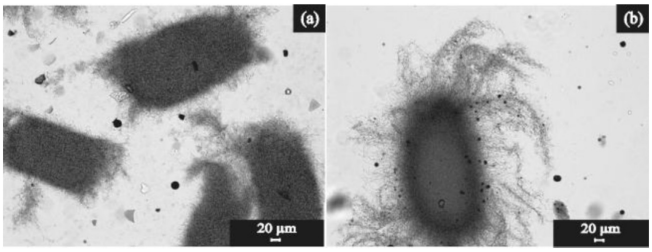

Fig. 1. Optical microscopy images of PPy microspheres obtained by *Streptomyces* spp.: (a) MIUG 12p strain; (b) MIUG 4.88 strain.

without using alcohol in the synthesis process, varied from 50 to 70 nm. After adding *n*-amyl alcohol the diameter reduced to 30 nm and obtained particles were monodispersed, differently from synthesis without alcohol where particles were conglutinated [18]. Using H_2O_2 in PPy synthesis, particle diameter was about 28–30 nm, in comparison with glucose oxidase initiated PPy synthesis precipitate appeared in ~50 nm diameter particles which formed clusters of micrometer-size PPy nanoparticles that were visible by immersing optical microscope [19]. Compared with chemically synthesized PPy, biocatalytical PPy appears in bigger sizes if it is synthesized using enzyme.

3.2. FIB-SEM imaging of PPy microspheres

The FIB-SEM technology was used to increase the accuracy of the analysis, because it allows a better resolution and an improved perspective of the cross-section interior of the PPy microspheres. Scanning electron micrographs of the PPy samples are depicted in Fig. 2.

The PPy microspheres obtained in the fermentation medium of the strain MIUG 12p are about 20 μm in size and prove a dense structure. The concentration of PPy microspheres obtained in the fermentation medium of strain MIUG 4.88 twice higher but smaller in size what is in agreement with previously presented SEM images. Their structure is not as resistant as the one of microspheres formed in MIUG 12p medium, their top bends under the action of vacuum used in the SEM analysis. The inside view though, indicates some sort of substance trapped in the middle of the PPy microspheres.

FIB-SEM microscopy has provided interesting information giving further insight into the morphological and compositional properties of the PPy microspheres. This device represents a combination of SEM and FIB systems, a high-resolution field emission scanning electron microscope and a scanning ion-beam microscope. This microscope has a dual beam that was used to scan the area of interest at low magnification and subsequently zoom in, for further analysis on an ultrastructural level, rendering valuable and detailed three-dimensional information of the PPy microspheres. Moreover, the ion beam has the ability to cross-section the polypyrrole microspheres and it revealed that the resistance of the PPy microspheres is better if they are formed in MIUG 12p than in MIUG 4.88 fermentation medium being that they have a more compact and dense structure. The reason of that could be the possibility that polymerization of pyrrole starts earlier and more intense with MIUG 12p bacteria, which gives time for polymer to grow more dense. Also FIB-SEM analysis showed that PPy microspheres are hollow unlike PPy particles obtained by many other synthesis

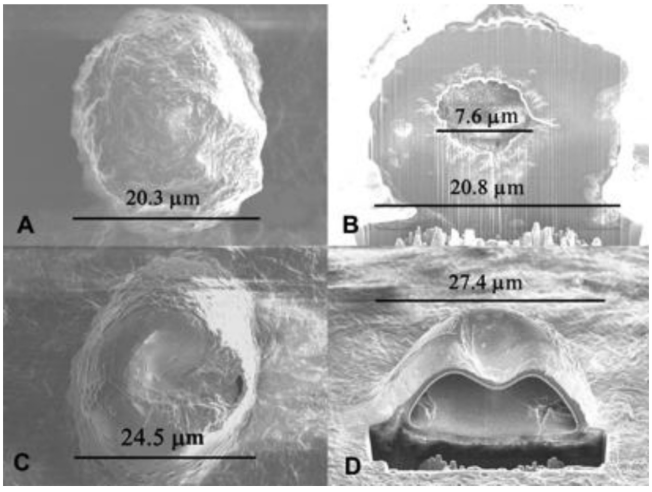

Fig. 2. FIB-SEM images of PPy microspheres obtained by incubation *Streptomyces* spp. based medium: (A,B) MIUG 12p strain; (C, D) MIUG 4.88 strain. A, C – top view; B, D – cross section, view angle 53°.

methods. Obtaining hollow PPy microspheres throughout biocatalytic synthesis is a feature attractive to develop drug delivery systems [20], since it provides an option to entrap desired materials into the microspheres in order to form microspheres suitable for delivery of entrapped materials. The hollow structures of Ppy, especially conducting it's strains, was investigated as potential material for the artificial muscle [21], conductive wires [22], improving the properties of Li-Ion batteries [23] and shielding from electromagnetic interference (EMI) [24].

3.3. FTIR spectrums

FTIR spectrums of pure pyrrole (Py), bacterial synthesized polypyrrole (BPPy) and electrochemically-synthesized polypyrrole (EPPy) were obtained. Wet samples for analysis were lyophilized and FTIR spectrums were obtained. The FTIR absorption spectrums of Py, BPPY and EPPy shown in Fig. 3 exhibited characteristic vibration bands at 1530 cm^{-1} for pyrrole ring stretching at C=C band. Wide peaks at 3300 cm^{-1} and 3400 cm^{-1} is attributed to pyrrole ring N–H stretch vibrations. Intense peak at 1678 cm^{-1} is assigned for the stretching vibration of the acetate C=O group which could occur due to enzymes. Peaks between 1450 and 1300 cm^{-1} occurs due to C–C and C–N conjugated stretching. Other peak, which is common for polypyrrole spectrums at 1236 cm^{-1}, is attributed to C–N in plane deformation [21]. Furthermore peaks at 1035 cm^{-1} and 726 cm^{-1} are due to N–H wagging vibrations.

FTIR was used to identify of chemical bonds in microspheres by producing an infrared absorption spectrum [25]. Both spectrums of PPy that were obtained from biocatalytic synthesis using *Streptomyces* spp. and spectrum that was obtained from electrochemically synthesized PPy exhibited characteristic peaks of polypyrrole. The shift of peaks in spectrums from PPy microspheres that was synthesized using bacteria could be because of additional products in the synthesis solution, such as starch, and/or presence of bacterial byproducts. This fact is concerning and further use of polymer will demand extra steps of PPy microspheres purification.

3.4. Photoelectron spectra

Measured survey XPS spectra for all investigated compounds are similar and practically don't differ from the spectra of electrodeposited films of polypyrrole [26]. The energy loss regions of major elements in spectrum: carbon, nitrogen and oxygen peaks were analyzed.

3.5. Carbon region

For all investigated compounds C 1s peak consists of three components with binding energies 284.6 eV, ~286 eV, and ~288 eV that corresponds to carbon – carbon and carbon – hydrogen (C – C/C – H), carbon in hydroxyl group (C – OH), and carbon – protonated nitrogen (C – N^{+}) [27] chemical bond. As example, Fig. 4a presents more detailed C 1s peak fitting results for bacterial synthesized polypyrrole.

3.6. Oxygen region

Fig. 4b presents deconvolution of O 1s peak for BPPy compound. Similar fitting results were obtained for Py and EPPy samples. In all cases O 1s peak consists from three components with binding energies ~531 eV, ~532 eV, and ~533 eV. The interpretation of given experimental results become complicated because oxygen ions are not involved into the structure of pyrrole. But its derivatives (such as furan, furfural, N-methylpyrrole, porphobilinogen, pyrrole-3-carboxylic acid, and so on) comprised of carbonyl, carboxyl groups, and also N – C/N – C – O bindings [28]. Thus fitting component with binding energy ~531 eV can be attributed to carbonyl group [29]. Then component with binding energy ~532 eV may be accredited as carboxyl groups (because the difference between oxygen ions in oxide (O^{2-}) and hydroxyl (OH^{-}) states binding energies is ~1 eV) and bindings between oxygen, carbon and nitrogen [30] (carboxyl/N component in Fig. 4b). The last fitting component with binding energy ~533 eV corresponds to oxygen ions in water molecules [31] (Fig. 4b). It must be pointed that similar approach was applied in Ref. [32] setting up the chemical bonds of O 1s peak components.

3.7. Nitrogen region

For BPPy (see Fig. 4c) as well as for Py and EPPy compounds, N 1s

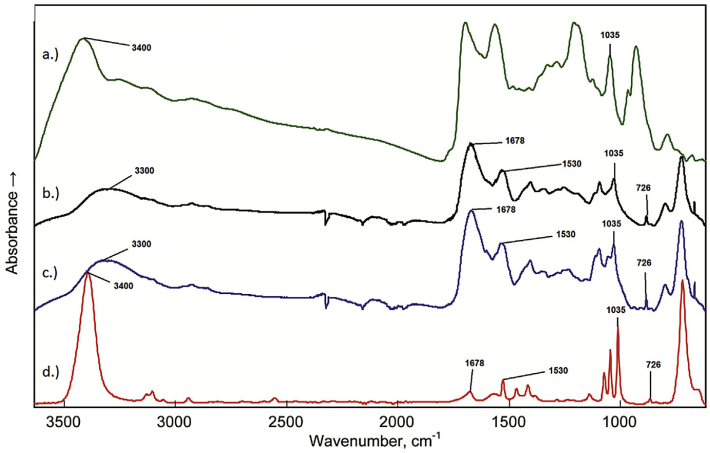

Fig. 3. FTIR spectrum of polypyrrole synthesized: (a) electrochemicaly; (b) MIUG 12p strain; (c) MIUG 4.88 strain; (d) pyrrole.

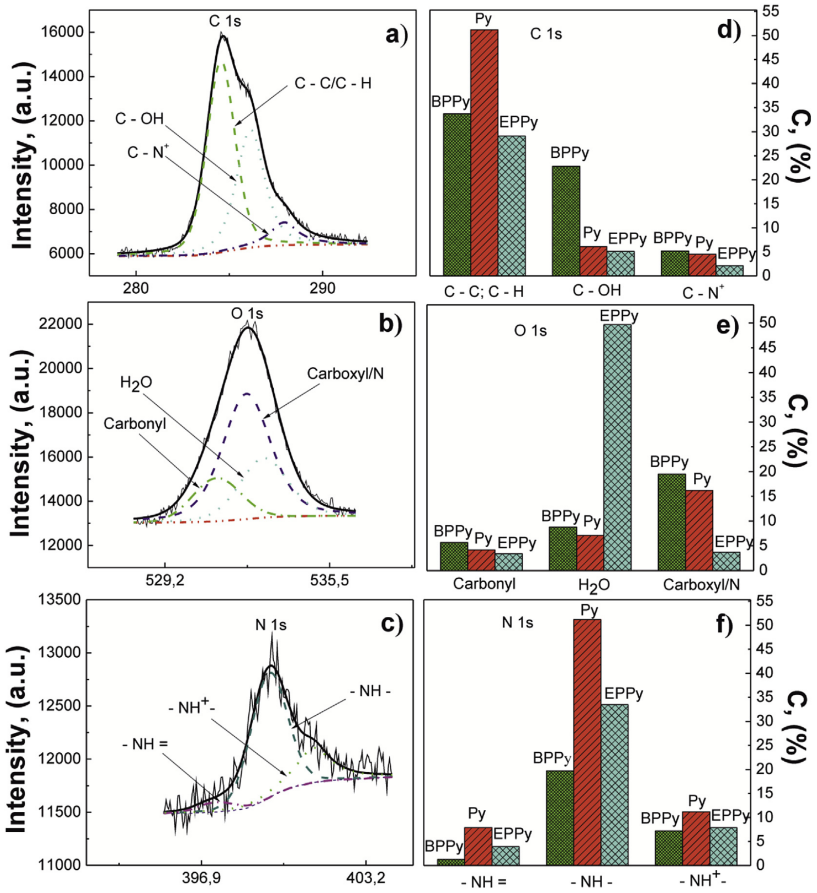

Fig. 4. XPS spectra of bacterial synthesized polypyrrole (BBPy) of (a) C 1s; (b) O 1s; (c) N 1s; histograms of relative concentration of (d) carbon ions in various chemical bonds (BPPy, Py, EPPy); (e) oxygen ions in various chemical bonds (BPPy, Py, EPPy); (f) nitrogen ions in various chemical bonds (BPPy, Py, EPPy).

peak was deconvoluted in three components with binding energies ~ 398 eV, ~400 eV, and ~401 eV that corresponds to nitrogen in imine state (−NH−), amine nitrogen (−NH−) [27], and protonated nitrogen (−NH^+−) [33].

The relative concentrations of carbon, nitrogen, and oxygen ions, which are involved in various chemical bonds, are shown in Fig. 4d, e, and f.

The total content of nitrogen in investigated samples is highest for pure pyrrole (Fig. 5, Column N) when the distribution of nitrogen ions under their chemical binding is similar for all samples (Fig. 4f) – highest concentration of amine group then follows protonated amine and least – for nitrogen ions in imine group. It means that in pure pyrrole (sample Py) the concentration of pyrrole is the highest between all used Py samples. From results presented in Fig. 4d follows that the concentration of real pyrrole in all investigated samples is smaller than the concentration of derivatives of pyrrole, because the concentration of C–N bonds is lower then the sum of concentrations of C – C/C – H and C – OH bonds. The total carbon concentration (Fig. 5) is *fairly large* (61.7%, 61.8% and 36.3% for BPPy, Py and EPPy respectively). It may be explain by carbon absorption from environment.

The concentrations of carbon, nitrogen, and oxygen ions for all investigated compounds are shown in Fig. 5. The results, which are shown in Fig. 4a–f and Fig. 5 are calculated from experimentally registered XPS spectra for C 1s, O 1s, and N 1s peaks, and their deconvolution into separate components.

As follows from Fig. 5 results, the chemical formulas of investigated samples may be written as: $C_{0.617}N_{0.043}O_{0.34}$, $C_{0.618}N_{0.107}O_{0.275}$, and $C_{0.363}N_{0.069}O_{0.568}$ for BPPy, Py, and EPPy respectively. The highest concentration of oxygen ions (Fig. 5, O column) is observed for EPPy sample. This fact related with highest concentration of water in EPPy compound (Fig. 4e, H_2O columns). The appearance of water can be explained in two ways. First – absorption of water molecules from **e**nvironment and second – infiltration of water into structure of the samples during synthesis process. The amounts of oxygen ions in water molecules in BPPy, Py,

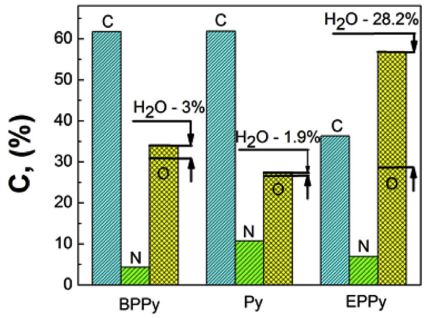

Fig. 5. Histogram of carbon, nitrogen, and oxygen concentrations in investigated compounds (BPPy – bacterial synthesized polypyrrole, Py – pure pyrrole, and EPPy – electrochemically synthesized polypyrrole; H_2O – X % – relative concentration of water molecules).

and EPPy samples are equal to 8.8%, 7.1%, and 49.7% (Fig. 4e, H_2O columns) of total oxygen quantity (total oxygen quantity – 34%, 27.5%, and 56.8% for BPPy, Py, and EPPy samples (Fig. 5). Then the general formulas of BPPy, Py, and EPPy must be written as $C_{0.617}N_{0.043}O_{0.31}\cdot 0.03H_2O$, $C_{0.618}N_{0.107}O_{0.256}\cdot 0.019H_2O$, and $C_{0.363}N_{0.069}O_{0.286}\cdot 0.282H_2O$ respectively. In this case the amount of oxygen (marked as bold in last formulas) is approximately equal to 0.3 for all samples. It means that the quantity of pyrrole derivatives is the same for all investigated compounds. In this way, we have to speak about pyrrole as a hydrated compound, which consists of several pyrrole derivatives.

4. Conclusions

Streptomyces spp. bacteria synthesized novel type of hollow polypyrrole microspheres. The observation by optical microscopy revealed that microspheres formed in the bacterial medium was from 10 to 25 μm in diameter. It was found that diameter and interior cross-section of microspheres depending from the strain of bacteria. Microspheres obtained by strain MIUG 4.88 was smaller in size and not as resistant as the one of microspheres formed by MIUG 12p, their top bends under the action of vacuum used in the SEM analysis. Moreover, the quantity of pyrrole derivatives is the same for all investigated variant of pyrrole polymerization. Concluding, in this article we presented innovative biocatalytic synthesis for hollow PPy microspheres, which could be applied in bio-mimetic materials, molecular electronics, shielding applications, nanomedicine and bioremediation.

Acknowledgment

The European Social Fund under the Global Grant measure funded this research. We thank J. Varanovič for providing electrochemically-synthesized polypyrole.

References

[1] A.G. MacDiarmid, "Synthetic metals": a novel role for organic polymers (Nobel Lecture), Angew. Chem. Int. Ed. 40 (14) (2001) 2581–2590.
[2] Y. Wan, H. Wu, D. Wen, Porous-Conductive chitosan scaffolds for tissue engineering, 1, Macromol. Biosci. 4 (9) (2004) 882–890.
[3] (a) P. Chandrasekhar, B.J. Zay, T. McQueeney, G.C. Birur, V. Sitaram, R. Menon, M. Coviello, R.L. Elsenbaumer, Physical, chemical, theoretical aspects of conducting polymer electrochromics in the visible, IR and microwave regions, Synth. Met. 155 (3) (2005) 623–627;
(b) T.A. Skotheim, R.L. Elsenbaumer, J.R. Reynolds, Handbook of Conducting Polymers, second ed., M. Dekker, New York, 1998 p xiii, 1097 pp.;
(c) H.S. Nalwa, Handbook of Organic Conductive Molecules and Polymers, Wiley, Chichester ; New York, 1997;
(d) S. Sadki, P. Schottland, N. Brodie, G. Sabouraud, The mechanisms of pyrrole electropolymerization, Chem. Soc. Rev. 29 (5) (2000) 283–293.
[4] V. Bocchi, G. Gardini, S. Rapi, Highly electroconductive polypyrrole composites, J. Mater. Sci. Lett. 6 (11) (1987) 1283–1284.
[5] A. Vaitkuviene, V. Kaseta, J. Voronovic, G. Ramanauskaite, G. Biziuleviciene, A. Ramanaviciene, A. Ramanavicius, Evaluation of cytotoxicity of polypyrrole nanoparticles synthesized by oxidative polymerization, J. Hazard. Mater. 250 (2013) 167–174.
[6] A. Chauhan, S. Zubair, S. Tufail, A. Sherwani, M. Sajid, S.C. Raman, A. Azam, M. Owais, Fungus-mediated biological synthesis of gold nanoparticles: potential in detection of liver cancer, Int. J. nanomedicine 6 (2011) 2305.
[7] (a) R. Sindhu, A. Pandey, P. Binod, Microbial diversity of nanoparticle biosynthesis, in: Bio-nanoparticles, John Wiley & Sons, Inc, 2015, pp. 187–203;
(b) H. Korbekandi, S. Iravani, S. Abbasi, Production of nanoparticles using organisms, Crit. Rev. Biotechnol. 29 (4) (2009) 279–306.
[8] D. Byrom, Polymer synthesis by microorganisms: technology and economics, Trends Biotechnol. 5 (9) (1987) 246–250.
[9] R. Bouldin, S. Ravichandran, A. Kokil, R. Garhwal, S. Nagarajan, J. Kumar, F.F. Bruno, L.A. Samuelson, R. Nagarajan, Synthesis of polypyrrole with fewer structural defects using enzyme catalysis, Synth. Met. 161 (15–16) (2011) 1611–1617.
[10] K. Leonavicius, A. Ramanaviciene, A. Ramanavicius, Polymerization model for hydrogen peroxide initiated synthesis of polypyrrole nanoparticles, Langmuir 27 (17) (2011) 10970–10976.
[11] H.V.R. Dias, M. Fianchini, R.M.G. Rajapakse, Greener method for high-quality polypyrrole, Polymer 47 (21) (2006) 7349–7354.
[12] F.F. Bruno, S.A. Fossey, S. Nagarajan, R. Nagarajan, J. Kumar, L.A. Samuelson, Biomimetic synthesis of water-soluble conducting copolymers/homopolymers of pyrrole and 3,4-ethylenedioxythiophene, Biomacromolecules 7 (2) (2005) 586–589.
[13] J. Tabaciarová, M. Mičušík, P. Fedorko, M. Omastová, Study of polypyrrole aging by XPS, FTIR and conductivity measurements, Polym. Degrad. Stab. 120 (2015) 392–401.
[14] K.F. Chater, S. Biró, K.J. Lee, T. Palmer, H. Schrempf, The complex extracellular biology of *Streptomyces*, FEMS Microbiol. Rev. 34 (2) (2010) 171–198.
[15] C. Popa, L. Favier, G. Bahrim, testing of the new streptomyces strains for production of phenoloxidases, Food Technol. 37 (2) (2013) 35–46.
[16] M. Cotarlet, G. Bahrim, T. Negoita, P. Stougaard, Screening of polar streptomycetes able to produce cold-active hydrolytic enzymes using common and chromogenic substrates, Romanian Biotechnol. Lett. 13 (5, suppl) (2008) 69–80.
[17] S.W. Kim, H.G. Cho, C.R. Park, Fabrication of unagglomerated polypyrrole nanospheres with controlled sizes from a surfactant-free emulsion system, Langmuir 25 (16) (2009) 9030–9036.
[18] Y. Liu, Y. Chu, L. Yang, Adjusting the inner-structure of polypyrrole nanoparticles through microemulsion polymerization, Mater. Chem. Phys. 98 (2–3) (2006) 304–308.
[19] A. Ramanavicius, A. Kausaite, A. Ramanaviciene, J. Acaite, A. Malinauskas, Redox enzyme – glucose oxidase – initiated synthesis of polypyrrole, Synth. Met. 156 (5–6) (2006) 409–413.
[20] P.M. George, D.A. LaVan, J.A. Burdick, C.Y. Chen, E. Liang, R. Langer, Electrically controlled drug delivery from biotin-doped conductive polypyrrole, Adv. Mater. 18 (5) (2006) 577–581.
[21] P. Novák, B. Rasch, W. Vielstich, Overoxidation of polypyrrole in propylene carbonate an in situ FTIR study, J. Electrochem. Soc. 138 (11) (1991) 3300–3304.
[22] A. Kros, J.G. Linhardt, H.K. Bowman, D.A. Tirrell, From giant vesicles to filaments and wires: templates for conducting polymers, Adv. Mater. 16 (8) (2004) 723–726.
[23] F.H. Du, B. Li, W. Fu, Y.J. Xiong, K.X. Wang, J.S. Chen, Surface binding of polypyrrole on porous silicon hollow nanospheres for Li-Ion battery anodes with high structure stability, Adv. Mater. 26 (35) (2014) 6145–6150.
[24] R. Panigrahi, S.K. Srivastava, Trapping of microwave radiation in hollow polypyrrole microsphere through enhanced internal reflection: a novel approach, Sci. Rep. 5 (2015).
[25] X. Lu, D. Chao, J. Chen, W. Zhang, Y. Wei, Preparation and characterization of inorganic/organic hybrid nanocomposites based on Au nanoparticles and polypyrrole, Mater. Lett. 60 (23) (2006) 2851–2854.
[26] P. Louette, F. Bodino, J.-J. Pireaux, Poly(pyrrole) (PPY) XPS reference core level and energy loss spectra, Surf. Sci. Spectra 12 (1) (2005) 84–89.
[27] L. Sabbatini, C. Malitesta, E. De Giglio, I. Losito, L. Torsi, P. Zambonin, Electrosynthesised thin polymer films: the role of XPS in the design of application oriented innovative materials, J. Electron Spectrosc. Relat. Phenom. 100 (1) (1999) 35–53.
[28] A.L. Harreus, R. Backes, J.O. Eichler, R. Feuerhake, C. Jäkel, U. Mahn, R. Pinkos, R. Vogelsang, 2-Pyrrolidone. In Ullmann's Encyclopedia of Industrial Chemistry, Wiley-VCH Verlag GmbH & Co. KGaA, 2000.
[29] (a) S.D. Gardner, C.S.K. Singamsetty, G.L. Booth, G.-R. He, C.U. Pittman Jr., Surface characterization of carbon fibers using angle-resolved XPS and ISS, Carbon 33 (5) (1995) 587–595;
(b) S. Delpeux, F. Beguin, R. Benoit, R. Erre, N. Manolova, I. Rashkov, Fullerene

core star-like polymers—1. Preparation from fullerenes and mono-azidopolyethers, Eur. Polym. J. 34 (7) (1998) 905–915.
[30] L.N. Bui, N.B. Thompson M Fau – McKeown, A.D. McKeown Nb Fau – Romaschin, P.G. Romaschin Ad Fau – Kalman, P.G. Kalman, Surface Modification Of The Biomedical Polymer Poly(Ethylene Terephthalate), 1993, pp. 463–474, 0003–2654 (Print)).
[31] S. Yamamoto, H. Bluhm, K. Andersson, G. Ketteler, H. Ogasawara, M. Salmeron, A. Nilsson, In situ x-ray photoelectron spectroscopy studies of water on metals and oxides at ambient conditions, J. Phys. Condens. Matter 20 (18) (2008) 184025.
[32] I. Frateur, J. Lecoeur, S. Zanna, C.O.A. Olsson, D. Landolt, P. Marcus, Adsorption of BSA on passivated chromium studied by a flow-cell EQCM and XPS, Electrochimica Acta 52 (27) (2007) 7660–7669.
[33] (a) E.T. Kang, K.G. Neoh, Y.K. Ong, K.L. Tan, B.T.G. Tan, X-ray photoelectron spectroscopy studies of deprotonated polypyrrole and its complexes, Polymer 32 (8) (1991) 1354–1360;
(b) K.L. Tan, B.T.G. Tan, E.T. Kang, K.G. Neoh, The chemical nature of the nitrogens in polypyrrole and polyaniline: a comparative study by x-ray photoelectron spectroscopy, J. Chem. Phys. 94 (8) (1991), http://dx.doi.org/10.1063/1.460524.

Paper 2

Electrochemical determination of Cu(II) ions using glassy carbon electrode modified by some nanomaterials and 3-nitroaniline

L. Dedelaite, S. Kizilkaya, H. Incebay, H. Ciftci, M. Ersoz, Z. Yazicigil, Y. Oztekin, A. Ramanaviciene, A. Ramanavicius

Colloids and Surfaces A: Physicochemical and Engineering Aspects 483 (2015) 279-284

Colloids and Surfaces A: Physicochem. Eng. Aspects 483 (2015) 279–284

Contents lists available at ScienceDirect

Colloids and Surfaces A: Physicochemical and Engineering Aspects

journal homepage: www.elsevier.com/locate/colsurfa

Electrochemical determination of Cu(II) ions using glassy carbon electrode modified by some nanomaterials and 3-nitroaniline

Lina Dedelaite[a], Selin Kizilkaya[c], Hilal Incebay[d], Hakan Ciftci[e], Mustafa Ersoz[b,c], Zafer Yazicigil[c], Yasemin Oztekin[b,c], Almira Ramanaviciene[f], Arunas Ramanavicius[a,*]

[a] Vilnius University, Faculty of Chemistry, Department of Physical Chemistry, Vilnius, Lithuania
[b] Selcuk University, Advanced Technology Research and Application Center, Konya, Turkey
[c] Selcuk University, Faculty of Science, Department of Chemistry, Konya, Turkey
[d] Nevsehir Haci Bektas Veli University, Faculty of Science and Lecture, Department of Chemistry, Nevsehir, Turkey
[e] Kirikkale University, Kirikkale Vocational High School, Department of Chemistry and Chemical Processing Technologies, Kirikkale, Turkey
[f] Vilnius University, NanoTechnas, Center of Nanotechnology and Materials Science, Vilnius, Lithuania

HIGHLIGHTS

- Glassy carbon (GC) electrodes were initially modified by several nanomaterials.
- Then these electrodes were electrochemically modified by poly-3-nitroaniline (poly-3NA).
- Modified electrodes were sensitive for Cu(II) ions.
- Differential pulse voltammetry was applied for determination of Cu(II) ions.
- GC electrode modified with MWCNTs and poly-3NA was the most sensitive toward Cu(II).

GRAPHICAL ABSTRACT

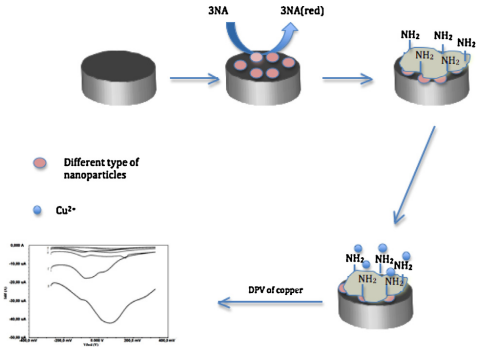

ARTICLE INFO

Article history:
Received 10 February 2015
Received in revised form 17 May 2015
Accepted 19 May 2015
Available online 19 July 2015

Keywords:
Conducting polymer
Electrochemical deposition
Nitroaniline
Polyaniline
Graphene
Graphene oxide
Nanomaterials
Cu(II) ion determination

ABSTRACT

The aim of this research was to investigate the effect of the several nanomaterials in electrochemical determination of Cu(II) ions. For this aim, firstly the deposition of graphene oxide (GO), graphene, magnetite (Fe_3O_4), gold-chitosan (AuChts) or multilayer carbon nanotubes (MWCNTs) on the glassy carbon (GC) electrode surface was performed. Then the electrochemical modification of electrode by poly-3-nitroaniline (poly-3NA) was performed by 100 potential cycles in the range between +0.9 V and +1.4 V vs. $Ag/AgNO_3$ at the sweep rate of 100 mV/s. For electrochemical reduction of nitro groups present on modified GC electrode surface, potential cycling was performed in 100 mM HCl between −0.1 V and −0.8 V vs. $Ag/AgCl/(KCl_{sat.})$ at the sweep rate of 100 mV/s. Nanomaterial and poly-3NA modified electrodes were applied in the determination of Cu(II) ions by differential pulse voltammetry. It was determined that GC electrodes consecutively modified with MWCNTs, poly-3NA and then by electrochemical reduction of nitro groups were the most sensitive towards Cu(II) ions with detection limit of 0.5×10^{-9} M.

* Corresponding author. Fax: +370 5 2 301658.
E-mail address: arunas.ramanavicius@chf.vu.lt (A. Ramanavicius).

http://dx.doi.org/10.1016/j.colsurfa.2015.05.054
0927-7757/

1. Introduction

Some heavy metals at particular concentrations are known to be essential for human metabolism due to formation of metallo-proteins and metallo-enzymes and their importance in transcriptional events [1,2]. Copper in the form of Cu(II) ions is one of the most important heavy metal for living species and according to distribution in human organism among the other heavy metals it takes the third place after iron and zinc ions [3]. However with the increasing human activities such as metal plating, application of fertilizers, mining, development and usage of electrical devices, laptops, mobile phones, batteries and pesticides, large quantities of copper is released into the environment [4–6]. Aqueous solutions containing Cu(II) ions are used and/or produced and they are potential pollutants. In many industrial countries, soil contaminated by a variety of heavy metals such as copper is found in hazardous waste sites, which could be a result of illegal or inappropriate drainage of waste water. Copper compounds tends to accumulate in the living organisms and through edible plants and animals, copper compounds can enter into human food chain or into beverages [7]. Long-term exposure to excess of Cu(II) ions can increase the risk of many diseases including gastrointestinal disturbance, liver or kidney damage, neurodegenerative diseases, amyotrophic lateral sclerosis, cancer, Alzheimer's disease, etc [8,9]. Cu(II) ions are especially toxic for microorganisms, such as algae, fungi, bacteria and viruses [10]. Based on above mentioned facts there has been always huge interest in the development of simple and fast methods suitable for Cu(II) ion determination [11–13].

In the most natural samples the amount and/or concentration of Cu(II) ion is relatively low, therefore, effective measurements for the determination of Cu(II) ion traces are highly desired. Most of the copper analysis have been performed by conventional methods such as atomic absorption/emission spectroscopy [14], graphite furnace atomic absorption spectroscopy [15], inductively coupled plasma mass spectrometry [11,16], inductively coupled plasma optical emission spectroscopy with solid phase extraction [17,18], X-ray fluorescence [19,20], colorimetric analysis [21], chemiluminescence based detection [22,23] and neutron activation analysis [12]. Each of the mentioned analysis has its own distinct advantages, but also there are some limitations related to practical application of these techniques, including inconvenient and time-consuming procedures, requirement of expensive equipment and sophisticated maintenance, etc. As a consequence, there is a growing interest in the development of electrochemical sensors, which would be suitable for the determination of Cu(II) ion concentration. Such sensors should be robust, sensitive, compact, simple, low cost, reliable, easily adaptable and selective [13,24–28].

Solid state electrodes, such as gold, platinum or carbon have superior electrochemical properties, but various carbon forms are preferred because of being electrochemically inert and having wide potential window suitable for electrochemical detection, good conductivity and resistance to environmental and chemical hazards [29]. Due to these facts all carbon based electrodes seem very promising for electrochemical analytical systems [30]. To enhance and/or to extend carbon electrode properties some modifications of the surfaces are applied [31]. Recently, there has been increasing interest in electrodes' surface modification with some conductive/non-conductive polymers, organic and inorganic molecules due to their ability to bind various metal ions [9,13,27,28,32,33]. Moreover, for certain electroanalytical requirements in order to detect various analytes as individual, selective or simultaneous detection, the carbon electrodes have been modified with various nanomaterials (NMs). Main advantages of the application of a NMs-modified electrode when compared to others: high effective surface area, mass transport, catalysis and control over local microenvironment. The electrochemical sensors based on unmodified/modified nanostructured carbon materials could be applied in sensors suitable for the detection of chemical and biochemical analytes [34,35].

In this study new electrode for Cu(II) ion detection by stripping voltammetry is suggested and evaluated. In order to increase analytical characteristics of this electrode glassy carbon electrode was modified with graphene oxide (GO), graphene, magnetite (Fe_3O_4), gold-chitosan (AuChts) or multilayer carbon nanotubes (MWCNTs) in order to increase electrochemically active surface and then electrodes were modified with electrochemically reduced 3NA to obtain electrochemically active area for Cu(II) ion detection.

2. Experimental

All chemicals used in this study were of analytical grade and were purchased from Merck, Riedel and Sigma–Aldrich companies. All NMs except MWCNTs were synthesized using the purest available chemicals, which were additionally purified by procedures described in other references [36–39], while MWCNTs was purchased from Sigma–Aldrich.

Electrochemical measurements were performed using a Gamry Reference 750 Potentiostat/Galvanostat from Gamry Instruments (PA, USA) equipped with a C3 cell stand. Glassy carbon electrodes of 0.071 cm^2 geometric area were used as working electrodes. Platinum wire was used as a counter electrode. Ag/AgCl in saturated KCl (Ag/AgCl/($KCl_{sat.}$)) was applied as a reference electrode for the experiments, which were performed in aqueous media; or a Ag/Ag^+ in 10 mM $AgNO_3$ ($Ag/AgNO_3$) was applied for the experiments, which were performed in non-aqueous media. All experiments were carried out inside a Faraday cage at a room temperature. In order to avoid contamination and to obtain a clean renewed electrode surface: the surface of the bare GC electrode was hand-polished as described before [40,41].

Electrochemical modification of GC electrode surface was performed with Gamry PCI4/750 potentiostat controlled by PHE 200 software. Modification protocol was carried by using 3NA and performed by 100 reversible potential cycles between +0.9 V and +1.4 V in acetonitrile (CH_3CN) including 100 mM tetrabutylammoniumtetrafluoroborate (TBATFB). After the modification of the GC electrode, the surface of obtained GC/3NA electrode was carefully washed with pure water. Electrochemical reduction of nitro groups on the GC/3NA surface to amino groups was performed by 100 potential cycles in 100 mM HCl solution in the potential range between −0.1 V and −0.8 V at scan rate of 100 mV/s [28]. Deposition of nanomaterials on bare, modified and/or reduced electrodes' surfaces was performed by dropping twice 5 μL drops of NMs prepared in pure water as 1 mg/mL solution. Subsequently, it was dried in the air. Modification procedures are schematically depicted in Scheme 1.

In order to investigate the effect of selected nanomaterials to the electrochemical determination of copper (II) ions by modified GC electrode surfaces previously described by our research group [28], in this study, several different types of electrodes were designed and evaluated: (I) bare GC; (II) GC/3NA; (III) GC/3NA(red); (IV) several GC electrodes differently modified with selected nanomaterials and 3NA. For copper determination all electrodes were immersed in aqueous 1 mM Cu(II) ions containing solutions prepared in Britton–Robinson (BR) buffer solution, pH 5.0, for five minutes. After immersion electrode was carefully washed with pure water and stable potential (STB POT) was applied for Cu(II) ions reduction into metallic copper (1). This process then was followed by differential pulse voltammetry (DPV), which was performed in the range of −0.3 V to +0.3 V vs. Ag/AgCl/KCl_{sat} with a pulse amplitude of 50 mV, pulse time of 0.1 s, pulse period (interval) of 1 s and a voltage step of 2 mV in BR buffer solution, pH 5.0. During this

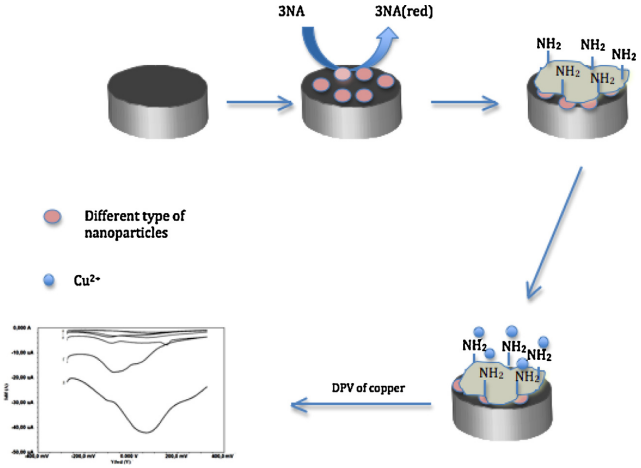

Scheme 1. Schematic presentation of electrode modification and evaluation procedure.

stage copper is being oxidized back to its preliminary state (2). All results were compared with that obtained using bare GC electrode, GC/3NA and GC/3NA(red) electrodes.

$$Cu^{2+} + 2e^- \rightarrow Cu \quad (1)$$

$$Cu - 2e^- \rightarrow Cu^{2+} \quad (2)$$

In order to investigate proposed electrodes' selectivity for Cu(II) ions test was performed in the presence of the 1 mM interfering Zn(II), Cd(II), Pb(II), Mn(II), Co(II), Fe(III) metal ions together with 1 mM Cu(II) ions in BR buffer solution, pH 5.0. Stability test was performed by storing prepared electrode in argon (Ar) atmosphere at +4 °C in refrigerator for 0, 1, 4 and 14 days. Reproducibility test was performed using three different GC electrodes, which were prepared in exact same conditions. Moreover, repeatability test was performed using same electrode for copper detection multiple times. Between detections, electrode was washed with pure water and ethylenediamine tetraacetic acid (EDTA). For all experiments STB POT and DPV analysis were applied.

3. Results and discussion

Adsorption and electrochemical deposition followed by reduction of functional groups on the modified GC electrodes' surface were combined for electrochemical detection of Cu(II) ion. The interaction mechanism of the Cu(II) ions and the amino groups can be explained by interaction of amino groups and Cu(II) ions and formation chelate complex (Fig. 1), which is taking place on modified electrode surface. On the other hand, the efficiency of 3NA modified surfaces was enhanced by nanomaterials, which were applied in this research. For this aim, number of differently modified electrodes was prepared by the deposition of NMs before or after electrochemical modification with 3NA; the electrodes were classified into several groups: (I) bare GC; (II) GC modified with 3NA (GC/3NA); (III) GC modified with electrochemically reduced 3NA (GC/3NA(red)); (IV) GC/3NA additionally modified with nanomaterial (GC/3NA/NMs); (V) 3NA(red)/GC additionally modified with nanomaterial (GC/3NA(red)/NMs), (VI) GC modified with nanomaterial (GC/NMs) and then modified with 3NA (GC/NMs/3NA); (VII) GC modified with nanomaterial and then modified with electrochemically reduced 3NA (GC/NMs/3NA(red)). Then these electrodes were applied for the electrochemical determination of Cu(II) ions. Firstly GO and 3NA/GO modified electrodes were evaluated. DPV results, which are shown in Fig. 2, illustrate that the highest DPV peak was observed at −0.06 V towards Cu(II) ions with GC/NMs/3NA(red) electrode.

Dependently on oxidation reduction process and oxidation state copper ions have several reduction potentials for various reduction processes $Cu^{2+} + 2e^- \rightarrow Cu$ of +0.34 V, $Cu^{2+} + e^- \rightarrow Cu^+$ +0.15 V, $Cu^+ + e^- \rightarrow Cu$ + 0.52 V vs. hydrogen electrode at standard conditions (at partial pressure of 1 atmosphere and at 25 °C (298 K) temperature when concentrations of initial Cu-ion solutions are 1 M). However, under different experimental conditions (e.g., ion concentration, electrode material, reference electrode, etc.) this potential can vary [42,43]. GC electrode modified by electrochemically reduced poly-4NA (GC/4NA(red)) has been already investigated by Oztekin et al. [28] and this electrode has been found suitable for Cu(II) determination. But differently from the previous article present research

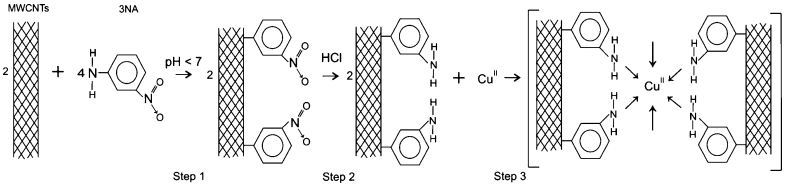

Fig. 1. Reaction scheme of (1) 3NA electrochemical modification on MWCNTs, (2) nitro group electrochemical reduction to amino groups and (3) Cu(II) reduction.

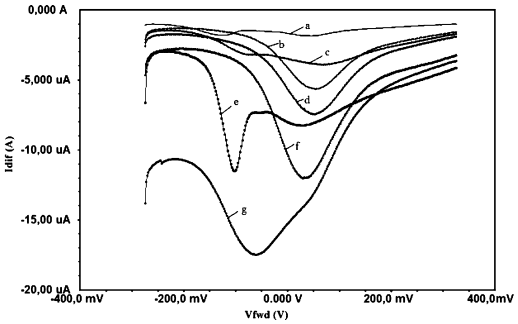

Fig. 2. Differential pulse voltammograms of copper at Bare GC (a); GC/3NA (b); GC/3NA(red) (c); GC/3NA/GO (d); GC/3NA(red)/GO (e); GC/GO/3NA (f); GC/GO/3NA(red) (g) electrodes recorded in BR buffer solution, pH 5.0 vs. Ag/AgCl/KCl_{sat}.

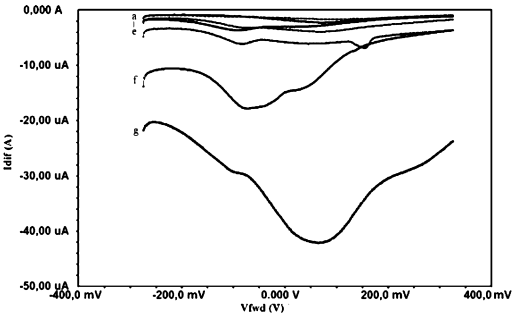

Fig. 3. Differential pulse voltammograms of copper at GC/NPs/3NA(red) electrodes: Bare GC (a); GC/3NA(red) (b); GC/Fe_2O_3/3NA(red) (c); GC/AuChts/3NA(red) (d); GC/Graphene/3NA(red) (e); GC/GO/3NA(red) (f); GC/MWCNTs/3NA(red) (g) recorded in BR buffer solution, pH 5.0 vs Ag/AgCl/KCl_{sat}.

showed that GC/GO/3NA(red) electrode is 5 times more sensitive compared to GC/3NA(red) electrode. The reason of this advanced sensitivity is related to larger electrochemically active surface, which has been increased by GO. Other researches also noticed some advantages of electrodes modified by carbon nanomaterials [44,45].

As it is understood from Fig. 2, the modification of GC by GO before electrochemical modification procedures enhances current responses compared with that of GC/3NA and GC/3NA(red)/ electrodes. Therefore, another step of this research was to determine nanomaterials which are the most efficient in electrochemical determination of Cu(II) ion. Five different nanomaterials were chosen for this aim: GO, graphene, Fe_3O_4, AuChts and MWCNTs and five different electrodes (GC/Fe_2O_3/3NA(red), GC/AuChts/3NA(red), GC/Graphene/3NA(red), GC/GO/3NA(red) and GC/MWCNTs/3NA(red)) were prepared for this part of research and their electrochemical responses towards Cu(II) ions were compared with bare GC and GC/3NA(red) electrodes.

DPV results (Fig. 3) showed that analytical signal registered by GC/MWCNTs/3NA(red) at +0.05 V electrode increases twice when compared with that registered with GC/GO/3NA(red). This effect is related to properties of MWCNTs. Since the MWCNTs can adsorb ions and molecules, exhibit strong adsorptive ability towards other species and increase their surface concentration [46]. In this way, it can provide large area for electrochemical modification by poly-3NA, which leads to significantly larger electrochemically active surface available for Cu(II) ion binding [47]. On the basis of above-mentioned factors Cu(II) ion binding efficiency on the GC/MWCNTs/3NA(red) electrode is much higher in comparison with that of electrodes, which are modified by the other nanomaterials used in this research. Therefore further experiments were carried using GC/MWCNTs/3NA(red) electrode.

The characteristics of the sensing systems such as selectivity, repeatability, reproducibility and stability are important as much as sensitivity. For this reason all further experiments were performed and the results were evaluated while applying statistical analysis. The investigation of sensitivity of the GC/MWCNTs/3NA(red) electrode towards binding of Cu(II) ions was carried out in the presence of other interfering metal ions (Zn(II), Cd(II), Pb(II), Mn(II), Co(II), Fe(III)). When other ions were presented at the same concentration as Cu(II) ions, their interfering effect decreased in following order: Co(II) > Mn(II) > Fe(III) > Cd(II) > Pb(II) > Zn(II). Here presented interfering metal ions at 1 mM concentration reduced the current peak from 14 to 37%. When all these metal ions at 1 mM concentrations were applied simultaneously and together with Cu(II) ions the interference towards Cu(II) ions determination increased up to 40%. Also no additional peaks were visible in related potential range, which would clearly indicate interfering effect. Takeuchi et al. have published research based on DPV results of Cu(II) detection, which are consistent with the results presented here. Addition of interfering metal ions reduces Cu(II) ion peak current and no other peaks have been observed in potential range between −0.3 V and +0.3 V. However in that research authors have also expanded the potential range and interfering metal peaks appeared outside −0.3 V and +0.3 V potential range [48]. In order to perform exact determination of interfering metals that are present in the sample together with Cu(II) ions it is essential to know the potentials of current peaks of interfering ions (Table 1).

During the investigation of the stability of GC/MWCNTs/3NA(red), electrode was kept at +4 °C temperature for 0, 1, 5 and 14 days in closed vessel with Ar gas and their sensitivity towards Cu(II) ions has been investigated using DPV. It has been noticed that the stability of analytical signal of electrode was decreasing gradually and after 5 days it became stable. After 14 days of incubation GC/MWCNTs/3NA(red) remained at 50% level of its' original electrochemical response towards Cu(II) ions (Fig. 4). In our previous research the stability of GC electrode modified with poly-4NA for Cu(II) ion determination has been analyzed within 4 days and

Table 1
Interference of various metal ions to DPV-based analytical signal of GC/MWCNTs/3NA electrode registered in BR buffer, pH 5.0 vs. Ag/AgCl/KClsat.

Ions	Concentration (mM)	DPV peak curent (μA)	Relative difference from 1 mM Cu^{2+}
Cu^{2+}	1	−42.12	0
All metals	1	−25.38	40%
Co^{2+}	1	−26.63	37%
Mn^{2+}	1	−27.71	34%
Fe^{3+}	1	−31.50	25%
Cd^{2+}	1	−33.60	20%
Pb^{2+}	1	−32.22	27%
Zn^{2+}	1	−36.13	14%

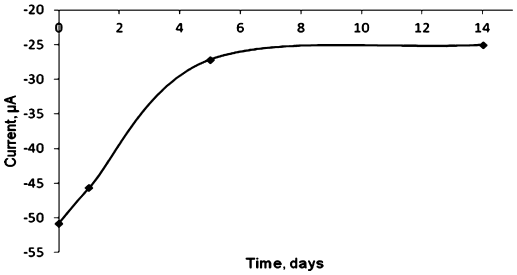

Fig. 4. Stability of DPV-based analytical signal of GC/MWCNTs/3NA(red) electrode in BR buffer solution, pH 5.0 vs. Ag/AgCl/KCl_{sat}.

the results of this test have demonstrated that analyzed electrode remained stable after mentioned period [28]. In other research by Fu et al. glassy carbon electrode, which was dedicated for copper determination, was modified with single-walled carbon nanotubes, gold nanoparticles and immobilized with L-cysteine self-assembled monolayers after 30 days still retained 82% of their initial analytical signal [49].

Compared to the electrodes analyzed in other researches, GC/MWCNTs/3NA(red) electrode showed relatively good storage stability, because after 5 days of incubation still 50% of initial analytical signal remains and later no decrease of analytical signal was observed, when the last stability test was performed after 14 days. Repeatability of differently modified electrodes in Cu(II) ion detection was tested using three similar electrodes prepared at same conditions. Relative standard variation (R.S.V.) of this test was 6.4%. R.S.V. of the reproducibility test was 1.4%. Between measurements for reproducibility electrode was regenerated using EDTA, which is known to be able to form complexes with heavy metals including Cu(II) ions. Zhuang et al. have analyzed the applicability of gold microelectrode for Cu(II) detection and their R.S.V. of reproducibility and repeatability is 5.1% and 3.2%, respectively [50]. In other research, which has been performed by Mohadesi et al., platinum electrode modified with overoxidized polypyrrole doped with Nitroso-R, which was applied for Cu(II) detection, their repeatability R.S.V. test results were in the range of 1.1–1.8% depending on Cu(II) concentration [51]. Another electrode, which has been analyzed for Cu(II) detection by Wang et al., was glassy carbon electrode modified with graphene and gold nanoparticles. R.S.V. for this electrode was calculated as 5.8% [42]. After the evaluation of repeatability and reproducibility results obtained by various electrodes applied in Cu(II) detection, which have been reported in some other researches and comparing them with the results of repeatability and reproducibility that were obtained in the frame of this article, it was determined that here reported GC/MWCNTs/3NA(red) electrode can compete in the determination of Cu(II) ions with other electrodes, which were reported to be suitable for Cu(II) determination [50,51].

Finally, only the GC/MWCNTs/3NA(red) electrode was evaluated for the limit of detection (LOD) value towards Cu(II) ions. The determination of Cu(II) ions was performed for three times and standard deviation values were calculated for all of the concentration values and for each differently modified electrode. Although the GC/MWCNTs/3NA(red) was the most sensitive (0.5×10^{-9} M) electrode for Cu(II) ions out of all electrodes, which were evaluated in this study, however it is still not the best sensitivity because the LOD value reported for the NTA/Reduced-P4NA/GC electrode was 0.5×10^{-12} M [28]. Another electrochemical Cu(II) ion sensor, which showed better sensitivity than our electrode, has been developed by Yang et al. and its detection limit was below 0.2×10^{-12} M. In this sensor analyte-recognizing element has been formed by a covalent attachment of the tripeptide Gly-Gly-His to self assembled monolayer of 3-mercaptopropionic acid formed on the gold electrode [52]. There are some more reports, which showed similar results with sensor presented in recent research, e.g.: Niu et al. have studied the electrochemical Cu(II) determination with a self-assembled monolayer of penicillamine formed on gold electrode that has limit of detection at 4.0×10^{-7} M [9]; Zeng et al. have reported the electrochemical determination of Cu(II) on gold electrode surface by stripping techniques with LOD at 1.0×10^{-10} M [53]; Betelu et al. have reported Cu(II) determination on 4–carboxyphenyl–grafted screen printed electrode with the limit of detection at 5.0×10^{-9} M by using square wave voltammetry [54]; Bai et al. have reported cysteine–modified mercury film electrode suitable for the Cu(II) determination at 5.0×10^{-10} M level by using stripping potentiometry [55].

4. Conclusions

In this research we have presented improved, low cost, easy fabrication, low-time consuming and sensitive method for Cu(II) by electrode based on MWCNTs deposited on GC electrode and then electrochemically modified with 3NA. The resulting GC/MWCNTs/3NA(red) electrode demonstrated that accurate determination of copper by DPV method is possible even in the presence of some interfering metal ions. Advanced analytical characteristics of here evaluated electrode shows great potential for the construction of electrochemical Cu(II) ion sensors and they open a new avenue for the development of sensing systems suitable for industrial application.

Disclaimer

This manuscript has not been published by other articles or simultaneously submitted to other articles for publishing.

Acknowledgement

This research has been partly supported by Selcuk University Research Foundation under the project number 12401014 and also European Union. Almira Ramanaviciene and Arunas Ramanavicius are grateful to European Community's social foundation under Grant Agreement No. VP1-3.1-ŠMM-08-K-01-004/KS-120000-1756. All other authors would like to thank Selcuk University Research Foundation and Short-Term Scientific Mission Program within the COST Action CM1101 and for their financial support.

References

[1] C. Horwitz, S.E. Van Der Linden, Cadmium and cobalt in tea and coffee and their relationship to cardiovascular disease, S.A. Med. J. 48 (1974) 230–233.
[2] L. Cui, J. Wu, J. Li, Y. Ge, H. Ju, Electrochemical detection of Cu^{2+} through Ag nanoparticle assembly regulated by copper-catalyzed oxidation of cysteamine, Biosens. Bioelectron. 55 (2014) 272–277.
[3] F. Li, J. Wang, Y. Lai, C. Wu, S. Sun, Y. He, H. Ma, Ultrasensitive and selective detection of copper (II) and mercury (II) ions by dye-coded silver nanoparticle-based SERS probes, Biosens. Bioelectron. 39 (2013) 82–87.
[4] S. Mahdavi, M. Jalali, A. Afkhami, Removal of heavy metals from aqueous solutions using Fe_3O_4, ZnO, and CuO nanoparticles, J. Nanopart. Res. 14 (2012) 1–18.
[5] Y.F. Shen, J. Tang, Z.H. Nie, Y.D. Wang, Y. Ren, L. Zuo, Preparation and application of magnetic Fe_3O_4 nanoparticles for wastewater purification, Sep. Purif. Technol. 68 (2009) 312–319.
[6] K. Kalantari, M.B. Ahmad, H.R.F. Masoumi, K. Shameli, M. Basri, R. Khandanlou, Rapid adsorption of heavy metals by Fe_3O_4/talc nanocomposite and optimization study using response surface methodology, Int. J. Mol. Sci. 15 (2014) 12913–12927.

[7] P.F. Hsu, W.L. Ciou, P.Y. Chen, Electrochemical determination of Cu(II) ions in chloride-rich environment using polyviologen-modified glassy carbon electrodes, J. Chin. Chem. Soc. 57 (2010) 244–251.
[8] Z. Wang, M. Wang, G. Wu, D. Wu, A. Wu, Colorimetric detection of copper and efficient removal of heavy metal ions from water by diamine-functionalized SBA-15, Dalton Trans. 43 (2014) 8461–8468.
[9] L.M. Niu, H.Q. Luo, N.B. Li, L. Song, Electrochemical detection of copper(II) at a gold electrode modified with a self-assembled monolayer of penicillamine, J. Anal. Chem. 62 (2007) 470–474.
[10] Z. Yao, B. Huang, X. Hu, L. Zhang, D. Li, M. Guo, X. Zhang, H. Yuan, H.C. Wu, Colorimetric detection of copper ions based on a supramolecular complex of water-soluble polythiophene and ATP, Analyst 138 (2013) 1649–1652.
[11] H. Vanhoe, C. Vandecasteele, J. Versieck, R. Dams, Determination of iron, cobalt, copper, zinc, rubidium, molybdenum, and cesium in human serum by inductively coupled plasma mass spectrometry, Anal. Chem. 61 (1989) 1851–1857.
[12] O.A. Culicov, M.V. Frontasyeva, E. Steinnes, O.S. Okina, Z. Santa, R. Todoran, Atmospheric deposition of heavy metals around the lead and copper-zinc smelters in Baia Mare Romania, studied by the moss biomonitoring technique, neutron activation analysis and flame atomic absorption spectrometry, J. Radioanal. Nucl. Chem. 254 (2002) 109–115.
[13] M. Lin, M. Cho, W.S. Choe, Y. Son, Y. Lee, Electrochemical detection of copper ion using a modified copolythiophene electrode, Electrochim. Acta 54 (2009) 7012–7017.
[14] M. Ghaedi, F. Ahmadi, A. Shokrollahi, Simultaneous preconcentration and determination of copper, nickel, cobalt and lead ions content by flame atomic absorption spectrometry, J. Hazard. Mater. 142 (2007) 272–278.
[15] M. Tüzen, Determination of heavy metals in fish samples of the middle Black Sea (Turkey) by graphite furnace atomic absorption spectrometry, Food Chem. 80 (2003) 119–123.
[16] J.S. Becker, M.V. Zoriy, C. Pickhardt, N. Palomero-Gallagher, K. Zilles, Imaging of copper, zinc, and other elements in thin section of human brain samples (hippocampus) by laser ablation inductively coupled plasma mass spectrometry, Anal. Chem. 77 (2005) 3208–3216.
[17] J. Otero-Romani, A. Moreda-Pineiro, P. Bermejo-Barrera, A. Martin-Esteban, Inductively coupled plasma-optical emission spectrometry/mass spectrometry for the determination of Cu, Ni, Pb and Zn in seawater after ionic imprinted polymer based solid phase extraction, Talanta 79 (2009) 723–729.
[18] M. Faraji, Y. Yamini, S. Shariati, Application of cotton as a solid phase extraction sorbent for on-line preconcentration of copper in water samples prior to inductively coupled plasma optical emission spectrometry determination, J. Hazard. Mater. 166 (2009) 1383–1388.
[19] O.W. Lau, S.Y. Ho, Simultaneous determination of traces of iron, cobalt, nickel, copper, mercury and lead in water by energy-dispersive X-ray fluorescence spectrometry after preconcentration as their piperazino-1,4-bis(dithiocarbamate) complexes, Anal. Chim. Acta 280 (1993) 269–277.
[20] L. Yang, R. McRae, M.M. Henary, R. Patel, B. Lai, S. Vogt, C.J. Fahrni, Imaging of the intracellular topography of copper with a fluorescent sensor and by synchrotron X-ray fluorescence microscopy, Proc. Natl. Acad. Sci. U. S. A. 102 (2005) 11179–11184.
[21] B.C. Yin, B.C. Ye, W. Tan, H. Wang, C.C. Xie, An allosteric dual-DNAzyme unimolecular probe for colorimetric detection of copper(II), J. Am. Chem. Soc. 131 (2009) 14624–14625.
[22] H. Zamzow, K.H. Coale, K.S. Johnson, C.M. Sakamoto, Determination of copper complexation in seawater using flow injection analysis with chemiluminescence detection, Anal. Chim. Acta 377 (1998) 133–144.
[23] Y.M. Liu, J.K. Cheng, Highly sensitive chemiluminescence detection of copper(II) in capillary electrophoresis with field-amplified sample injection, Electrophoresis 23 (2002) 556–558.
[24] H. Yin, Y. Zhou, X. Meng, T. Tang, S. Ai, L. Zhu, Electrochemical behaviour of Sudan I at Fe_3O_4 nanoparticles modified glassy carbon electrode and its determination in food samples, Food Chem. 127 (2011) 1348–1353.
[25] Y.J. Yang, L. Weikun, Simultaneous determination of catechol, hydroquinone, and resorcinol on CTAB functionalized graphene oxide/multiwalled carbon nanotube modified electrode, Fullerenes Nanotubes Carbon Nanostruct. 23 (2014) 410–417.
[26] H. Yin, Y. Zhou, Q. Ma, S. Ai, Q. Chen, L. Zhu, Electrocatalytic oxidation behavior of guanosine at graphene, chitosan and Fe_3O_4 nanoparticles modified glassy carbon electrode and its determination, Talanta 82 (2010) 1193–1199.
[27] E. Bilici, Z. Yazicigil, M. Tok, Y. Oztekin, Electrochemical determination of copper (II) using modified glassy carbon electrodes, Desalin. Water Treat. 50 (2012) 198–205.
[28] Y. Oztekin, M. Tok, H. Nalvuran, S. Kiyak, T. Gover, Z. Yazicigil, A. Ramanaviciene, A. Ramanavicius, Electrochemical modification of glassy carbon electrode by poly-4-nitroaniline and its application for determination of copper(II), Electrochim. Acta 56 (2010) 387–395.
[29] Y. Alvarez-Gallego, X. Dominguez-Benetton, D. Pant, L. Diels, K. Vanbroekhoven, I. Genné, P. Vermeiren, Development of gas diffusion electrodes for cogeneration of chemicals and electricity, Electrochim. Acta 82 (2012) 415–426.
[30] C.L. Yu, N.C. Lo, H. Cheng, T. Tsuda, T. Sakamoto, Y.H. Chen, S. Kuwabata, P.Y. Chen, An ionic liquid-Fe_3O_4 nanoparticles-graphite composite electrode used for nonenzymatic electrochemical determination of hydrogen peroxide, J. Electroanal. Chem. 729 (2014) 109–115.
[31] X. Zhang, D. Pant, F. Zhang, J. Liu, W. He, B.E. Logan, Long-term performance of chemically and physically modified activated carbons in air cathodes of microbial fuel cells, ChemElectroChem 1 (2014) 1859–1866.
[32] G. Aragay, J. Pons, A. Merkoci, Recent trends in macro-, micro-, and nanomaterial-based tools and strategies for heavy-metal detection, Chem. Rev. 111 (2011) 3433–3458.
[33] T. Alizadeh, M.R. Ganjali, M. Zare, Application of an Hg^{2+} selective imprinted polymer as a new modifying agent for the preparation of a novel highly selective and sensitive electrochemical sensor for the determination of ultratrace mercury ions, Anal. Chim. Acta 689 (2011) 52–59.
[34] L. Lin, J. Chen, H. Yao, Y. Chen, Y. Zheng, X. Lin, Simultaneous determination of dopamine, ascorbic acid and uric acid at poly (Evans Blue) modified glassy carbon electrode, Bioelectrochemistry 73 (2008) 11–17.
[35] X. Dai, R.G. Compton, Detection of As(III) via oxidation to As(V) using platinum nanoparticle modified glassy carbon electrodes: arsenic detection without interference from copper, Analyst 131 (2006) 516–521.
[36] D.C. Marcano, D.V. Kosynkin, J.M. Berlin, A. Sinitskii, Z. Sun, A. Slesarev, L.B. Alemany, W. Lu, J.M. Tour, Improved synthesis of graphene oxide, ACS Nano 4 (2010) 4806–4814.
[37] Y. Wang, D. Zhang, J. Wu, Electrocatalytic oxidation of kojic acid at a reduced graphene sheet modified glassy carbon electrode, J. Electroanal. Chem. 664 (2012) 111–116.
[38] Y. Yong, Y. Bai, Y. Li, L. Lin, Y. Cui, C. Xia, Preparation and application of polymer-grafted magnetic nanoparticles for lipase immobilization, J. Magn. Magn. Mater. 320 (2008) 2350–2355.
[39] H. Ciftci, U. Tamer, A.U. Metin, E. Alver, N. Kizir, Electrochemical copper (II) sensor based on chitosan covered gold nanoparticles, J. Appl. Electrochem. 44 (2014) 563–571.
[40] Y. Oztekin, Z. Yazicigil, A.O. Solak, Z. Ustundag, A. Okumus, Z. Kilic, A. Ramanaviciene, A. Ramanavicius, Phenanthroline derivatives electrochemically grafted to glassy carbon for Cu(II) ion detection, Sens. Actuators B: Chem. 166–167 (2012) 117–127.
[41] Y. Oztekin, M. Tok, E. Bilici, L. Mikoliunaite, Z. Yazicigil, A. Ramanaviciene, A. Ramanavicius, Copper nanoparticle modified carbon electrode for determination of dopamine, Electrochim. Acta 76 (2012) 201–207.
[42] S. Wang, Y. Wang, L. Zhou, J. Li, S. Wang, H. Liu, Fabrication of an effective electrochemical platform based on graphene and AuNPs for high sensitive detection of trace Cu^{2+}, Electrochim. Acta 132 (2014) 7–14.
[43] F. Gauthard, F. Epron, J. Barbier, Palladium and platinum-based catalysts in the catalytic reduction of nitrate in water: effect of copper, silver, or gold addition, J. Catal. 220 (2003) 182–191.
[44] S.G. Wang, Q. Zhang, R. Wang, S.F. Yoon, A novel multi-walled carbon nanotube-based biosensor for glucose detection, Biochem. Biophys. Res. Commun. 311 (2003) 572–576.
[45] Y. Zhang, P. He, N. Hu, Horseradish peroxidase immobilized in TiO_2 nanoparticle films on pyrolytic graphite electrodes: direct electrochemistry and bioelectrocatalysis, Electrochim. Acta 49 (2004) 1981–1988.
[46] F.H. Wu, G.C. Zhao, X.W. Wei, Electrocatalytic oxidation of nitric oxide at multi-walled carbon nanotubes modified electrode, Electrochem. Commun. 4 (2002) 690–694.
[47] K. Wu, S. Hu, J. Fei, W. Bai, Mercury-free simultaneous determination of cadmium and lead at a glassy carbon electrode modified with multi-wall carbon nanotubes, Anal. Chim. Acta 489 (2003) 215–221.
[48] R.M. Takeuchi, A.L. Santos, P.M. Padilha, N.R. Stradiotto, Copper determination in ethanol fuel by differential pulse anodic stripping voltammetry at a solid paraffin-based carbon paste electrode modified with 2-aminothiazole organofunctionalized silica, Talanta 71 (2007) 771–777.
[49] X.C. Fu, J. Wu, J. Li, C.G. Xie, Y.S. Liu, Y. Zhong, J.H. Liu, Electrochemical determination of trace copper(II) with enhanced sensitivity and selectivity by gold nanoparticle/single-wall carbon nanotube hybrids containing three-dimensional L-cysteine molecular adapters, Sens. Actuators B: Chem. 182 (2013) 382–389.
[50] J. Zhuang, L. Zhang, W. Lu, D. Shen, R. Zhu, D. Pan, Determination of trace copper in water samples by anodic stripping voltammetry at gold microelectrode, Int. J. Electrochem. Sci. 6 (2011) 4690–4699.
[51] A. Mohadesi, A. Salmanipour, S.Z. Mohammadi, A. Pourhatami, M.A. Taher, Stripping voltammetric determination of copper (II) on an overoxidized polypyrrole functionalized with Nitroso-R, J. Braz. Chem. Soc. 19 (2008) 956–962.
[52] W. Yang, D. Jaramillo, J.J. Gooding, D.B. Hibbert, R. Zhang, G.D. Willett, K.J. Fisher, Sub-ppt detection limits for copper ions with Gly-Gly-His modified electrodes, Chem. Commun. (2001) 1982–1983.
[53] B. Zeng, X. Ding, F. Zhao, Y. Yang, Electrochemical determination of copper(II) by gold electrodes modified with *N*-acetyl-L-cysteine, Anal. Lett. 35 (2002) 2245–2258.
[54] S. Betelu, C. Vautrin-Ul, A. Chaussé, Novel 4-carboxyphenyl-grafted screen-printed electrode for trace Cu(II) determination, Electrochem. Commun. 11 (2009) 383–386.
[55] Y. Bai, X. Ruan, J. Mo, Y. Xie, Potentiometric stripping analysis of copper using cysteine modified mercury film electrode, Anal. Chim. Acta 373 (1998) 39–46.

Paper 3

Surfaces functionalized by graphene oxide nanosheets for single cell investigations

L. Dedelaite, R.D. Rodriguez, E. Andriukonis, M. Hietschold, D.R. Zahn, A. Ramanavicius

Sensors and Actuators B: Chemical 255 (2018) 1735-1743

Sensors and Actuators B xxx (2017) xxx–xxx

Contents lists available at ScienceDirect

Sensors and Actuators B: Chemical

journal homepage: www.elsevier.com/locate/snb

Surfaces functionalized by graphene oxide nanosheets for single cell investigations

Lina Dedelaite [a], Raul D. Rodriguez [b,c,d,**], Eivydas Andriukonis [a,e], Michael Hietschold [f], Dietrich R.T. Zahn [c,d], Arunas Ramanavicius [a,*]

[a] Department of Physical Chemistry, Faculty of Chemistry and Geosciences, Vilnius University, Naugarduko 24, LT-03225 Vilnius, Lithuania
[b] Laser and Light Technology, Tomsk Polytechnic University, 30 Lenin Ave., 634050 Tomsk, Russia
[c] Semiconductor Physics, Chemnitz University of Technology, Reichenhainer Str. 70, 09126 Chemnitz, Germany
[d] Cluster of Excellence "Center for Advancing Electronics Dresden" Carbon Path, cfaed, Würzburger Str. 46, 01187 Dresden, Germany
[e] Laboratory of Nanotechnology, State Research Institute, Center for Physical Sciences and Technology, Savanoriu ave. 231, LT-02300 Vilnius, Lithuania
[f] Institute of Physics, Solid Surface Analysis, Technische Universität Chemnitz, Reichenhainer Str. 70, 09107 Chemnitz, Germany

ARTICLE INFO

Article history:
Received 20 May 2017
Received in revised form 15 August 2017
Accepted 26 August 2017
Available online xxx

Keywords:
Substrate modification
Graphene oxide
Raman spectroscopy
Cell immobilization
Yeast cell
Single cell

ABSTRACT

In this research development of sensor suitable for single cell investigation is reported. To achieve this goal biocompatible graphene oxide (GO) nanosheets were applied as substrates for separated cell immobilization. GO nanosheets are particularly interesting due to their biocompatibility, scalability, and possibility to be deposited *via* simple surface functionalization protocols. In this context, we rise the hypothesis that GO nanosheets can be used to treat substrates for single cell studies. We investigated this hypothesis using several pristine and GO-modified highly oriented pyrolytic graphite, objective glass slides, polished silicon wafers, polydimethylsiloxane and mica substrates. A significantly larger frequency of single cell deposition events was observed on all substrates modified by GO. We exploited the GO functionalization to advance the Raman spectroscopy based analysis of the chemical composition of individual cells gathering different Raman spectra with respect to that collected from yeast cell colonies.

1. Introduction

Cell imaging and investigation started immediately after the invention of optical microscopy, although mostly bulk samples containing high number of cells were analyzed. Recently the attention shifted towards the investigation and manipulation of single cells since it was understood that cells are individual microorganisms showing variations and distinct behavior with respect to that of the colony. It has been believed that the information obtained by analyzing large cell colonies is also representative for the behavior of individual cells. However, this is not always the case since individual cells can show different characteristics if they are separated from the cell colony. Most of the methods adapted to separate cells from a colony and to immobilize on an arbitrary surface, which is suitable for analytical purposes, demand sophisticated equipment and procedures. By exposing genetically identical cells to the same environmental conditions multiple variations in molecular content and even phenotype can be observed at the single cell level [1]. In the data obtained from bulk cell samples this phenotype-related information is averaged or even attributed to noise or statistical variations. In order to avoid this situation analysis at the single cell level is required. Analysis of single cells provides more realistic data about cell viability, aging, their biochemical properties, mutations, and many other characteristics. The demand to gather information from individual cells facilitates the development of novel methods for the immobilization of single cells on arbitrary substrates.

Nowadays there exist several most frequently used techniques for the separation and immobilization of single cells. One of the common ways to immobilize cells is based on the contact trapping method by exploiting the ability of cells to adhere naturally or artificially after treatment by various chemicals. This method involves the application of microwells [2], microchambers [3], cell

* Corresponding author at: Department of Physical Chemistry, Faculty of Chemistry and Geosciences, Vilnius University, Naugarduko 24, LT-03225 Vilnius, Lithuania.
** Corresponding author at: Laser and Light Technology, Tomsk Polytechnic University, 30 Lenin Ave., 634050 Tomsk, Russia.
E-mail addresses: raulmet@gmail.com (R.D. Rodriguez), arunas.ramanavicius@chf.vu.lt (A. Ramanavicius).

http://dx.doi.org/10.1016/j.snb.2017.08.187
0925-4005/

valve traps [4], or functionalized micro-pattered substrates [5,6]. The contact-based method is easy in application, inexpensive, does not require intricate devices or invasive techniques, moreover it allows high-throughput studies to be performed. However, using this technique there is a high chance to induce unknown phenotype variations. Therefore, it is very important to minimize these effects and optimal substrates with surfaces most suitable for cell-immobilization have to be selected carefully [7–9]. Beyond substrate engineering to investigate single cells, there are non-contact optical methods based on light trapping, the so-called optical tweezers. It is particularly interesting the case of laser tweezer Raman spectroscopy (LTRS) because it allows to manipulate single cells and simultaneously obtain the Raman spectra of cells interacting only with a liquid environment [10].

Budding yeasts cells (*Saccharomyces Cerevisiae*) serve as a bio-analytical target and model system to investigate single cells [11] and the mechanisms of their attachment on different substrates. Yeasts are simple single cell microorganisms, characterized by long shelf life, rapid growth, superior tolerance towards extreme pH, temperature, osmotic pressure, and ionic strength. Yeast cells are suitable for various manipulations, chemical treatment [12,13], electrochemical, and electromagnetic perturbations [14,15] and they are well growing in different media and are sticking to various surfaces. These criteria determined the application of yeast cells as one of the most extensively used eukaryotic models, which is often used for a better understanding of biological systems [16]. Yeast cell walls contains specialized surface proteins called 'adhesins' or 'flocculins' that are responsible for cell to cell and cell to surface adhesion. Cell adhesion is one of the most crucial ability that prevents cells from being washed away when a cell finds nourishing environment and allows forming biofilms with strong self-protection abilities [17]. These interactions include van der Waals, electrostatic, and hydrogen bonds [18] that create up to 25 mN averaged adhesion force per cell [19]. However not only proteins are known to form interactions with GO. The stacking π-π interaction between nucleotide bases of DNA can also be formed with the aromatic rings of graphene as shown in a previous report [20]. All these characteristics make yeast cells attractive and easy to analyse even immobilized on dry substrates in air at ambient conditions [21]. However, for better cell adhesion surface functionalization agents are required.

Graphene oxide (GO) is a two-dimensional (2D) material with a honeycomb carbon structure composed of relatively large sp^2 carbon domains surrounded by some sp^3 carbon domains and/or oxygen containing hydrophilic functional groups such as epoxide, hydroxyl, and carboxyl [22]. Due to its unique chemical structure, GO shows excellent processability in aqueous environments, applicability for surface engineering, suitability for surface-enhanced Raman scattering (SERS) and fluorescence quenching based technologies [23]. These properties attracted interest in using this material for biological studies and creation of advanced graphene-based nanomaterials [24,25]. Recently GO received even more attention due to its ability to self-exfoliate into single sheets by simple incubation in water making the production of GO films possible straight from a water-based solution. This is a considerable advantage over the modification by fullerenes that requires high temperatures or vapor deposition for fullerene-based film formation. Due to these characteristics GO can be combined with plastics or other materials that are sensitive to high temperature [26]. Moreover, the functional groups of GO can be reduced to graphene-like nanosheets by chemical [27] and/or electrochemical reduction [28], thermal reduction [29], 'green chemistry' based reduction by using reducing biological materials [30], or reduction by applying intense light pulses [31]. The conductivity of reduced GO (rGO) is increased but it is not as high as exfoliated graphene since rGO has a higher number of various defects in its structure and not all attached functional groups are removed. A significant number of sp^3 hybridization possessing groups and structures and increased number of lattice defects remains in rGO induced by oxidation of graphene to GO, which is followed by the GO reduction process. On the other hand, functional groups that were not reduced can remain as chemically active defect sites, which can be used for further chemical modification [27].

Vibrational spectroscopy offers non-invasive, non-destructive analysis of microorganisms. Raman spectroscopy is one of the most sensitive methods for obtaining chemical information and vastly used for biomedical research and materials science [32,33]. For biomolecules, such as proteins, lipids, carbohydrates, and nucleic acids, functional groups *e.g.*, C—C, C—H, and C=O stretching bonds as well as H—C—H bending bonds, can be detected as well-defined bands in the Raman spectra [34,35]. Usually the whole spectra of cells are presented as fingerprints of molecules and functional groups that can be used for microorganism identification and/or analysis of the chemical composition of their surface structures.

In this work, we aimed to demonstrate the possibility to use GO as a modification agent, which allows single cells to be immobilized on the surface of various arbitrary substrates. The simple modification of several substrates, namely glass, silicon, graphite, polydimethylsiloxane, and mica with graphene oxide is presented and their applicability for single cell immobilization is proven. The mechanism for cell adhesion on GO-modified surfaces is dominated by chemical interactions due to the presence of carboxylic and epoxy groups in the GO structure. The nature of adhesion phenomena is analyzed and a Raman spectroscopy based analysis of single cells immobilized on GO-modified substrates is performed.

2. Experimental

2.1. Materials

GO was purchased from ACS Materials (USA) dispersed in ethanol at a concentration of 5 g/L. The GO was chemically prepared by the Hummers method [36] with a flake size of about 0.5–5 μm. About 60% of the flakes have a thickness of one atomic layer. For surface modification with GO five different samples were chosen: objective glass slides from VWR, (USA), polished silicon wafers (100, p-type) from LG Siltron Inc. (South Korea), highly orientated pyrolytic graphite (HOPG) from NT-MDT (Moscow, Russia), polydimethylsiloxane (PDMS), and mica from Sigma Aldrich (Germany). Glass and silicon were cleaned sequentially in an ultrasonic bath in acetone, ethanol, and deionized ultra-pure water (Milli-Q) for 5 min in each solvent and then dried under nitrogen flow. HOPG and mica were cleaved with scotch tape right before cell deposition. PDMS was mixed by combining 10:1 mass equivalents of Silicone Elastomer (SYLGARD 184 silicone elastomer base) in a petri dish or container with cross-linker/curing agent (Dow Corning) for 5 min and kept inside a desiccator in vacuum for 4 h to remove air bubbles. The obtained substrate was cured by heating at 100 °C for one hour.

Yeast *Saccharomyces cerevisiae* cell strain Y00000 (BY4741 *Matα his3Δ1*; *leu2Δ0*; *met15Δ0*; *ura3Δ0*) was obtained from EUROSCARF (Frankfurt, Germany). The cells (3–4 μm size) were cultivated in solid agar yeast extract-agar media (1% yeast extract, 2% peptone, 2% glucose, 2% agar) plates in ambient atmosphere at 25 °C for 2 days and then stored at 4 °C. Cell cultures were renewed every 2 weeks. For Raman spectroscopy measurements only fresh yeast cell cultures were used. Some cells were grabbed with sterile loop and stirred in distilled water. A drop of the suspension was placed on the substrate and let dry at room temperature for 30 min before the Raman spectroscopy analysis was performed.

Please cite this article in press as: L. Dedelaite, et al., Surfaces functionalized by graphene oxide nanosheets for single cell investigations, Sens. Actuators B: Chem. (2017), http://dx.doi.org/10.1016/j.snb.2017.08.187

2.2. Procedures

The static contact angle measurements were carried out using an OCA-20 contact angle meter (Data Physics Instruments GmbH, Filderstadt, Germany) with the sessile drop method at room temperature and under air atmosphere. Deionized water (Millipore, 18.2 MΩ cm^{-1}) was applied for all contact angle measurements and for the preparation of all aqueous solutions.

The surface of glass, modified glass with GO and rGO substrates were imaged using atomic force microscopy (AFM). An OmegaScope SPM (AIST-NT, USA) was employed in contact mode with conventional silicon cantilevers.

Raman spectroscopy experiments were performed with a micro-Raman spectrometer LabRam HR800 (HORIBA, France) and XploRA (HORIBA, France). Two excitation laser lines were used: 514.7 nm solid state laser (Coherent, USA) and 532.0 nm. The laser intensity measured at the sample was set to 1 mW and 105 μW for the 514.7 nm and 532.0 nm, respectively. The laser light filtered by a plasma filter was focused onto the sample with a 100× objective (numerical aperture, N.A. = 0.9). The laser spot size obtained with the same objective is about 721 nm for the 532 nm wavelength. While all comparisons were made under the same conditions of laser wavelength and power, we resorted to use one or the other of the two Raman spectrometers according to the availability of the instrument. The scattered Raman signal was collected with the same objective in the backscattering geometry and detected by a charge coupled device (CCD) detector. Statistical averages were obtained from at least 5 spectra for an exposition time of 10 s each.

3. Results and discussion

3.1. Yeast cell solution drying observation

Five different materials: glass, silicon, HOPG, PDMS, and mica were chosen as substrates for further immobilization single cells. The substrates were freshly prepared before analysis and 3 μL of yeast cell in water solution was evenly deposited on the surface of the materials mentioned above. The drying process was observed in ambient conditions under a digital microscope Keyence VH-Z100 (USA) at 100× and 1000× magnification, the results are presented in Fig. 1. It was observed that on the pristine substrates, during water evaporation, the diameter of water droplets decreases depending on surface morphology defects. Cells that are immersed in the droplet due to water surface tension were swept across the surface and formed aggregates at the end of drying.

As can be seen from Fig. 1 intricate yeast cell agglomerates are formed on all substrates. GO was chosen for the modification of the mentioned substrates due to its unique chemical properties and biocompatibility [37]. A simple sample preparation method was used to obtain GO-based layers on glass substrates by the drop coating 5 μL on selected 10 mm^2 areas of the substrates and letting it dry in air. The layer of GO formed a slight brownish colored layer on the glass substrate as observed by simple visual inspection (Fig. S1). The drying process of the yeast cell suspension, which was prepared by dispersion of yeast cells in water-based solution and then drop coated on the modified with GO surfaces of all substrates, was observed through a digitalized microscope (videos, which are showing the process in real time, are included in the supporting information). The images of the cell suspension drying process are presented in Fig. 2. Unlike pristine substrates, the GO modified surfaces remarkably reduced the cell aggregation and increased the regions containing separated single cells. This is an indication of the enhanced cell adhesion on GO-based surfaces that is strong enough to withstand the water flow that was applied after deposition of yeast suspension on used substrates (before the drying process). Cell adhesion occurs in all substrates resulting in the formation of large agglomerates (see Fig. 1); however, this situation is drastically different for surfaces coated with GO where the cells distributing in singlets and small colonies (see Fig. 2) allow to perform analysis at the single cell level.

We investigated the mechanism behind such improved single cell addition and identified some most plausible reasons: 1) increased mechanical friction between cells and GO-modified surfaces due to larger roughness of GO films in comparison with pristine substrates, 2) changes in hydrophobicity of the substrates as determined by contact angle measurements, the increased hydrophobicity alters the drying process of the solvent, 3) increased electrostatic interaction between charged parts of yeast cell walls and carboxyl, carbonyl, and hydroxyl groups of GO, and 4) possible chemical interaction between carbonyl and hydroxyl groups of GO and the cell surface. In order to investigate these mechanisms in more detail we performed atomic force microscopy, contact

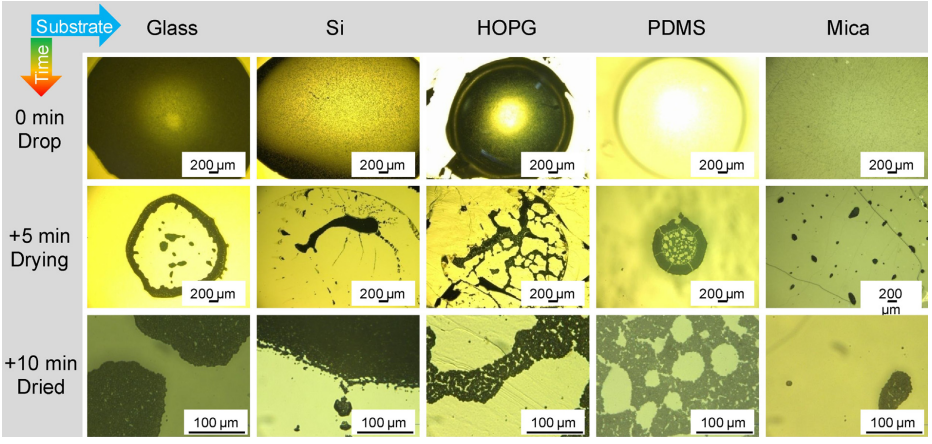

Fig. 1. Drying process of yeast cell suspension, which was prepared by dispersion of yeast cells in water and then drop coated on clean substrates such as: glass, silicon, HOPG, PDMS, and mica. Pictures were taken before and after water evaporation proceeded at ambient conditions over 5–10 min.

Please cite this article in press as: L. Dedelaite, et al., Surfaces functionalized by graphene oxide nanosheets for single cell investigations, Sens. Actuators B: Chem. (2017), http://dx.doi.org/10.1016/j.snb.2017.08.187

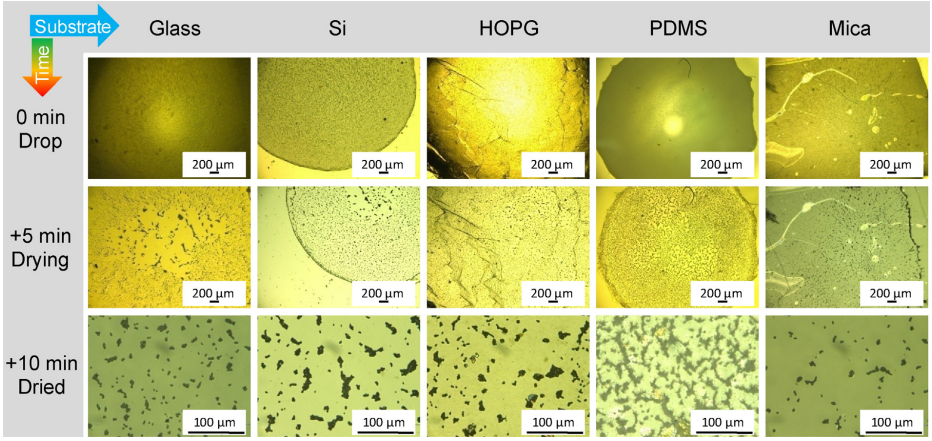

Fig. 2. Visualization of the drying process of yeast cell suspensions drop coated on the surfaces of GO modified substrates. Pictures were taken before and after water evaporation proceeded at ambient conditions over 5–10 min.

angle measurements, and studied a GO-coated surface after thermal reduction.

3.2. Increase in surface roughness

Theoretically there is a correlation between surface roughness and cell adhesion, which can be related to the interface energy. The surface roughness can increase or decrease the contact area between a cell and the substrate surface, which is proportional to the solid-liquid interfacial adhesive force [38]. Therefore, for surface roughness measurements contact mode AFM imaging was performed on pristine glass and glass coated with GO. Images of GO coated glass showed a heterogeneous surface with planar and wrinkled surface areas (Fig. S2b). The cross section of a graphene oxide nanosheet and surface proved that the thickness of GO is around (1.7 ± 0.1) nm, which is in the same order of the thickness of single layer 2D nanosheets. It should be noted that the thickness of pure graphene layer is 0.34 nm, and the GO thickness, due to the presence of functional groups, structural defects and adsorbed water molecules, increases up to 1 nm [39], and the

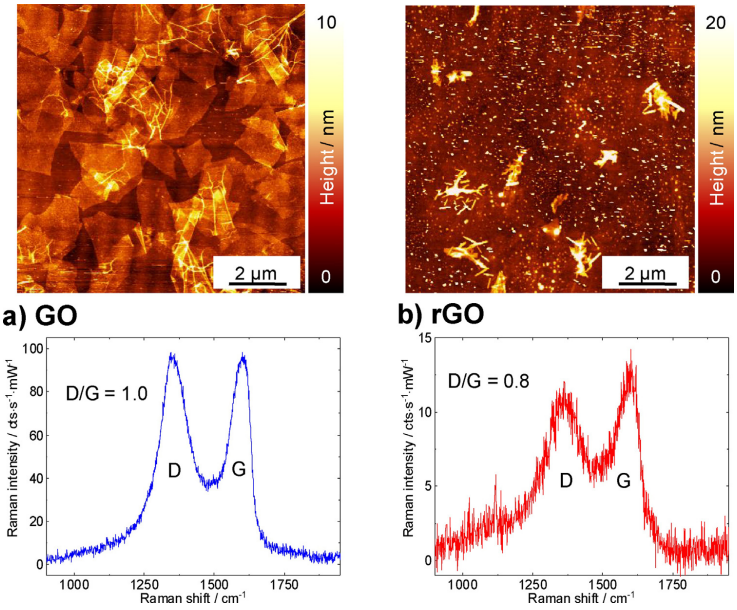

Fig. 3. AFM images and Raman spectra of a) graphene oxide and b) thermally reduced graphene oxide.

Please cite this article in press as: L. Dedelaite, et al., Surfaces functionalized by graphene oxide nanosheets for single cell investigations, Sens. Actuators B: Chem. (2017), http://dx.doi.org/10.1016/j.snb.2017.08.187

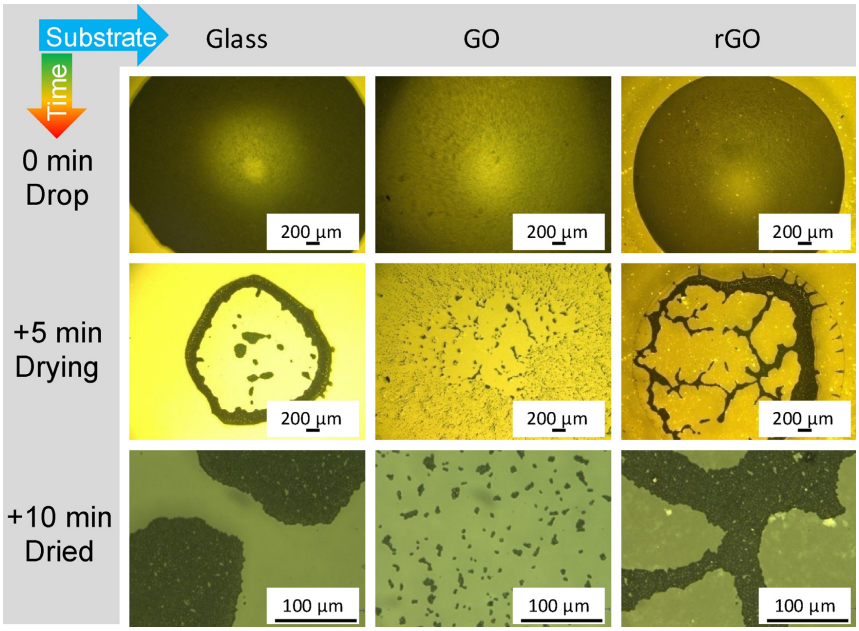

Fig. 4. Visualization of drying process of yeast cell suspension drop coated on GO- and rGO-modified substrates. Pictures were taken before and after water evaporation proceeded at ambient conditions over 5–10 min.

difference in tip-sample interaction between tip on glass and on GO can give rise to uncertainty in thickness. Even though, due to natural stacking into multiple layers and formation of wrinkles and folds the root mean square roughness increases up to (1.5 ± 0.2) nm compared to the clean glass surface with a roughness of (0.4 ± 0.2) nm. In comparison with the micrometer range cell size (*ca.* 4 µm), the nanometer roughness difference between reduced and pristine GO can be expected to be insignificant to mechanically immobilize cells. This is in contrast to a recent report by Mikoliunaite, Rodriguez, Sheremet, Kolchuzhin, Mehner, Ramanavicius and Zahn [40] where large submicrometer silver particles on the surface resulted in cell anchoring and efficient immobilization.

3.3. GO hydrophilicity

Graphene oxide is known to be a hydrophilic material due to the presence of oxygen groups on its basal plane and edges, hence we can expect that it changes the hydrophilic properties of the substrate that could be the origin of the difference in cell adhesion. For this reason, water contact angle measurements were performed in order to evaluate the change of surface hydrophilicity before and after modification with GO, the results are shown in Fig. S3. This analysis revealed that the layer of graphene oxide increases the substrate hydrophilicity by 14–69%, with the smallest change for the glass substrate and highest for PDMS. However, we cannot conclude that the surface hydrophilicity is the parameter that defines isolation of cells since GO-coated samples do not display a unique value but show different contact angles in the range of $12.6^\circ \pm 0.6^\circ$ to $41.3^\circ \pm 0.4^\circ$ (Fig. S3). These values also partly overlap with the contact angle of the surfaces before the GO modification. However, in the report of Kang and Choi [41] the adhesion of *S. cerevisiae* cells on surfaces coated with poly(styrene-ran-sulfonic acid) random copolymer (PS-*x*-SA) decreased while increasing surface hydrophilicity. This effect was not observed in our work.

3.4. Chemical functionality of GO

As already mentioned above, the yeast cell surface contains proteins that can create attractive interactions due to H-bonding, electrostatic interactions, including dipole-dipole interactions and van der Waals interactions, in contact with functional groups present at the substrate, in this case – the basal plane of GO. In order to test this assumption, we compared the aggregation of yeast cells on both GO and reduced GO, which contains a much lower concentration of functional groups on its surface. In order to covert GO into rGO a thermal reduction at 400 °C for 30 min was applied for the glass substrate, which was modified with GO. AFM images and Raman spectra before and after reduction of GO were taken under excitation by a 514.7 nm laser and are shown in Fig. 3.

The Raman spectra of GO and rGO presented in Fig. 3 show characteristic D and G bands, which arise from sp^2 and sp^3 vibrations, and some other peaks that arise due to defects in the carbon-based structure. In this study, both Raman bands were fitted using a total of 5 peaks (mixed Gaussian/Lorentzian fit) which are marked by D* (1201 cm^{-1}), D (1354 cm^{-1}), D" (1521 cm^{-1}), G (1592 cm^{-1}) and D' (1618 cm^{-1}) to allow differences in the spectra of GO and rGO to be tracked (Fig. S4). D* and D" after GO thermal reduction into rGO shift towards higher (1234 cm^{-1}) and lower (1492 cm^{-1}) wavelength numbers, respectively, which indicates the decrease of oxygen content [42]. G shift towards higher wave numbers (1601 cm^{-1}) can be explained due to amorphisation of the graphite structure. Additional D' peak rises from structural variety of the sample sp^2 hybridization [43]. Moreover, band marked as D" intensity decreases 10 times after reduction compared with its' intensity

Please cite this article in press as: L. Dedelaite, et al., Surfaces functionalized by graphene oxide nanosheets for single cell investigations, Sens. Actuators B: Chem. (2017), http://dx.doi.org/10.1016/j.snb.2017.08.187

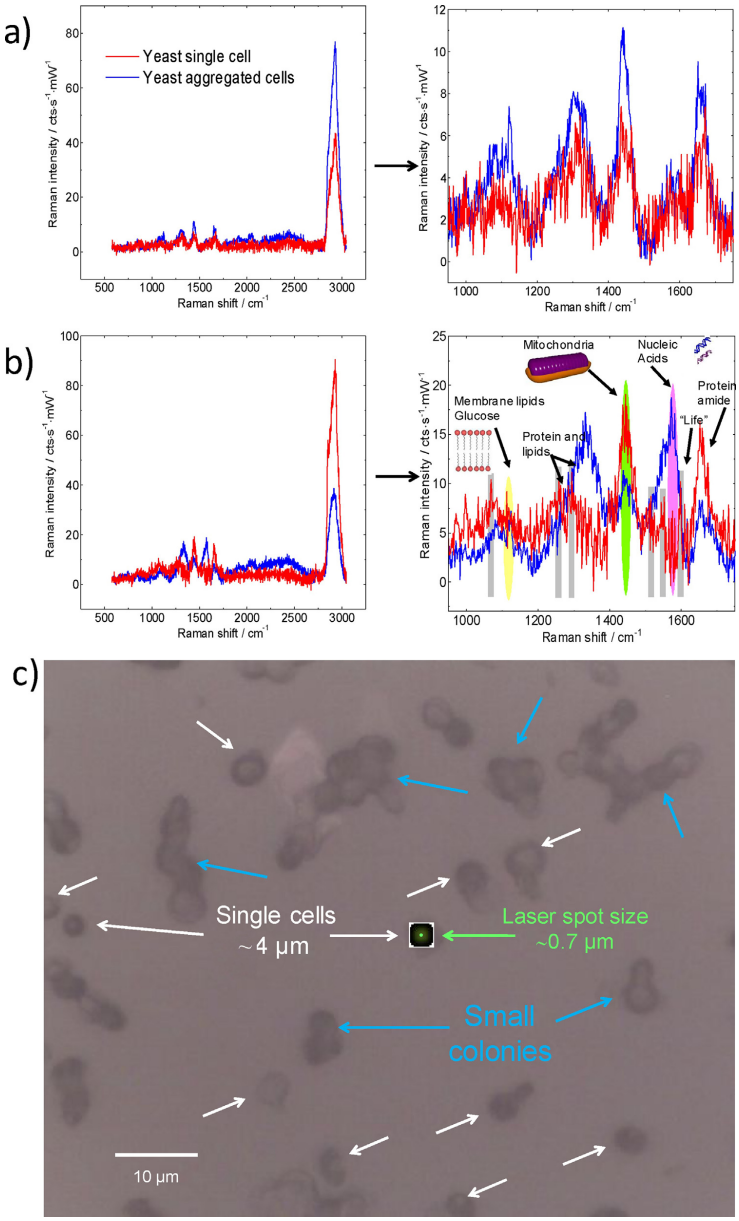

Fig. 5. Raman spectra of yeast cells immobilized on a) bare glass and b) GO-modified glass with part of spectra 'zoomed in' in the range from 950 cm^{-1} to 1750 cm^{-1}. Peaks that are visible only in the spectrum of a single yeast cell modified surface are marked by grey color. The baseline is corrected and the Raman signal of GO-modified glass was subtracted. c) Optical microscopy image obtained with the same optics used to record the Raman spectra. The different single cells and small colonies distribution on GO are shown, as well as the laser represented by the green dot. (For interpretation of the references to color in this figure legend, the reader is referred to the web version of this article.)

Please cite this article in press as: L. Dedelaite, et al., Surfaces functionalized by graphene oxide nanosheets for single cell investigations, Sens. Actuators B: Chem. (2017), http://dx.doi.org/10.1016/j.snb.2017.08.187

before the reduction. This band is related to amorphous phase since its intensity decreases with the increase of the crystallinity [42]. In addition to that, the intensity of these bands and the intensity ratio between D and G bands decreased after the thermal treatment in agreement with previous results [44]. The AFM image shows that GO nanosheets were significantly reduced during thermal annealing although some structural changes in the form of newly formed rods and particles were also observed. These results confirm that the reduction of GO was successful and that most of the functional groups were reduced.

Yeast cell adhesion on rGO-modified surfaces was tested. It was observed that on the rGO-modified surface, yeast cells behave the same way as on the pristine glass substrate not modified by GO (Fig. 4). Given that the roughness increased from 1.6 nm to 4.5 nm after the thermal reduction of GO was performed (as deduced from AFM), and that such increased roughness resulted in poorer cell adhesion, then we can conclude that the roughness effects are too small to play a significant role in our case. This observation comes intuitively considering that this roughness is way too small to act as a mechanical roadblock capable of anchoring the cells that have a size three orders of magnitude larger. These results on rGO thus provide essential evidence to support our hypothesis that the functional groups on GO are responsible for the stronger interaction between cell wall and GO-coated surfaces. This can be explained by chemical heterogeneities between the cell wall and the GO-modified surface, which creates localized sites where interaction energies at the interfacial area are higher making adhesion more efficient [41].

3.5. Evaluation of the Raman spectra of single yeast cells immobilized on GO-modified surfaces

All five GO-modified substrates (glass, Si, HOPG, PDMS, and mica) showed similar efficiency for yeast cell immobilization. However, for Raman spectroscopy investigations those substrates present intrinsic Raman features in the range from 700 cm^{-1} to 3000 cm^{-1}, which overlap with the Raman features from yeast cells. The only exception is the glass substrate that shows a rather flat spectrum in that fingerprint range, therefore, glass is the substrate we have chosen to perform the detailed Raman analysis presented below. Raman spectra of single and aggregated cells immobilized on glass and GO-modified glass surfaces were registered under 532.0 nm laser excitation. The average of 5 spectra from single cell and aggregates were registered, the results are presented in Fig. 5. In all four spectra the yeast cell characteristic peaks are visible. One of them is the high intensity, broad band at 2929 cm^{-1}, which is attributed to C—H stretch vibrations and is one of markers characteristic for organic matter [45]. The intensity of this peak indicates yeast cell thickness and can be attributed to its viability. The next peak is at 1654 cm^{-1}, which is attributed to C=C stretching mode, and the third one is at 1443 cm^{-1}, which is attributed to C—H deformation mode and is also called as 'mitochondria band' [46], that all are visible in the spectra presented in Fig. 5. They mark the ratio of unsaturated and saturated C—C bonds of fatty acids in lipids [47]. Another peak at 1572 cm^{-1}, which is also visible in all spectra [35] is attributed to nucleic acids (adenine and guanine). While comparing the yeast spectrum obtained for yeast cells immobilized on glass with that obtained for yeast cells immobilized on a GO-modified glass substrate it was observed that the GO-modification improves the Raman signals, because the intensity of the peaks in the range of 1000 cm^{-1} and 1750 cm^{-1} increased by 100%. This increase in intensity is likely due to the enhancing properties of GO-based layers as it was previously reported in applications of GO for surface-enhanced Raman scattering [48]. Moreover, these Raman spectra prove that the spectrum registered from a single cell modified surface provides more information than the one from surfaces modified by aggregated cells. No significant difference other than the peak intensity was observed in the spectra of single and aggregated yeast cells immobilized on pristine glass substrates. However, in the spectra registered from single and aggregated yeast cells immobilized on GO-modified glass substrates there are obvious differences in peak positions and intensities. In the spectrum of a single yeast cell immobilized on a GO-modified glass substrate the low intensity peaks at 1260 cm^{-1} and 1294 cm^{-1} are observed. These peaks are attributed to C—H deformation in proteins and lipids, although these peaks are absent in the spectrum registered from aggregated yeast cells. Therefore, the intensity of these vibrations is likely to be sensitive to the cell-cell interaction. This opens an exciting possibility to identify from the Raman spectra the cell-cell interaction affected by the presence of GO, for example, by comparing the spectra of optically trapped cells with that of cells immobilized on GO. The peaks at 1548 cm^{-1} and 1601 cm^{-1} are also visible only in the spectra registered from single cells. These peaks are attributed to nucleic acids and lipids, respectively [49]. Moreover, the peak at 1601 cm^{-1} reflects the respiratory activity of mitochondria and can be associated with cell viability [50]. From these results, we conclude that by analyzing single cells immobilized on GO-modified substrates in comparison to the analysis of large cell aggregates it is possible to gather additional information, which otherwise would be not noticed. Furthermore, an additional GO-modification amplifies the Raman signal registered from cells immobilized on molecular layers on mildly reduced GO in a similar way as it has been reported before [51]. Although the main Raman features discussed here are all observed above the noise level, we must notice that the spectra shown (like in Fig. 5) appear with a relatively low signal to noise ratio (s/n). We found that increasing the laser power in order to increase the spectral quality resulted in the irreversible modification of graphene oxide as shown in Fig. S5 in the supporting information. In order to increase the s/n one can also simply increase the acquisition time and the number of averaged spectra; however, this comes at the price of averaging out the non-stop changes ongoing in the cell, and that those changes could mask the small differences arising from the different environment around the cells (arising from the interaction with GO and other cells). Moreover, the dark spectrum obtained with the laser turned off shows a rather flat signal with an instrumental noise level well below the intensity of the Raman features from the cells. Therefore, considering these limitations in laser power and acquisition time, we compromised the s/n in order to make sure that the spectra obtained resulted from the pristine samples while keeping the s/n slightly above the noise level.

4. Conclusion

In this work, we demonstrated a simple and fast method for the deposition of single yeast cells on several arbitrary substrates functionalized with graphene oxide. Glass slides, PDMS, silicon, graphite, and mica substrates were investigated in parallel to show the generality of the method proposed here. After analyzing the cell immobilization mechanism, contributions from surface roughness and hydrophilicity were ruled out. We proved that single cell immobilization on GO-modified substrates is possible due to the presence of proteins on the cell surface, which bonds with epoxy, hydroxyl, and carboxyl functional groups of GO. These cell-surface interactions are strong enough to hold cells immobilized and well dispersed throughout the surface allowing the immobilization of single cells. Samples prepared in such way can be used for microscopic investigations at the single-cell level. The presence of graphene oxide on the substrate not only increases the density of isolated single cell events, but it also decreases the cell colony size as can be observed from Figs. 2 and 5c after drying. This opens the

Please cite this article in press as: L. Dedelaite, et al., Surfaces functionalized by graphene oxide nanosheets for single cell investigations, Sens. Actuators B: Chem. (2017), http://dx.doi.org/10.1016/j.snb.2017.08.187

possibility to investigate the effect of colony size on the cell properties. We expect that by changing the degree of graphene oxide reduction upon thermal annealing, the density of isolated single cells and colony size could be controlled.

Acknowledgement

We would like to express our gratitude for InProTUC project which allowed this research collaboration to happen. We thank Lina Mikoliunaite for her contribution in the start of this research. We would also like to thank Andrey Krayev from AIST-NT for providing the original GO dispersion and Clemens Göhler for the help with water contact angle measurements. We would also like to thank Akash Verma, Harsha Vijay Shah, and Alexander A. Golubev for the help with processing Raman and AFM data. We acknowledge funding by the German Science Foundation DFG Research Unit SMINT FOR1317, the Cluster of Excellence "Center for Advancing Electronics Dresden" (cfaed). This work was performed in the context of the European COST Action MP1302 Nanospectroscopy. The research was partially supported by Tomsk Polytechnic University Competitiveness Enhancement Program grant, Project Number TPU CEP_IHTP_73\2017. The research was partly supported (Arunas Ramanavicius, Eivydas Andriukonis and Lina Dedelaite) by Lithuanian Research Council project number SEN – 21/2015.

Appendix A. Supplementary data

Supplementary data associated with this article can be found, in the online version, at http://dx.doi.org/10.1016/j.snb.2017.08.187.

References

[1] A. Amantonico, J.Y. Oh, J. Sobek, M. Heinemann, R. Zenobi, Mass spectrometric method for analyzing metabolites in yeast with single cell sensitivity, Angew. Chem. Int. Ed. 47 (2008) 5382–5385.
[2] S. Lindström, H. Andersson-Svahn, Miniaturization of biological assays—overview on microwell devices for single-cell analyses, Biochim. Biophys. Acta 1810 (2011) 308–316.
[3] K.R. Love, V. Panagiotou, B. Jiang, T.A. Stadheim, J.C. Love, Integrated single-cell analysis shows Pichia pastoris secretes protein stochastically, Biotechnol. Bioeng. 106 (2010) 319–325.
[4] B. Sankaran, M. Racic, A. Tona, M.V. Rao, M. Gaitan, S.P. Forry, Dielectrophoretic capture of mammalian cells using transparent indium tin oxide electrodes in microfluidic systems, Electrophoresis 29 (2008) 5047–5054.
[5] Q. Cheng, K. Komvopoulos, S. Li, Surface chemical patterning for long-term single-cell culture, J. Biomed. Mater. Res. A 96 (2011) 507–512.
[6] D. Falconnet, G. Csucs, H.M. Grandin, M. Textor, Surface engineering approaches to micropattern surfaces for cell-based assays, Biomaterials 27 (2006) 3044–3063.
[7] F.S. Fritzsch, C. Dusny, O. Frick, A. Schmid, Single-cell analysis in biotechnology, systems biology, and biocatalysis, Annu. Rev. Chem. Biomol. Eng. 3 (2012) 129–155.
[8] A. Suchodolskis, V. Feiza, A. Stirke, A. Timonina, A. Ramanaviciene, A. Ramanavicius, Elastic properties of chemically modified baker's yeast cells studied by AFM, Surf. Interface Anal. 43 (2011) 1636–1640.
[9] A. Suchodolskis, A. Stirke, A. Timonina, A. Ramanaviciene, A. Ramanavicius, Baker's yeast transformation studies by Atomic Force Microscopy, Adv. Sci. Lett. 4 (2011) 171–173.
[10] C. Xie, M.A. Dinno, Y.-q. Li, Near-infrared Raman spectroscopy of single optically trapped biological cells, Opt. Lett. 27 (2002) 249–251.
[11] A. Ramanavicius, I. Morkvenaite-Vilkonciene, A. Kisieliute, J. Petroniene, A. Ramanaviciene, Scanning electrochemical microscopy based evaluation of influence of pH on bioelectrochemical activity of yeast cells-Saccharomyces cerevisiae, Colloids Surf. B: Biointerfaces 149 (2017) 1–6.
[12] A. Ramanavicius, E. Andriukonis, A. Stirke, L. Mikoliunaite, Z. Balevicius, A. Ramanaviciene, Synthesis of polypyrrole within the cell wall of yeast by redox-cycling of [Fe(CN)6]3-/[Fe(CN)6]4-, Enzyme Microb. Technol. 83 (2016) 40–47.
[13] I. Morkvenaite-Vilkonciene, A. Ramanaviciene, A. Ramanavicius, 9,10-Phenanthrenequinone as a redox mediator for the imaging of yeast cells by scanning electrochemical microscopy, Sens. Actuators B: Chem. 228 (2016) 200–206.
[14] A. Stirke, A. Zimkus, S. Balevicius, V. Stankevic, A. Ramanaviciene, A. Ramanavicius, N. Zurauskiene, Permeabilization of yeast Saccharomyces cerevisiae cell walls using nanosecond high power electrical pulses, Appl. Phys. Lett. 105 (2014) 253701.
[15] A. Stirke, A. Zimkus, A. Ramanaviciene, S. Balevicius, N. Zurauskiene, G. Saulis, L. Chaustova, V. Stankevic, A. Ramanavicius, Electric field-induced effects on yeast cell wall permeabilization, Bioelectromagnetics 35 (2014) 136–144.
[16] K. Baronian, The use of yeast and moulds as sensing elements in biosensors, Biosens. Bioelectron. 19 (2004) 953–962.
[17] K.J. Verstrepen, F.M. Klis, Flocculation, adhesion and biofilm formation in yeasts, Mol. Microbiol. 60 (2006) 5–15.
[18] C. Nune, W. Xu, R. Misra, The impact of grafted modification of silicone surfaces with quantum-sized materials on protein adsorption and bacterial adhesion, J. Biomed. Mater. Res. A 100 (2012) 3197–3204.
[19] Y. Shen, M.R. Ahmad, M. Nakajima, S. Kojima, M. Homma, T. Fukuda, Evaluation of the single yeast cell's adhesion to ITO substrates with various surface energies via ESEM nanorobotic manipulation system, IEEE Trans. Nanobiosci. 10 (2011) 217–224.
[20] M. Stobiecka, B. Dworakowska, S. Jakiela, A. Lukasiak, A. Chalupa, K. Zembrzycki, Sensing of survivin mRNA in malignant astrocytes using graphene oxide nanocarrier-supported oligonucleotide molecular beacons, Sens. Actuators B: Chem. 235 (2016) 136–145.
[21] L. Mikoliunaite, A. Makaraviciute, A. Suchodolskis, A. Ramanaviciene, Y. Oztekin, A. Stirke, G. Jurkaite, M. Ukanis, G. Carac, P. Cojocaru, Atomic force microscopy study of living Baker's yeast cells, Adv. Sci. Lett. 4 (2011) 368–376.
[22] D.R. Dreyer, S. Park, C.W. Bielawski, R.S. Ruoff, The chemistry of graphene oxide, Chem. Soc. Rev. 39 (2010) 228–240.
[23] C. Chung, Y.-K. Kim, D. Shin, S.-R. Ryoo, B.H. Hong, D.-H. Min, Biomedical applications of graphene and graphene oxide, Acc. Chem. Res. 46 (2013) 2211–2224.
[24] Y. Wang, Z. Li, J. Wang, J. Li, Y. Lin, Graphene and graphene oxide: biofunctionalization and applications in biotechnology, Trends Biotechnol. 29 (2011) 205–212.
[25] S.H. Yang, T. Lee, E. Seo, E.H. Ko, I.S. Choi, B.S. Kim, Interfacing living yeast cells with graphene oxide nanosheaths, Macromol. Biosci. 12 (2012) 61–66.
[26] J.T. Robinson, F.K. Perkins, E.S. Snow, Z. Wei, P.E. Sheehan, Reduced graphene oxide molecular sensors, Nano Lett. 8 (2008) 3137–3140.
[27] C.K. Chua, M. Pumera, Chemical reduction of graphene oxide: a synthetic chemistry viewpoint, Chem. Soc. Rev. 43 (2014) 291–312.
[28] J. Kauppila, P. Kunnas, P. Damlin, A. Viinikanoja, C. Kvarnström, Electrochemical reduction of graphene oxide films in aqueous and organic solutions, Electrochim. Acta 89 (2013) 84–89.
[29] X. Gao, J. Jang, S. Nagase, Hydrazine and thermal reduction of graphene oxide: reaction mechanisms, product structures, and reaction design, J. Phys. Chem. C 114 (2009) 832–842.
[30] P. Khanra, T. Kuila, N.H. Kim, S.H. Bae, D.-s. Yu, J.H. Lee, Simultaneous bio-functionalization and reduction of graphene oxide by baker's yeast, Chem. Eng. J. 183 (2012) 526–533.
[31] A. Al-Hamry, H. Kang, E. Sowade, V. Dzhagan, R. Rodriguez, C. Müller, D. Zahn, R. Baumann, O. Kanoun, Tuning the reduction and conductivity of solution-processed graphene oxide by intense pulsed light, Carbon 102 (2016) 236–244.
[32] A. Downes, A. Elfick, Raman spectroscopy and related techniques in biomedicine, Sensors 10 (2010) 1871–1889.
[33] K.A. Antonio, Z.D. Schultz, Advances in biomedical raman microscopy, Anal. Chem. 86 (2013) 30–46.
[34] S.B. Rodriguez, M.A. Thornton, R.J. Thornton, Raman spectroscopy and chemometrics for identification and strain discrimination of the wine spoilage yeasts Saccharomyces cerevisiae, Zygosaccharomyces bailii, and Brettanomyces bruxellensis, Appl. Environ. Microbiol. 79 (2013) 6264–6270.
[35] I. Notingher, Raman spectroscopy cell-based biosensors, Sensors 7 (2007) 1343–1358.
[36] N. Cao, Y. Zhang, Study of reduced graphene oxide preparation by Hummers' method and related characterization, J. Nanomater. 2015 (2015) 2.
[37] S. Nagarajan, C. Pochat-Bohatier, C. Teyssier, S. Balme, P. Miele, N. Kalkura, V. Cavailles, M. Bechelany, Design of graphene oxide/gelatin electrospun nanocomposite fibers for tissue engineering applications, RSC Adv. 6 (2016) 109150–109156.
[38] Y. Fan, F. Cui, S. Hou, Q. Xu, L. Chen, I.-S. Lee, Culture of neural cells on silicon wafers with nano-scale surface topograph, J. Neurosci. Methods 120 (2002) 17–23.
[39] M.J. McAllister, J.-L. Li, D.H. Adamson, H.C. Schniepp, A.A. Abdala, J. Liu, M. Herrera-Alonso, D.L. Milius, R. Car, R.K. Prud'homme, Single sheet functionalized graphene by oxidation and thermal expansion of graphite, Chem. Mater. 19 (2007) 4396–4404.
[40] L. Mikoliunaite, R.D. Rodriguez, E. Sheremet, V. Kolchuzhin, J. Mehner, A. Ramanavicius, D.R. Zahn, The substrate matters in the Raman spectroscopy analysis of cells, Sci. Rep. 5 (2015).
[41] S. Kang, H. Choi, Effect of surface hydrophobicity on the adhesion of S. cerevisiae onto modified surfaces by poly (styrene-ran-sulfonic acid) random copolymers, Colloids Surf. B: Biointerfaces 46 (2005) 70–77.
[42] S. Claramunt, A. Varea, D. Lopez-Díaz, M.M. Velázquez, A. Cornet, A. Cirera, The importance of interbands on the interpretation of the Raman spectrum of graphene oxide, J. Phys. Chem. C 119 (2015) 10123–10129.
[43] M. Mowry, D. Palaniuk, C.C. Luhrs, S. Osswald, In situ Raman spectroscopy and thermal analysis of the formation of nitrogen-doped graphene from urea and graphite oxide, RSC Adv. 3 (2013) 21763–21775.

Please cite this article in press as: L. Dedelaite, et al., Surfaces functionalized by graphene oxide nanosheets for single cell investigations, Sens. Actuators B: Chem. (2017), http://dx.doi.org/10.1016/j.snb.2017.08.187

[44] S. Stankovich, D.A. Dikin, R.D. Piner, K.A. Kohlhaas, A. Kleinhammes, Y. Jia, Y. Wu, S.T. Nguyen, R.S. Ruoff, Synthesis of graphene-based nanosheets via chemical reduction of exfoliated graphite oxide, Carbon 45 (2007) 1558–1565.
[45] P. Rösch, M. Harz, M. Schmitt, J. Popp, Raman spectroscopic identification of single yeast cells, J. Raman Spectrosc. 36 (2005) 377–379.
[46] J. Ring, C. Sommer, D. Carmona-Gutierrez, C. Ruckenstuhl, T. Eisenberg, F. Madeo, The metabolism beyond programmed cell death in yeast, Exp. Cell Res. 318 (2012) 1193–1200.
[47] O. Samek, A. Jonáš, Z. Pilát, P. Zemánek, L. Nedbal, J. Tříska, P. Kotas, M. Trtílek, Raman microspectroscopy of individual algal cells: sensing unsaturation of storage lipids in vivo, Sensors 10 (2010) 8635–8651.
[48] H. Yang, H. Hu, Z. Ni, C.K. Poh, C. Cong, J. Lin, T. Yu, Comparison of surface-enhanced Raman scattering on graphene oxide, reduced graphene oxide and graphene surfaces, Carbon 62 (2013) 422–429.
[49] Y.-S. Huang, T. Karashima, M. Yamamoto, H.o. Hamaguchi, Molecular-level investigation of the structure, transformation, and bioactivity of single living fission yeast cells by time-and space-resolved Raman spectroscopy, Biochemistry 44 (2005) 10009–10019.
[50] L.d. Chiu, M. Ando, H.o. Hamaguchi, Study of the 'Raman spectroscopic signature of life'in mitochondria isolated from budding yeast, J. Raman Spectrosc. 41 (2010) 2–3.
[51] X. Yu, H. Cai, W. Zhang, X. Li, N. Pan, Y. Luo, X. Wang, J. Hou, Tuning chemical enhancement of SERS by controlling the chemical reduction of graphene oxide nanosheets, ACS Nano 5 (2011) 952–958.

Biographies

PhD Lina Dedelaite is from Vilnius, Lithuania. She received her BS and MS degree in Chemistry from Vilnius University in 2011 and 2013 respectively. There she is continuing to study physical chemistry as a PhD student. During the studies, she did several scientific researches abroad, one of them was in Selcuk University in Konya, Turkey and other ones were in Technical University of Chemnitz in Chemnitz, Germany where she got interested in Raman spectroscopy. Her scientific interest focuses on developing SERS substrates, analysis and applications.

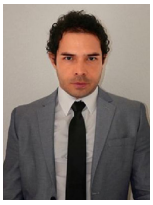

Prof. Dr. Raul D. Rodriguez received a Ph.D. in Physics and Chemistry of Nanomaterials in 2009 with the highest honors at the Institut des NanoSciences de Paris. Pierre et Marie Curie University (Sorbonne Universités) Paris, France. From 2011, he established the TERS Team in Chemnitz, Germany, developing novel methods for nanoscale characterization along with the direct supervision of over 30 graduate students. He is now a full professor at Tomsk Polytechnic University, Tomsk, Russia. Prof. Rodriguez is a co-editor and author of the Textbook on Optical Nanospectroscopy, as part of his active and leading role in the EU COST Action MP1302. In an active synergy between research and education, his group has been awarded 7 awards in international conferences. He is an active reviewer of a dozen high impact factor journals. Prof. Rodriguez research focuses on developing novel methods for nanoscale characterization, and the study and implementation of novel nanomaterials for technological developments from biomedicine and optoelectronics to energy and safety applications.

Eivydas Andriukonis PhD student chemistry at Vilnius University, Vilnius, Lithuania. In 2017 he received his master degree of biochemistry also from Vilnius University. During studies he worked on polymer polypyrrole synthesis catalysed by yeast cells to achieve cell wall structure modification. As a student he resulted in writing his first scientific paper back in 2016 (Synthesis of polypyrrole within the cell wall of yeast by redox-cycling of $[Fe(CN)_6]^{3-}$/$[Fe(CN)_6]^{4-}$). Further on expanded his qualification on working with stable isotope technologies, their application in ecology, metabolism studies and in polymer studies. As result at the end of master studies he published second paper "Kinetic 15N-isotope effects on algal growth".

Prof. Dr. Michael Hietschold studied physics and completed Ph.D. 1976 in theoretical solid state physics at Technical University Dresden, Germany. He was a postdoc at Quantum Theory Group of Moscow State Lomonosov University, Soviet Union. Since 1993, he was a professor for Solid Surfaces Analysis and head of the Electron Microscopy Laboratory at the Institute of Physics, Technische Universität Chemnitz, Germany. His research interests are surface physics, nanophysics and ultramicroscopy. He was a guest professor at the National University Ho Chi Minh City, Vietnam, and also lecturing at Portland State University, Oregon, USA. Since 2008 he is advisor for the National Metals and Materials Technology Center (MTEC), Pathumthani, Thailand. Michael Hietschold is a referee for many international scientific journals and funding organizations and has published about 250 scientific papers. He got retired in 2016 but is still actively interested in science.

Prof. Dr. Dr. h.c. Dietrich RT Zahn (born 1958) studied Physics at RWTH Aachen and received a PhD degree in 1988 from the University of Wales in Cardiff. After a post-doc period at the TU Berlin he became Professor for Semiconductor Physics at the Technische Universität Chemnitz in 1993. His research interests focus on the spectroscopic characterisation of semiconductor surfaces, interfaces, ultra-thin films, and low-dimensional structures (>800 publications, h-index 40). He served as Pro-rector for Research at the Technische Universität Chemnitz and as Head of the Thin Film Division of the German Physical Society (DFG). Currently he is Speaker of the DFG Research Unit FOR 1154 "Towards Molecular Spintronics" and the DFG Research Unit FOR 1713 "Sensorical Micro and Nano Systems". He is member of the excellence clusters "MERGE" and "cfaed". Prof. Zahn is Vice-president of the German Vacuum Society (DVG).

Prof. Habil. Dr. Arunas Ramanavicius is a professor at Vilnius University, Vilnius, Lithuania. He is a head of Department of Physical Chemistry at Vilnius University and NanoTechnas – Centre of Nanotechnology and Materials Science. He is also leading the department of NanoBioTechnology at Research Center of Physical Sciences and Technologies. Prof. Arunas Ramanavicius is a member of Lithuanian Academy of sciences. In 1998 he received PhD degree and in 2002 doctor habilitus degree from Vilnius University. Prof. A. Ramanavicius is serving as expert-evaluator in EU-FP7 program coordinated by European Commission and he is technical advisor of many foundations located in European and non-European countries. He has research interests in various aspects of nanotechnology, bionanotechnology, nanomaterials, biosensorics, bioelectronics, biofuel cells and MEMS based analytical devices. He is a national coordinator of several nanotechnology related COST actions.

Please cite this article in press as: L. Dedelaite, et al., Surfaces functionalized by graphene oxide nanosheets for single cell investigations, Sens. Actuators B: Chem. (2017), http://dx.doi.org/10.1016/j.snb.2017.08.187

Paper 4

Large-scale self-organized gold nanostructureswith bidirectional plasmon resonances for SERS

B. Schreiber, D. Gkogkou, L. Dedelaite, J. Kerbusch, R. Hubner, E. Sheremet, D.R.T. Zahn, A. Ramanavicius, S. Facsko, R.D. Rodriguez

RSC Advances 8 (2018) 22569-22576

RSC Advances

PAPER

View Article Online
View Journal | View Issue

Cite this: *RSC Adv.*, 2018, **8**, 22569

Large-scale self-organized gold nanostructures with bidirectional plasmon resonances for SERS†

Benjamin Schreiber,[*ab] Dimitra Gkogkou,[c] Lina Dedelaite,[de] Jochen Kerbusch,[a] René Hübner,[a] Evgeniya Sheremet,[f] Dietrich R. T. Zahn,[e] Arunas Ramanavicius,[d] Stefan Facsko[a] and Raul D. Rodriguez[*ef]

Efficient substrates for surface-enhanced Raman spectroscopy (SERS) are under constant development, since time-consuming and costly fabrication routines are often an issue for high-throughput spectroscopy applications. In this research, we use a two-step fabrication method to produce self-organized parallel-oriented plasmonic gold nanostructures. The fabrication routine is ready for wafer-scale production involving only low-energy ion beam irradiation and metal deposition. The optical spectroscopy features of the resulting structures show a successful bidirectional plasmonic response. The localized surface plasmon resonances (LSPRs) of each direction are independent from each other and can be tuned by the fabrication parameters. This ability to tune the LSPR characteristics allows the development of optimized plasmonic nanostructures to match different laser excitations and optical transitions for any arbitrary analyte. Moreover, in this study, we probe the polarization and wavelength dependence of such bidirectional plasmonic nanostructures by a complementary spectroscopic ellipsometry and Raman spectroscopy analysis. We observe a significant signal amplification by the SERS substrates and determine enhancement factors of over a thousand times. We also perform finite element method-based calculations of the electromagnetic enhancement for the SERS signal provided by the plasmonic nanostructures. The calculations are based on realistic models constructed using the same particle sizes and shapes experimentally determined by scanning electron microscopy. The spatial distribution of electric field enhancement shows some dispersion in the LSPR, which is a direct consequence of the semi-random distribution of hotspots. The signal enhancement is highly efficient, making our SERS substrates attractive candidates for high-throughput chemical sensing applications in which directionality, chemical stability, and large-scale fabrication are essential requirements.

Received 11th May 2018
Accepted 12th June 2018

DOI: 10.1039/c8ra04031a

rsc.li/rsc-advances

1 Introduction

Raman spectroscopy is a well-established method in a wide-field of chemical sensing applications.[1] For the detection of low concentration of molecules, Raman spectroscopy (RS) reaches its limit, because of the rather low Raman scattering cross-section of most samples. The most efficient approach to overcome this problem is the application of surface-enhanced Raman spectroscopy (SERS).[2] SERS exploits the strong electromagnetic amplifying properties of plasmonic nanostructures. Particularly interesting are plasmonic surfaces with more than one localized plasmon resonance (LSPR) that provide a broad range of applicability.[3] With such nanostructures, it is possible to employ simultaneously complementary vibrational spectroscopy methods ranging from SERS, surface-enhanced resonant Raman spectroscopy (SERRS), and surface-enhanced infrared absorption using the same sample.[4] However, the applicability of this kind of samples is undermined by the fabrication complexity that involves multiple steps and lithography processes.

Self-assembled SERS systems with bidirectionally excitable LSPRs offer a strategy to overcome this limitation. SERS substrates with bidirectionally excitable LSPRs supporting spectrally separated LSPRs which can be selectively triggered by polarization of the used light source. This allows broadband excitable SERS while spectral dependent Raman responses can be selectively switched on and off at the same substrate location

[a]Helmholtz-Zentrum Dresden-Rossendorf, Bautzner Landstraße 400, 01328 Dresden, Germany
[b]Rudolf Virchow Center, University of Würzburg, Josef-Schneider-Str. 2, 97080 Würzburg, Germany. E-mail: benjamin.schreiber@uni-wuerzburg.de
[c]Leibniz-Institut für Analytische Wissenschaften-ISAS-e.V., ISAS Berlin, Schwarzschildstr. 8, 12489 Berlin, Germany
[d]Vilnius University, Faculty of Chemistry and Geosciences, Department of Physical Chemistry, Naugarduko 24, Vilnius, Lithuania
[e]Chemnitz University of Technology, D-09107 Chemnitz, Germany. E-mail: raulmet@gmail.com
[f]Tomsk Polytechnic University, 30 Lenin Ave, 634050 Tomsk, Russia

† Electronic supplementary information (ESI) available. See DOI: 10.1039/c8ra04031a

and molecule concentration. A particularly interesting approach is the application of surface structures as a template for the self-organized alignment of molecules,[5] colloidal nanoparticles,[6] or vapour deposited nanoparticles.[7–9] Template candidates are atomic terraces,[10,11] epitaxially grown ridge-valley structures,[12,13] and low-energy ion-induced ripple patterns on solid surfaces.[14] These ripple structures are especially interesting, because they allow both wafer-scale fabrication on most solid surfaces and flexible ripple periodicities of several tens to hundreds of nanometers that can be controlled by the ion irradiation parameters.[15–19] The substrates are ideal for the self-organization of plasmonic nanostructures with strong anisotropic optical properties.[20–22] The polarization-dependent SERS response of such structures was reported for parallel gold nanowires (NWs)[23–26] and silver nanoparticle (NP) chains.[27,28] For gold NWs, the SERS enhancement is dominant across the ripple pattern. Along continuous metallic nanowires, a Drude-like behaviour is observed undermining the potential for surface enhancement. In contrast, noble metal nanoparticle chains on rippled templates have the potential for SERS with bidirectional independent tuneable LSPRs.[13,28–30] It is understandable that SERS substrates that are plasmonically active under multiple excitation wavelengths have significant potential for multipurpose chemical and biochemical sensing applications. This kind of SERS structures can be produced at a large-scale with a two-step fabrication routine. Since, the SERS enhancement effect of anisotropically aligned silver nanoparticles on rippled patterns is well studied,[20,27,28] it is time to investigate the plasmonic responses of anisotropically aligned gold nanoparticle systems for SERS applications. Gold nanostructures are known for their chemical stability,[31] biocompatibility, and strong plasmonic responses in red and near-infrared spectral regions[32,33] and thus gold is a popular material choice for SERS substrates.[34]

Here we present gold nanoparticle structures that are self-organized along rippled templates. We generate these nanostructures with a two-step fabrication routine including low-energy ion beam irradiation and oblique-angle physical vapour deposition. We show that the position of the localized surface plasmon resonance (LSPR) depends on the gold nanoparticle geometry, which allows tuning the LSPRs from the visible (VIS) to the near-infrared (NIR) spectral range. The different LSPRs can be excited selectively by setting the excitation light polarization along or across the rippled structures. We study the particle growth and alignment process along the rippled template by scanning electron microscopy (SEM) and cross-sectional transmission electron microscopy (TEM). The anisotropic spectral properties are evaluated by spectroscopic ellipsometry (SE) and probed by Raman spectroscopy for three different laser lines within the VIS-NIR range. We use a 1 nm ultra-thin homogenous film of cobalt phthalocyanine (CoPc) as the Raman probe deposited simultaneously on all sample surfaces. With an ultra-homogeneous film as a SERS probe the number of molecules on a SERS substrate and reference can be directly compared. This approach allows us to make a proper evaluation of the SERS enhancement without the need of additional assumptions to estimate the number of molecules in the SERS substrates.[32] We visualize the plasmonic hotspots by the finite element method (FEM) simulations using the exact nanoparticle size, geometry, and configuration experimentally determined from the SEM and TEM analysis.

2 Experimental

2.1 Sample fabrication

First step. Ripple patterns are produced by ion irradiation with a Kaufman type ion-source in a vacuum chamber. The sample was transferred into the chamber and tilted until the surface normal is oriented 67° of with respect to the ion source. Once a base pressure of $\sim 10^{-8}$ mbar was reached, argon gas was inserted into the chamber with a pressure of $\sim 10^{-4}$ mbar. Ion-beam irradiation is performed at room temperature with a broad argon ion-beam (acceleration voltage 800 V, ion flux $\sim 2.5 \times 10^{15}$ cm^{-2} s^{-1}). The irradiation process was finished when a total ion dose of 10^{18} cm^{-2} was reached. These process parameters led to surface ripple structures on silicon with a low defect density and a periodicity of 50 nm.[35]

Second Step. Oblique-angle gold deposition was performed by electron-beam deposition in a high vacuum chamber (Bes-Tech, Germany) at $\sim 10^{-8}$ mbar working pressure and a deposition angle of 80° with respect to the surface normal and facing the long flanks of the ripple pattern. The deposition rate of ~ 0.01 nm s^{-1} was controlled by a quartz micro balance (QCM). The sample thicknesses are given by the QCM recorded gold thickness. Since the QCM is calibrated for the deposition on surfaces under normal incidence angle, we checked the gold deposition with Rutherford backscattering spectrometry (RBS). For RBS, the 1.7 MeV helium ion-beam at the Helmholtz-Zentrum Dresden-Rossendorf was used. The data were analysed by the software SIMNRA.[36] The film thicknesses of the Au nanostructures are calculated by the areal density divided by the product of surface occupation and the atomic density of gold (see ESI Fig. S1†). The average effective deposition rate for the tilted samples is (1.2 ± 0.1) pm s^{-1}. The ratio of QCM and RBS measured film thicknesses are $\sim\cos(80°)$. This is in agreement with by the projected area caused by oblique deposition angle. For additional post-deposition annealing in air a conventional heating plate was used.

2.2 Morphological characterization

The topography of the ion-induced surface ripple pattern was measured by atomic force microscopy (AFM) in tapping mode (Bruker MM8 AFM with PPP-NCRL tips from Nanosensors). Top view images of deposited Au structures were taken by scanning electron microscopy (SEM) using a Raith e_LiNE plus with a Zeiss Gemini optics. Cross-sectional transmission electron microscopy (TEM) images were taken using an image C_s-corrected Titan 80-300 microscope FEI ltd (Eindhoven, The Netherlands). TEM lamella preparation was performed by a Zeiss Crossbeam NVision 40 system and a Kleindiek micromanipulator. To protect the Au nanoparticles from being damaged by the focused Ga ion beam, the sample surface was initially covered by depositing a carbon-based cap layer. Prior to each

TEM analysis, the specimen mounted in a double-tilt analytical holder was placed for 10 seconds into a plasma Model 1020 cleaner (Fischione) to remove contaminations.

2.3 Optical characterization and Raman spectroscopy

We performed spectroscopic ellipsometry (SE) with a J. A. Woollam M-2000FI device (angle of incidence = 75°, 100 repetitions per spectra) to measure the change of the phase and polarization ration of the light reflected from the sample.[37] The plotted imaginary part of the pseudo-dielectric function, $\langle \varepsilon_2 \rangle$ provides the indication of light absorption.[38,39] In our plasmonic systems, gold nanostructures are formed on a silicon surface. Light absorption above 550 nm is directly connected to excitation of surface plasmons. A peak in the $\langle \varepsilon_2 \rangle$ spectra indicates the LSPR position.[40] The rotation of the sample allowed the measurement of both optical axes of sample parallel ($\vec{E}_{\parallel}$) and perpendicular. ($\vec{E}_{\perp}$) to the ripple patterns.

For Raman Spectroscopy (RS) a LabRam HR800 from Horiba Scientific equipped in back-scattering geometry was used. A HeNe Laser (632.8 nm, laser power at the sample 1 mW) was focused and the signal collected with a 50× LWD objective (numerical aperture of 0.5). The Raman signal was diffracted by a 600 lines per mm diffraction grating and recorded by an EMCCD. A 1 nm thick cobalt phthalocyanine (CoPc) film was used as a well-defined Raman probe. CoPc has an absorption maximum at 650 nm.[41,42] Thus the molecules are resonantly excited at 632.8 nm. The samples were covered with CoPc by molecular beam evaporation in a vacuum chamber (working pressure 10^{-6} mbar). The film thickness was determined by QCM-based measurement. On SERS and reference substrates (REF) the number of CoPc molecules (N) was considered identical because all substrates were simultaneously covered under the same conditions of deposition ($N_{\mathrm{REF}} \cong N_{\mathrm{SERS}}$). This allows us to calculate the SERS enhancement factor directly from the Raman intensities $\mathrm{EF}_{\mathrm{SERS}} = (I_{\mathrm{SERS}}/I_{\mathrm{REF}})/(N_{\mathrm{SERS}}/N_{\mathrm{REF}}) \cong I_{\mathrm{SERS}}/I_{\mathrm{REF}}$. All shown Raman spectra are averages of 16 individual Raman spectra registered at different measuring points (in an 80 μm × 80 μm grid). Each single point was averaged for 10 times with 1 second acquisition time. In the ESI Fig. S4† an example of Raman signal acquisition at different locations on a sample and under different polarizations is shown. Performing SERS with an ultra-thin film of CoPc simultaneously deposited on all substrates, and with the time and spatial averages of the Raman signal it was possible to evaluate the SERS enhancement factors without minimal assumptions and statistical uncertainties.[43]

2.4 Finite element method calculations (FEM)

We used the wave optics module in COMSOL Multiphysics 4.4. From SEM images, we extracted the particle geometry by masking the particles greater than 5 nm (using Gwyddion[44]). The masks were contoured and saved as .dxf files (by Python 2.7 and OpenCV) to import into COMSOL. We used dielectric functions for gold,[45] silicon,[46] and silicon dioxide.[47] For 2D "bird-view" calculations the gold particles were embedded in an effective medium (82.5% air and 17.5% silicon). The excitation field is implemented as an incoming wave in the model plane. For cross-section simulations we used an excitation port and continuous periodic boundary conditions. A maximum mesh size of 1 nm and 5 nm were used for the boundaries and domains, respectively. The mean field enhancement was calculated by the area mean value of $|E/E_0|^4$ over the whole nanostructure surface where $|E_0|$ is the mean electric field surrounding the particle ensemble.

3 Results

Fig. 1 shows the morphology development of the plasmonic gold nanostructures during the metal deposition process. As templates, we used ion-beam induced ripple-patterned silicon surfaces with a ripple periodicity of (49.9 ± 2.5) nm (for more details see Methods Section and ESI Fig. S1†). The two-step fabrication routine of SERS substrates with bidirectional plasmon resonances is illustrated in Fig. 1(a). Different morphological steps are observed depending on the gold thickness. Starting with 30 nm, the nanoparticle self-organization with

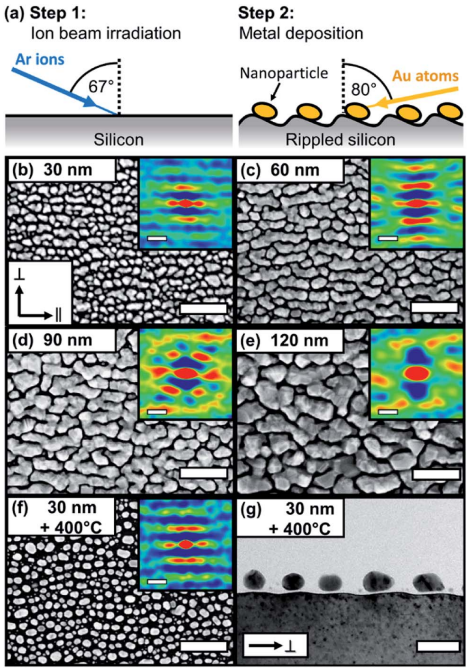

Fig. 1 Morphology of self-organized gold nanostructures on rippled templates. (a) Illustration of two-step fabrication routine. (b–f) Top-view SEM images for different gold thicknesses from 30 nm to 120 nm and (f) 30 nm with post-annealing at 400 °C. The insets show the corresponding 2D autocorrelations. (g) Cross-sectional bright-field TEM image of (f). Scale bars (b–f): 200 nm (insets 50 nm), (g) 50 nm.

a preferred in-plane orientation along the ripples is clearly observable. By increasing the gold film thickness, the nanoparticles start to elongate and form wire-like nanostructures. With a further increase of the gold thickness, coarser and more complex structures are formed, without the formation of a continuous gold layer. By further increasing the gold thickness, the gold films formed voids reaching a maximum surface coverage of ~80% (see ESI Fig. S1†). With an additional post-deposition annealing at 400 °C (for 1 hour), we re-shaped the rough and less spherical gold particles into more smooth and spherical ones (f and g). The morphology obtained for annealed gold particles is comparable to the known silver particle chains on rippled templates.[7,8]

Without annealing, rougher particles with less defined shapes are observable.[48,49] From the 2D autocorrelation and particle analysis, we deduce details on the particle geometry. For gold depositions of 30 nm and 60 nm nominal thicknesses, a clear separation of the structures on the rippled templates is observable. For larger thicknesses of 90 nm and 120 nm this separation is lost, and particle coalescence takes place.

From the 2D autocorrelation, we derived the average center-to-center particle distances for the parallel (||) and perpendicular (⊥) directions with respect to the pattern axis. The gold nanoparticles follow the periodicity of the template with the maximum particle diameter orientated along (|| direction) and the minimum diameter across (⊥ direction) the ripples. Table 1 summarizes the particle dimensions for samples with gold thicknesses of 30 nm, 60 nm and for 30 nm Au additionally annealed at 400 °C for 60 minutes. For 90 nm and 120 nm gold deposition thicknesses no isolated structures are formed.

In Fig. 2, we show the optical properties of the nanostructures for different gold thicknesses. We plot the imaginary part of the effective pseudo dielectric function $\langle\varepsilon_2\rangle$ measured by spectroscopic ellipsometry. $\langle\varepsilon_2\rangle$ is associated with the absorption of the Au layer and gives us an indication for the position of the LSPR. The area between 400 to 500 nm is the interband transition of gold, while the plasmon resonance starts in the range of 600 nm and red-shifts for increasing deposition thickness, moving to the mid-infrared range. The LSPR can be excited at different spectral positions for polarizations across ($\vec{E}_\perp$) and along ($\vec{E}_\parallel$) the ripple axis. The LSPRs for $\vec{E}_\perp$ polarization are observed in the spectral region from ~600 nm to ~1000 nm, red-shifting with increasing gold thickness. For $\vec{E}_\parallel$ polarization, the LSPR for 30 nm gold thickness sample starts at ~800 nm near infrared spectral region and then it red-shifts with increasing gold deposition where the LSPR peak gets broader becoming Drude-like. The results for polarizations

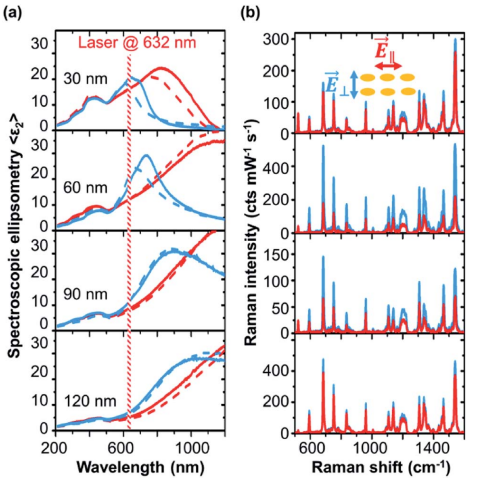

Fig. 2 Development of bidirectional LSPR through the gold deposition process. (a) Spectroscopic ellipsometry (SE) of the imaginary part of the effective dielectric function $\langle\varepsilon_2\rangle$ for polarization parallel ($\vec{E}_\parallel$, red) and perpendicular ($\vec{E}_\perp$, blue) to the nanoparticle chains. Solid and dashed lines for spectra with and without deposited CoPc molecules as Raman probe. The Raman excitation laser line of 632.8 nm is indicated. (b) Raman spectra at the same thicknesses corresponding to SE spectra in each column. Raman signal for different laser polarization $\vec{E}_\parallel$ (red) and $\vec{E}_\perp$ (blue) are shown.

Table 1 Summarized dimensions of self-organized gold nanoparticles by annealing

Sample	Min. diameter[a] (nm)	Max. diameter[a] (nm)	Particle height (nm)	∥ center-to-center (nm)	⊥ center-to-center (nm)
30 nm	24.4 ± 0.3	36.5 ± 1.4	18.1 ± 2.9	30.3 ± 9.4	46.6 ± 8.7
30 nm, annealed	23.1 ± 0.2	29.8 ± 0.4	17.6 ± 3.5	40.2 ± 12.8	46.9 ± 8.4
60 nm	40.0 ± 0.6	53.1 ± 7.4[b]	—	49.1 ± 8.3	49.1 ± 8.3

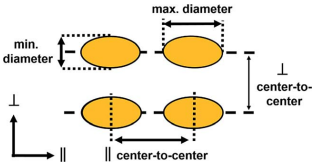

[a] Excluding the particles with diameter < 10 nm. [b] Excluding the particles grown together over grooves.

across ($\vec{E}_\perp$) and along ($\vec{E}_\parallel$) the template show that the LSPRs at different spectral positions can be selectively excited. Evidently, this selectivity is defined by the anisotropic particle shape and coupling along or across the templates. We have probed the plasmonic resonances by Raman spectroscopy with a laser excitation at 632.8 nm, as shown in Fig. 2(b). Using different polarisations Raman signals changes. We analysed the 687 cm^{-1} A_{1g} vibrational mode of CoPc.[50] The A_{1g} mode has a signal strength of 0.46 intensity counts mW^{-1} s^{-1} on unmodified silicon (see ESI Fig. S2†). As discussed before, the Raman enhancement is given by the intensity ratio of the plasmonic structures with respect to the Raman signal of the molecule on a flat (100) silicon surface used as reference. Enhancement factors from ~150 up to ~1200 are observed from the gold nanostructures. SERS enhancement factors (EF) of 10^3 to 10^4 are reported for silver nanostructures deposited on rippled silicon templates.[27,28] Silver nanostructures are well known for their strong plasmon resonances. The benefits of gold nanostructures are the biological and chemical stability and bio-compatibility.

On the first view, our shown SERS effects are comparably low to other SERS substrates and colloidal particle systems.[43,51–55] In the other hand, SERS enhancement factors are typically given by comparing the ratios of Raman intensities and number of molecules of the SERS substrate and a reference substrate. In the scenario when molecules are diluted in a liquid, the surface affinity of molecules can greatly differ between the reference substrates and the plasmonic nanostructures; this often leads to SERS EF overestimation.[43] The benefit of the used method in this study is that the SERS enhancement factors can be determined without the need to make assumptions about the molecule concentration.[32] In this way we can directly probe the plasmonic field enhancement *via* the Raman enhancement factors. This allows the possibility for direct comparison of SERS EFs between different substrates. In comparison to similar self-assembled gold nanostructures our reported SERS EFs are higher or comparable.[4,23–26] Further, since we can measure and compare the SERS EFs on different substrates, we can directly connect spectroscopic measurements with the Raman field enhancement factors to probe the plasmonic effects on the substrate.

Table 2 summarizes the values for $\langle\varepsilon_2\rangle$ and SERS enhancement for 632.8 nm excitation wavelength. The highest enhancement is obtained for $\vec{E}_\perp$. This means that the signal is dominated by the area between the gold chains since the plasmonic resonance of that direction is excited at this wavelength.

Table 2 Summarized Raman enhancement factor EF and pseudo dielectric functions $\langle\varepsilon_2\rangle$ for $\vec{E}_\perp$ and $\vec{E}_\parallel$ polarizations at excitation wavelength at 632.8 nm

Sample	$EF_\parallel$	$EF_\perp$	$\langle\varepsilon_2\rangle_\parallel$	$\langle\varepsilon_2\rangle_\perp$	$EF_\perp/EF_\parallel$	$\langle\varepsilon_2\rangle_\perp{}^2/\langle\varepsilon_2\rangle_\parallel{}^2$
30 nm	289	313	16.2	20.2	1.1	1.1
60 nm	385	1135	12.1	17.8	2.9	3.0
90 nm	144	314	8.5	11.1	2.2	2.0
120 nm	837	1032	5.2	7.0	1.2	1.8

For gold thicknesses of 60 nm and 90 nm, a clear anisotropic Raman signal is observed, while for the 30 nm and 120 nm gold thicknesses, the Raman signal anisotropy is less pronounced. These results are in agreement with the absorption due to LSPR deduced from the SE results. We have registered the largest Raman signal amplification for the excitation with 632.8 nm and $\vec{E}_\perp$ polarization. The SERS anisotropy $EF_\perp/EF_\parallel$ is in good agreement with the square of ratio of the pseudo-dielectric function $\langle\varepsilon_2\rangle_\perp{}^2/\langle\varepsilon_2\rangle_\parallel{}^2$ at this spectral position. The amplitude values of the imaginary part of pseudo dielectric function at the excitation wavelengths are not directly representing the plasmonic excitation strengths. The reason is, that the local plasmonic field enhancement also depends on local geometry of the plasmonic particle. For example, we also observe a strong off-plasmon resonance SERS effect on 120 nm gold structures. This is reasoned by strong electromagnetic field enhancement inside narrow voids (see Fig. 1).

Until know we presented the development of LSPR and SERS enhancement for different gold thicknesses deposited on rippled templates. The structures with the most defined geometry and bidirectional LSPRs are the 30 nm gold substrates. By additional post deposition annealing, the gold nanoparticles become more spherical and defined. This reduces the particle center-to-center distances and particle diameter in ∥ direction (see Table 1.). We want to observe the LSPR shift and the effect on SERS by post deposition annealing. In Fig. 3, we compare the anisotropic SERS effect of annealed and non-annealed samples probed by the excitation with three laser lines (532 nm, 638 nm, and 785 nm). With 532 nm, no clear anisotropic effect is observable for both samples. The reason is the off-LSPR excitation, and thus the Raman enhancement is rather low.

For 638 nm excitation, we see a clear anisotropic SERS effect on the annealed sample and a high enhancement for the $\vec{E}_\parallel$ polarization. For the non-annealed sample, a high SERS response for $\vec{E}_\perp$ is obtained. This situation reverses for the 785 nm excitation. Here, for the non-annealed sample, a very high SERS enhancement is obtained for the $\vec{E}_\parallel$ direction.

This is a good example for a sample that supports LSPRs excited under two different laser lines which that can be selected by polarization. The 785 nm excitation does not match a LSPR peak of the annealed sample and thus the observed non-resonant SERS enhancement is low and in good agreement with the SE results. The difference of $\langle\varepsilon_2\rangle$ is shown in Fig. 3(b). Values below zero show an increased LSPR excitation in $\vec{E}_\perp$ and above zero in the $\vec{E}_\parallel$ direction. The spectral anisotropy shows that the annealed sample supports an LSPR for $\vec{E}_\parallel$ excitation with a peak around 650 nm. The annealed sample carries two LSPRs matching the 638 nm and 785 nm excitation wavelength, each one individually accessible by controlling the excitation polarization.

Until now, we experimentally characterized the bidirectional optical properties of the self-organized substrates and probed the signal amplification with SERS. In Fig. 4, we show the spatial distribution of hotspots obtained by finite element method results for the annealed and non-annealed samples. For the

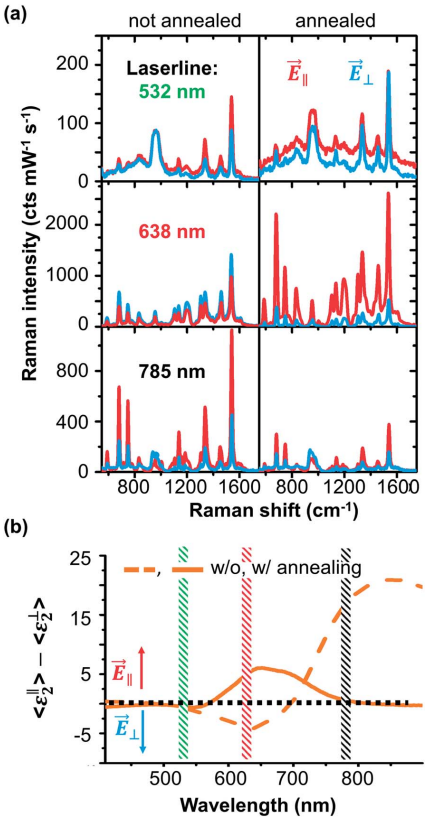

Fig. 3 Polarization dependent VIS-NIR Raman responses for 30 nm gold thickness with and without annealing. (a) Raman spectra of 1 nm CoPc probed by three different laser lines (top: 532 nm, middle: 638 nm, and bottom: 785 nm) for parallel ($\vec{E}_{\parallel}$, red) and perpendicular ($\vec{E}_{\perp}$, blue) polarizations. (b) Difference of the imaginary parts of the pseudo-dielectric function for parallel and perpendicular excitation measured for 30 nm gold thickness without (dashed) and with annealing (solid). Difference below or above zero means that Raman is enhanced for $\vec{E}_{\perp}$ or $\vec{E}_{\parallel}$ polarization.

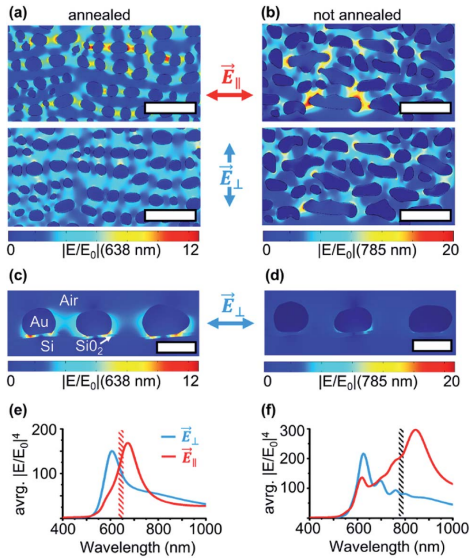

Fig. 4 FEM calculation results of the near-field enhancement of electric $|E/E_0|$ based on SEM images. The systems modeled correspond to (a) annealed and (b) non-annealed gold samples for two different directions of the incident electric field (top) $\vec{E}_{\parallel}$ and (bottom) $\vec{E}_{\perp}$. Scale bars: 100 nm. The particle cross-section visualization of the annealed (c) and not annealed (d) sample is shown below (scale 30 nm). Simulated spectra of average SERS enhancement ($\propto$ avrg. $|E/E_0|^4$) for annealed (e) and not annealed (f) particle geometries for $\vec{E}_{\perp}$ and $\vec{E}_{\parallel}$ polarizations. Simulated spectra of average SERS enhancement ($\propto$ avrg. $|E/E_0|^4$) for annealed and not annealed particle geometries for $\vec{E}_{\perp}$ and $\vec{E}_{\parallel}$ polarizations.

annealed sample under 638 nm $\vec{E}_{\parallel}$ excitation, we can visualize the plasmonic hotspots along the particle chains.

The LSPR coupling between the particles forces the hotspots to follow the particles on the ripple structure, even if the particles are not fully in line with the excitation field. For $\vec{E}_{\perp}$, a lower field enhancement with a weak "far"-coupling across the ripples is visible. In the simulation of the cross-section view in Fig. 4(c), it can be seen that a big portion of the electric field is caged in the native silicon oxide layer between the nanoparticles and the silicon substrate.[56] Thus for $\vec{E}_{\perp}$ the plasmonic coupling between the nanoparticles is weak and also because of the large separation distance between particles by the ripple structure in the $\perp$ direction. Interestingly, even if the particles are tilted because of the ripple pattern, the weak plasmonic interaction follows the shortest distance between the nanoparticles and the dipole-like LSPR field extends into the native oxide layer.

For the non-annealed scenario, the situation becomes more complicated. For the excitation direction $\vec{E}_{\parallel}$ at 785 nm, strong plasmon hotspots appear especially on particles with an elongated shape. The broad particle size, aspect ratio, and shape distribution result in LSPRs that can be excited in a wide spectral range. The chain structure made by interconnected oval-shaped particles can also contribute to the coupling of hotspots among particles with different shapes.[57] As we know from the experimental ellipsometry and Raman results, the $\vec{E}_{\perp}$ 785 nm excitation does not match the LSPRs and thus no active hotspots are visible. Interestingly, because of the high aspect ratio of non-annealed particles, a weak plasmonic coupling can also be seen along the particle rows. We summarize in Fig. 4(e and f) the geometry average $|E/E_0|^4$ spectra for both particle geometries. Since we used a homogenous film of molecules to probe the SERS effect, the amplification of Raman intensity is directly predictable by the $EF_{SERS} \propto |E/E_0|^4$ averaged over the whole sample geometry. Our simulated enhancement spectra

are in good agreement with the measured $\langle \varepsilon_2 \rangle$ (see ESI Fig. S3†) and anisotropic Raman signal ratios for $\vec{E}_{\perp}$ and $\vec{E}_{\parallel}$. The calculated enhancements are ~1–3 times weaker than the experimentally observed signal enhancements (compared to Table 2). This is caused by the fact that most of the signal amplification arises from just a few but very strong hotspots, preferable between very rough particles, therefore the samples cannot be fully represented by the FEM calculations.

4 Conclusions

We show a two-step fabrication process to generate gold nanostructures aligned along rippled templates. These structures show localized surface plasmon resonances that can be bidirectionally excited. These LSPRs are tuneable by controlling the fabrication parameters. We demonstrated substrates with LSPRs fitting laser lines from visible to near-infrared spectral regions matching the most conventional excitations used in Raman spectroscopy. We report SERS enhancement of up to ~1200 times. This SERS signal enhancement is comparatively high for a large-scale self-organized gold films reported in literature.[4,23–26] Finite element method calculations showed the polarization and wavelength dependent hotspot distributions of gold nanoparticle systems for well-ordered annealed particle films and less well-shaped gold particles deposited at room temperature are observed.

The biocompatible and chemically stable gold nanostructures here reported support strong plasmonic signal enhancement for multiple excitation wavelengths. Because of the time and cost-effective fabrication routine we report, the structures are suitable for mass-fabrication and only a physical vapor deposition system and a low-energy ion beam source are needed. These two requirements are well-established and widely used in research and industry laboratories. We believe that the large-scale self-organized gold nanostructures with bidirectional plasmonic responses have enormous potential for chemical and biological sensing applications where a large number of substrates are needed.

Conflicts of interest

There are no conflicts to declare.

Acknowledgements

We thank Adrian Keller for help and supervision of the initial fabrication of ion-beam induced silicon surface structures. RDR and ES thank the Tomsk Polytechnic University Competitiveness Enhancement Program. AR is grateful to European Regional Development Fund according to the supported activity 'Research Projects Implemented by World-class Researcher Groups' under Measure No. 01.2.2-LMT-K-718. The publication costs of this article were funded by the German Research Foundation/DFG and the Chemnitz University of Technology in the funding programme Open Access Publishing.

Notes and references

1 K. Kneipp, H. Kneipp, I. Itzkan, R. R. Dasari and M. S. Feld, *Chem. Rev.*, 1999, **99**, 2957–2976.
2 S. M. Nie and S. R. Emery, *Science*, 1997, **275**, 1102–1106.
3 K. A. Willets and R. P. Van Duyne, *Annu. Rev. Phys. Chem.*, 2007, **58**, 267–297.
4 C. D'Andrea, J. Bochterle, A. Toma, C. Huck, F. Neubrech, E. Messina, B. Fazio, O. M. Marago, E. Di Fabrizio, M. L. de la Chapelle, P. G. Gucciardi and A. Pucci, *ACS Nano*, 2013, **7**, 3522–3531.
5 B. Teshome, S. Facsko and A. Keller, *Nanoscale*, 2014, **6**, 1790–1796.
6 Q. Tong, E. W. Malachosky, J. Raybin, P. Guyot-Sionnest and S. J. Sibener, *J. Phys. Chem. C*, 2014, **118**, 19259–19265.
7 T. W. H. Oates, A. Keller, S. Facsko and A. Mucklich, *Plasmonics*, 2007, **2**, 47–50.
8 T. W. H. Oates, A. Keller, S. Noda and S. Facsko, *Appl. Phys. Lett.*, 2008, **93**, 063106.
9 M. Morales, R. Droppa Jr, S. R. S. d. Mello, C. A. Figueroa, A. R. Zanatta and F. Alvarez, *AIP Adv.*, 2018, **8**, 015025.
10 R. Verre, K. Fleischer, O. Ualibek and I. V. Shvets, *Appl. Phys. Lett.*, 2012, **100**, 031102.
11 F. Cuccureddu, S. Murphy, I. V. Shvets, M. Porcu and H. W. Zandbergen, *Nano Lett.*, 2008, **8**, 3248–3256.
12 F. Bisio, G. Gonella, G. Maidecchi, R. Buzio, A. Gerbi, R. Moroni, A. Giglia and M. Canepa, *J. Phys. D: Appl. Phys.*, 2015, **48**, 184003.
13 L. Anghinolfi, R. Moroni, L. Mattera, M. Canepa and F. Bisio, *J. Phys. Chem. C*, 2011, **115**, 14036–14043.
14 R. M. Bradley and J. M. E. Harper, *J. Vac. Sci. Technol., A*, 1988, **6**, 2390–2395.
15 A. Keller and S. Facsko, *Materials*, 2010, **3**, 4811–4841.
16 A. Keller, S. Facsko and W. Möller, *J. Phys.: Condens. Matter*, 2009, **21**, 495305.
17 D. Babonneau, E. Vandenhecke and S. Camelio, *Phys. Rev. B*, 2017, **95**, 085412.
18 A. Toma, B. Š. Batič, D. Chiappe, C. Boragno, U. Valbusa, M. Godec, M. Jenko and F. B. d. Mongeot, *J. Appl. Phys.*, 2008, **104**, 104313.
19 X. Ou, A. Keller, M. Helm, J. Fassbender and S. Facsko, *Phys. Rev. Lett.*, 2013, **111**, 016101.
20 D. Gkogkou, T. Shaykhutdinov, T. W. H. Oates, U. Gernert, B. Schreiber, S. Facsko, P. Hildebrandt, I. M. Weidinger, N. Esser and K. Hinrichs, *Appl. Surf. Sci.*, 2017, **421**, 460–464.
21 S. Camelio, D. Babonneau, F. Pailloux, S. Rousselet and E. Vandenhecke, *Nanosci. Nanotechnol. Lett.*, 2013, **5**, 19–26.
22 S. Camelio, E. Vandenhecke, S. Rousselet and D. Babonneau, *Nanotechnology*, 2014, **25**, 035706.
23 C. D'Andrea, B. Fazio, P. G. Gucciardi, M. C. Giordano, C. Martella, D. Chiappe, A. Toma, F. Buatier de Mongeot, F. Tantussi, P. Vasanthakumar, F. Fuso and M. Allegrini, *J. Phys. Chem. C*, 2014, **118**, 8571–8580.
24 B. Fazio, C. D'Andrea, F. Bonaccorso, A. Irrera, G. Calogero, C. Vasi, P. G. Gucciardi, M. Allegrini, A. Toma, D. Chiappe,

C. Martella and F. Buatier de Mongeot, *ACS Nano*, 2011, **5**, 5945–5956.
25 Q. Jia, X. Ou, M. Langer, B. Schreiber, J. Grenzer, P. F. Siles, R. D. Rodriguez, K. Huang, Y. Yuan, A. Heidarian, R. Hübner, T. You, W. Yu, K. Lenz, J. Lindner, X. Wang and S. Facsko, *Nano Res.*, 2017, DOI: 10.1007/s12274-017-1793-y.
26 D. Repetto, M. C. Giordano, A. Foti, P. G. Gucciardi, C. Mennucci and F. B. de Mongeot, *Appl. Surf. Sci.*, 2018, **446**, 83–91.
27 M. Ranjan and S. Facsko, *Nanotechnology*, 2012, **23**, 485307.
28 D. Gkogkou, B. Schreiber, T. Shaykhutdinov, H. K. Ly, U. Kuhlmann, U. Gernert, S. Facsko, P. Hildebrandt, N. Esser, K. Hinrichs, I. M. Weidinger and T. W. H. Oates, *ACS Sens.*, 2016, **1**, 318–323.
29 M. Ranjan, S. Facsko, M. Fritzsche and S. Mukherjee, *Microelectron. Eng.*, 2013, **102**, 44–47.
30 D. Babonneau, S. Camelio, L. Simonot, F. Pailloux, P. Guerin, B. Lamongie and O. Lyon, *EPL*, 2011, **93**, 26005.
31 M. Walter, J. Akola, O. Lopez-Acevedo, P. D. Jadzinsky, G. Calero, C. J. Ackerson, R. L. Whetten, H. Gronbeck and H. Hakkinen, *Proc. Natl. Acad. Sci. U. S. A.*, 2008, **105**, 9157–9162.
32 R. D. Rodriguez, E. Sheremet, M. Nesterov, S. Moras, M. Rahaman, T. Weiss, M. Hietschold and D. R. T. Zahn, *Sens. Actuators, B*, 2018, **262**, 922–927.
33 K. M. McPeak, S. V. Jayanti, S. J. P. Kress, S. Meyer, S. Iotti, A. Rossinelli and D. J. Norris, *ACS Photonics*, 2015, **2**, 326–333.
34 J. Baniukevic, I. H. Boyaci, A. G. Bozkurt, U. Tamer, A. Ramanavicius and A. Ramanaviciene, *Biosens. Bioelectron.*, 2013, **43**, 281–288.
35 A. Keller, S. Facsko and W. Möller, *New J. Phys.*, 2008, **10**, 063004.
36 M. Mayer, *AIP Conference Proceedings*, 1999.
37 H. Fujiwara, *Spectroscopic Ellipsometry: Principles and Applications*, John Wiley & Sons, 2007.
38 H. Kuzmany, *Solid-State Spectroscopy: An Introduction*, Springer Science & Business Media, 2009.
39 H. Fujiwara, *Spectroscopic Ellipsometry: Principles and Applications*, John Wiley & Sons, 2007.
40 T. Oates, H. Wormeester and H. Arwin, *Prog. Surf. Sci.*, 2011, **86**, 328–376.
41 F. Li, Q. Zheng, G. Yang and P. Lu, *Dyes Pigm.*, 2008, **77**, 277–280.
42 A. T. Davidson, *J. Chem. Phys.*, 1982, **77**, 168–172.
43 S. L. Kleinman, R. R. Frontiera, A.-I. Henry, J. A. Dieringer and R. P. V. Duyne, *Phys. Chem. Chem. Phys.*, 2012, **15**, 21–36.
44 D. Necas and P. Klapetek, *Cent. Eur. J. Phys.*, 2012, **10**, 181–188.
45 P. B. Johnson and R. W. Christy, *Phys. Rev. B: Solid State Rev*, 1972, **6**, 4370–4379.
46 D. E. Aspnes and A. A. Studna, *Phys. Rev. B: Condens. Matter Mater. Phys. Rev*, 1983, **27**, 985–1009.
47 L. Gao, F. Lemarchand and M. Lequime, *J. Eur. Opt. Soc. Rapid Publ.*, 2013, **8**, 13010.
48 B. J. Y. Tan, C. H. Sow, T. S. Koh, K. C. Chin, A. T. S. Wee and C. K. Ong, *J. Phys. Chem. B*, 2005, **109**, 11100–11109.
49 K. C. Kao, H. Nishi and T. Tatsuma, *Phys. Chem. Chem. Phys.*, 2018, **20**, 3735–3740.
50 Z. Q. Liu, X. X. Zhang, Y. X. Zhang and J. Z. Jiang, *Spectrochim. Acta, Part A*, 2007, **67**, 1232–1246.
51 S. Rodal-Cedeira, V. Montes-Garcia, L. Polavarapu, D. M. Solis, H. Heidari, A. La Porta, M. Angiola, A. Martucci, J. M. Taboada, F. Obelleiro, S. Bals, J. Perez-Juste and I. Pastoriza-Santos, *Chem. Mater.*, 2016, **28**, 9169–9180.
52 S. Gomez-Grana, C. Fernandez-Lopez, L. Polavarapu, J. B. Salmon, J. Leng, I. Pastoriza-Santos and J. Perez-Juste, *Chem. Mater.*, 2015, **27**, 8310–8317.
53 P. A. Mosier-Boss, *Nanomaterials*, 2017, **7**, 142.
54 D. Cialla-May, X. S. Zheng, K. Weber and J. Popp, *Chem. Soc. Rev.*, 2017, **46**, 3945–3961.
55 C. Muehlethaler, M. Leona and J. R. Lombardi, *Anal. Chem.*, 2016, **88**, 152–169.
56 S. H. Guo, S. J. Tsai, H. C. Kan, D. H. Tsai, M. R. Zachariah and R. J. Phaneuf, *Adv. Mater.*, 2008, **20**, 1424–1428.
57 Z. Mingsi, Q. Jiwei, J. Meiling, L. Yudong, Q. Jun, C. Jing, C. Zongqiang, S. Qian and X. Jingjun, *J. Opt.*, 2018, **20**, 025001.

For notes

Vilnius University Press
1 Universiteto St., LT-01513 Vilnius
info@leidykla.vu.lt, www.leidykla.vu.lt

Print run 13 copies